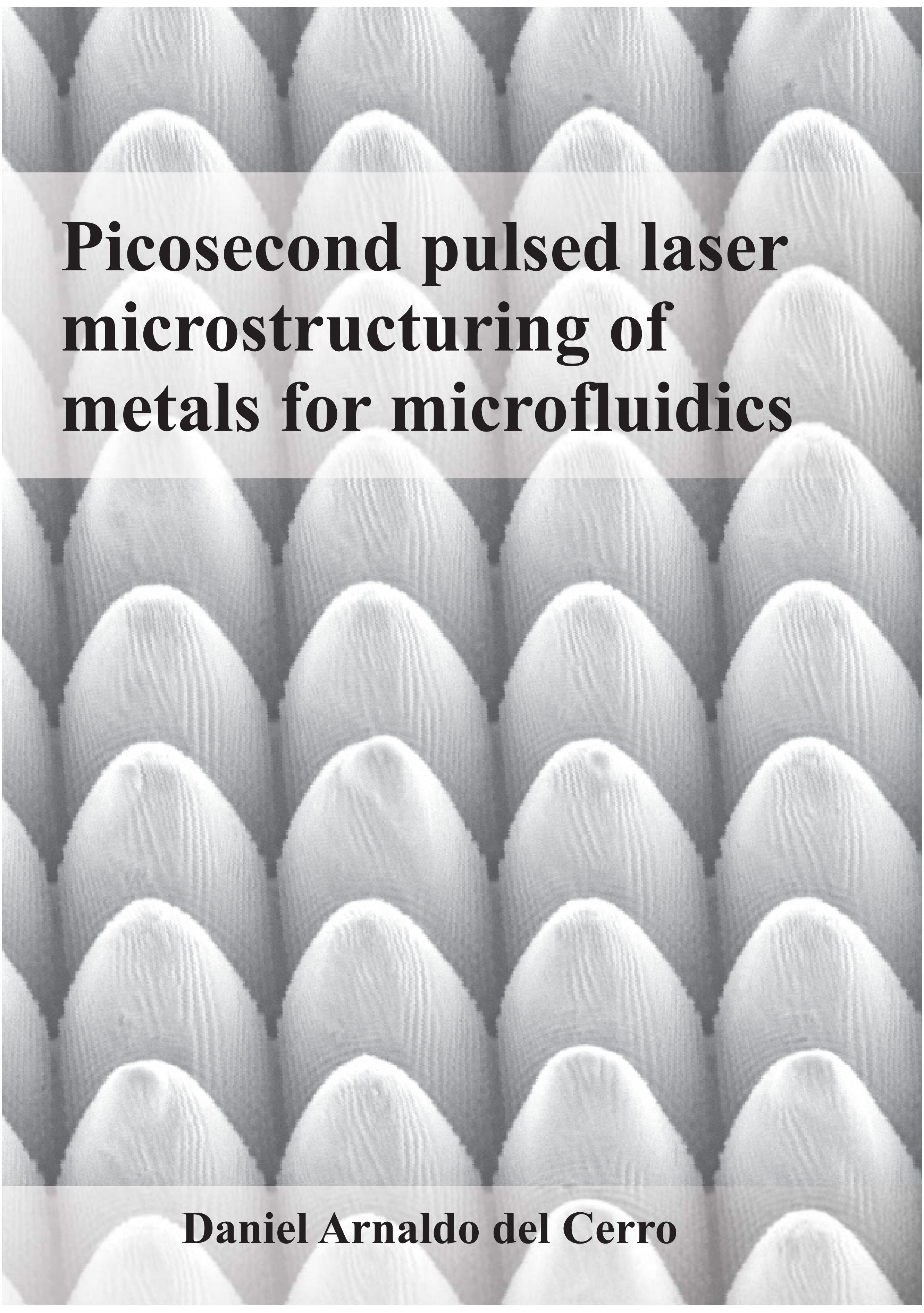

Picosecond pulsed laser microstructuring of metals for microfluidics

Daniel Arnaldo del Cerro

PICOSECOND PULSED LASER MICROSTRUCTURING OF METALS FOR MICROFLUIDICS

Daniel Arnaldo del Cerro

The research leading to these results has received funding from the European Community’s Seventh Framework Programme FP7/2007-2013 for the Clean Sky Joint Technology Initiative (JTI) under grant agreement N° CSJUGAM-SFWA-2008-001.

Composition of the graduation committee:

Chairman and secretary:
prof.dr. G.P.M.R. Dewulf, University of Twente

Promoter and assistant-promoters:
prof.dr.ir. A.J. Huis in ‘t Veld, University of Twente
dr.ir. G.R.B.E. Römer, University of Twente
dr.ir. M.B. de Rooij, University of Twente

Members:
prof.dr.ir. R. Akkerman, University of Twente
prof.dr.-ing. S. Barcikowski, University of Duisburg-Essen
prof.dr.ir. J.M.J. den Toonder, Eindhoven University of Technology
prof.dr.ir. R.G.H. Lammertink, University of Twente
prof.dr.ir. D. Lohse, University of Twente

The work described in this thesis was performed at the group of Mechanical Automation of the Faculty of Engineering Technology, Chair of Applied Laser Technology, University of Twente, P.O. Box 217, 7500 AE Enschede, The Netherlands.

Picosecond pulsed laser microstructuring of metals for microfluidics
Arnaldo del Cerro, Daniel
ISBN 978-90-365-3726-1

Printed by Gildeprint, Enschede, The Netherlands.

PICOSECOND PULSED LASER MICROSTRUCTURING OF METALS FOR MICROFLUIDICS

DISSERTATION

to obtain
the degree of doctor at the University of Twente,
on the authority of the rector magnificus,
Prof.dr. H. Brinksma,
on account of the decision of the graduation committee,
to be publicly defended
on Thursday 2nd of October 2014 at 16.45 hours

by

Daniel Arnaldo del Cerro

born on 5 November 1980
in Luarca (Spain)

This thesis has been approved by
prof.dr.ir A.J. Huis in't Veld, promoter
dr.ir. G.R.B.E. Römer, assistant-promoter
dr.ir. M.B. de Rooij, assistant-promoter.

Contents

Abstract

Micromachining with short and ultra-short laser pulses has evolved over the past years as a versatile tool that can be employed for the creation of microstructured surfaces. A microstructured surface modifies the way a fluid interacts with a solid surface. Surface microstructuring can then be employed to provide surfaces with certain functionalities. By proper adjustment of the laser machining conditions, well defined surface topographies can be created with sufficient accuracy. This allows to investigate the fluid/microstructured surface interactions. However, the relation between the applied laser parameters and the shape of the emerging microstructure has not been systematically studied in literature.

This thesis is dedicated to the study of some of the mechanisms underlying different fluid/microstructured surface interactions. First, an empirical model is developed for the prediction of the surface topography emerging from a process driven by short laser pulses. To this end, average ablated profiles are measured and employed for the simulation of the laser microstructuring process. The accuracy of the model is assessed by establishing a direct comparison between simulated and measured surface profiles. The model is shown to accurately reproduce the surface topography obtained from a laser micromachining process, within a certain processing window.

Next, the developed model is employed as a tool for the design of fluidic microstructures, as well as for the investigation of different fluidic functionalities, based on the generated microstructures. Moreover, simplified models are introduced, to relate the geometry of a microstructure to the fluid-microstructure interaction. This allows the calculation of the laser processing parameters that are required to obtain a desired functional microstructured surface. Furthermore, modifying key geometrical parameters, for example depths or slopes of the microstructure, allows investigating some of the fluidic mechanisms responsible for the functionality. Hence, additional knowledge on the fluid-microstructured surface interaction is gained by this approach.

List of publications

Parts of the work described in this thesis have been published in the papers listed below in chronological order.

- Römer, G.R.B.E., Arnaldo del Cerro, D., Sipkema, R.C.J., Groenendijk, M.N.W. and Huis in 't Veld, A.J. Ultra short pulse laser generated surface textures for anti-ice applications in aviation. In: Proceedings of the 28th International Congress on Applications of Lasers & Electro-Optics (ICALEO 2009), November 2-5, 2009, Orlando, Florida, USA. [Paper B in this thesis]
- Jagdheesh, R., Pathiraj, B., Gómez Marín, Á., Arnaldo del Cerro, D., Lammertink, R.G.H., Lohse, D., Huis in 't Veld, A.J. and Römer, G.R.B.E. Ultra fast laser machined hydrophobic stainless steel surface for drag reduction in laminar flows. In: Proceedings of the 11th International Symposium on Laser Precision Microfabrication (LPM 2010), June 7-10 June 2010, Stuttgart, Germany.
- Arnaldo del Cerro, D., Römer, G.R.B.E. and Huis in 't Veld, A.J. Picosecond laser machined designed patterns with anti-ice effect. In: Proceedings of the 11th International Symposium on Laser Precision Microfabrication (LPM 2010), June 7-10 2010, Stuttgart, Germany. [Paper A in this thesis].
- Arnaldo del Cerro, D., Römer, G.R.B.E. and Huis in 't Veld, A.J. Erosion resistant anti-ice surfaces generated by ultra short laser pulses. Physics Procedia, 5 (Part A) pp 231-235, 2010. URL: `http://dx.doi.org/10.1016/j.phpro.2010.08.141`
- Römer, G.R.B.E., Jorritsma, M., Arnaldo del Cerro, D., Chang, B., Liimatainen, V., Zhou, Q. and Huis in 't Veld, A.J. Laser micro-machining of hydrophobic-hydrophilic patterns for fluid driven self-alignment in micro-assembly. In: Proceedings of the 12th International Symposium on Laser Precision Microfabrication (LPM 2011) June 7-10, 2011, Takamatsu, Japan.

- Römer, G.R.B.E., Arnaldo del Cerro, D., Pohl, R., Chang, B., Liimatainen, V., Zhou, Q. and Huis in 't Veld, A.J. Picosecond Laser Machining of Metallic and Polymer Substrates for Fluidic Driven Self-Alignment. Physics procedia, (39) pp 628-635, 2012. URL: `http://dx.doi.org/10.1016/j.phpro.2012.10.082`

- Römer, G.R.B.E., Arnaldo del Cerro, D., Pohl, R., Chang, B., Liimatainen, V., Zhou, Q. and Huis in 't Veld, A.J. (2012) Picosecond laser machining of metallic and polymer substrates for fluidic self-alignment. In: Proceedings of the 7th International Conference on Laser Assisted Net Shape Engineering (LANE 2012), November 12-15, 2012, Fürth, Germany.

- Römer, G.R.B.E., Arnaldo del Cerro, D., Jorritsma, M.M.J., Pohl, R., Chang, B., Liimatainen, V., Quan, Zhou and Huis in 't Veld, A.J. (2012) Laser micro–machining of sharp edged receptor sites in polyimide for fluid driven self-alignment. In: Proceedings of the 13th International Symposium on Laser Precision Microfabrication (LPM 2012), June 12–15, 2012, Washington, USA.

- Arnaldo del Cerro, D., Gómez Marín, A., Römer, G.R.B.E., Pathiraj, B., Lohse, D. and Huis in 't Veld, A.J. Leidenfrost point reduction on micro–patterned metallic surface. Langmuir, 28 (42) pp 15106–15110, 2012. [Paper C in this thesis]. URL: `http://dx.doi.org/10.1021/la302181f`

- Gómez Marín, A., Arnaldo del Cerro, D., Römer, G.R.B.E., Pathiraj, B., Huis in 't Veld, A.J. and Lohse, D. Capillary droplets on Leidenfrost micro–ratchets. Physics of fluids, 24 (12) pp 1-10, 2012. [Paper D in this thesis]. URL: `http://dx.doi.org/10.1063/1.4768813`

Nomenclature

Roman characters

Symbol	Description	Units
$a(\phi)$	energy losses due to pressure waves	-
A	absorptivity	-
A_e	linear coefficient for the specific heat of electrons	J m^{-3} K^{-2}
c	volumetric heat capacity	J m^{-3}K^{-1}
c_e	electron volumetric heat capacity	J m^{-3}K^{-1}
c_i	lattice volumetric heat capacity	J m^{-3}K^{-1}
c_l	capillary length	m
C_s	speed of sound	m s^{-1}
D	thermal diffusivity	m^2 s^{-1}
E_{eff-th}	threshold energy for phase explosion	J m^{-3}
f	projected wet area	-
$F^{(c)}$	force exerted on a capillary drop	N
$F^{(s)}$	force exerted on a heavy drop	N
$h(x,y)$	ablated profile per pulse	m
$h_N(x,y)$	average ablated profile per pulse	m
$H(x,y)$	surface profile	m
H_{drop}	height of a drop	m
I	absorbed intensity	W m^{-2}
I_0	incident intensity	W m^{-2}
I_{th}	threshold intensity for ablation	W m^{-2}
l_{th}	thermal diffusion length	m
l_c	maximal penetration depth of energy	m
l_{e-ph}	electronic heat diffusion length	m
N_L	applied number of laser cycles	-
r	roughness ratio	-

Symbol	Description	Units
r_f	roughness ratio of the wet area	-
R	reflectivity	-
R_d	radius of a drop	m
T	temperature	K
T_a	activation temperature	K
T_m	melting temperature	K
T_{het}	temperature required for heterogenous nucleation	K
T_{ash}	available superheat	K
T_i	temperature at the solid-fluid interface	K
v	advancing velocity of the melting front	m s^{-1}
v_0	preexponential factor for the velocity of the melting front	m s^{-1}
w_0	beam waist	m

Greek characters

Symbol	Description	Units
α	linear absorption coefficient	m^{-1}
β	two-photon absorption coefficient	m W^{-1}
γ	surface tension	N m^{-1}
δ	optical penetration depth	m^{-1}
Δv_{fg}	change of specific volume from liquid to vapour	m^3 kg^{-1}
θ_c	critical contact angle	-
θ_Y	Young's contact angle	-
θ_r^w	apparent contact angle at Wenzel state	-
θ_r^c	apparent contact angle at Cassie-Baxter state	-
κ	thermal conductivity	$Wm^{-1}K^{-1}$
λ	latent heat of vaporization	J kg^{-1}
Λ	ratchet periodicity	m
ρ	density	kg m^{-3}
τ_{cr}	critical pulse duration	s
τ_{e-ph}	electron-phonon relaxation time	s
τ_p	pulse duration	s
τ_s	characteristic time for mechanical equilibration	s
ϕ_0	Incident fluence	J m^{-2}
ϕ	Absorbed fluence	J m^{-2}
μ	electron-phonon coupling coefficient	$Wm^{-3}K^{-1}$

Abbreviations

Abbreviation	Description
APCA	Apparent contact angle
CA	Contact angle
CA_{ad}	Advancing contact angle
CA_{rec}	Receding contact angle
CAH	Contact angle hysteresis
CHF	Critical heat flux
CLSM	Confocal laser scanning microscope
DLC	Diamond-like carbon
FOTS	Fluoro-octyl-trichloro-silane
fps	Frames per second
GD	Gas dynamics
HDMSO	Hexamethyldisiloxane
LFP	Leidenfrost point
LIPSS	Laser induced periodic surface structures
LWC	Liquid water content
MD	Molecular dynamics
NRMS	Normalized root mean square
PE-CVD	Plasma enhanced chemical vapour deposition
RMS	Root mean square
SEM	Scanning electron microscope
SHG	Second harmonic generation
THG	Third harmonic generation
TTM	Two-temperature model

1 | Introduction

1.1. Fluidics & microstructures

The interaction between fluids and solid surfaces manifests itself in a number of daily situations. It determines for example the shape of water drops sitting on a glass window after a rainy day. It also explains how certain insects, such as the *Gerridae* (water strider), are capable of sliding on the surface of water ponds. From a technical point of view, the friction experienced by a fluid as it flows close to a wall, is a critical parameter determining, e.g. the fuel consumption of an airplane, or the pressure losses along a pipeline.

Regardless the length scale of the system under consideration, the nature of these fluid-surface interactions lies at the inter-phase phenomena occurring at a microscopic level. A *surface topography*, i.e., the shape, size, orientation and spatial distribution of the surface features, in combination with the particular chemical composition of both the liquid and the surface, determine the fluid-solid surface interactions.

Perhaps one the most remarkable examples of a surface *functionality* which is given by a micro-metric sized surface topography can be found in nature.

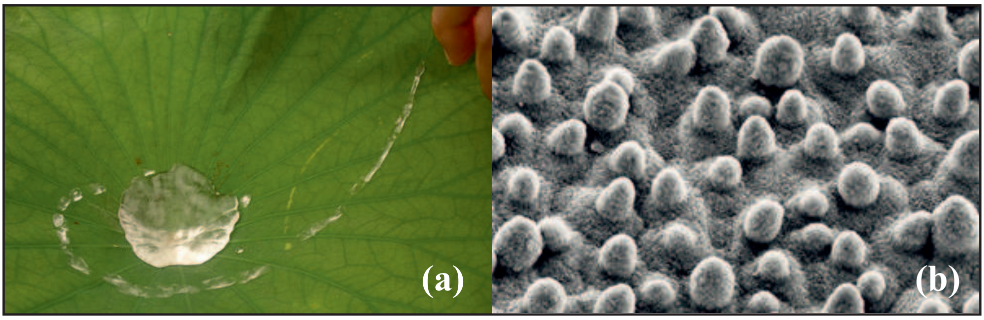

Figure 1.1.: The water repelling ability of the Lotus leaf, (a), is a result of a dual scaled micro- and nano-structured surface which is covered with hydrophobic waxes, (b). Image (a) © User:Saperaud / Wikimedia Commons / CC-BY-SA-3.0. Image (b) courtesy of W. Barthlott.

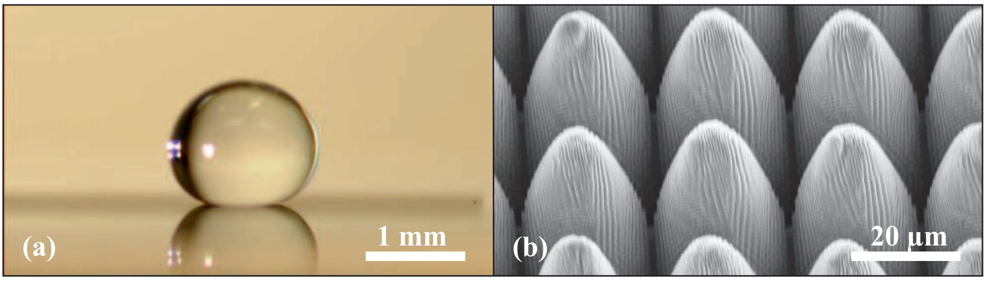

Figure 1.2.: A water drop sitting on top of a laser micromachined microstructure (a), and a SEM micrograph of the surface (b).

That is, certain leaves, like that of the *Nelumbo nucifera* (Lotus leaf) show an extremely water repellent surface, see figure 1.1. On these leaves, water drops bead up and easily roll off, taking away contaminants from the surface. This functionality can in part be attributed to the particular micrometric structure of the leaf, as was determined by Barthlott et al. in the late 1990s [1].

The surface micro-structure of the Lotus leaf has been mimicked by modern microfabrication techniques, to create artificial water repellent substrates [2–5]. These substrates mimic comparable surface features of the leaf, both in size and shape. The resulting water repellent properties were found to be similar or superior to those of the leaf [2–7], see figure 1.2. Moreover, a detailed analysis of the phenomena and the mechanisms leading to water repellency, allowed for a generalization of the effect. For example, Tuteja et al. accomplished the creation of a new micro-structure with *oleophobic* properties, that is, a surface capable of repelling non-polar organic liquids [8]. This shows how the study and design of a surface topography can be exploited to render surfaces with novel functionalities.

1.2. Surface micro-structuring with pulsed lasers

Creating functional surfaces requires an interdisciplinary approach, to design adequate surface profiles with respect to a particular fluid-microstructure interaction. To this end, different micro-fabrication techniques can be employed for the generation of these micro-structures on various materials.

Laser microstructuring with pulsed laser sources can be successfully employed as a microfabrication technique. Pulsed laser sources, particularly with pulse durations in the picosecond and femtosecond regime, have been increasingly employed for the creation of micro-metric sized features [9, 10]. These micro-metric sized features emerge as the result of a direct laser-induced material removal process, which is initiated by the absorbed optical energy. More specifically, in laser microfabrication, the energy of a laser pulse can be tightly

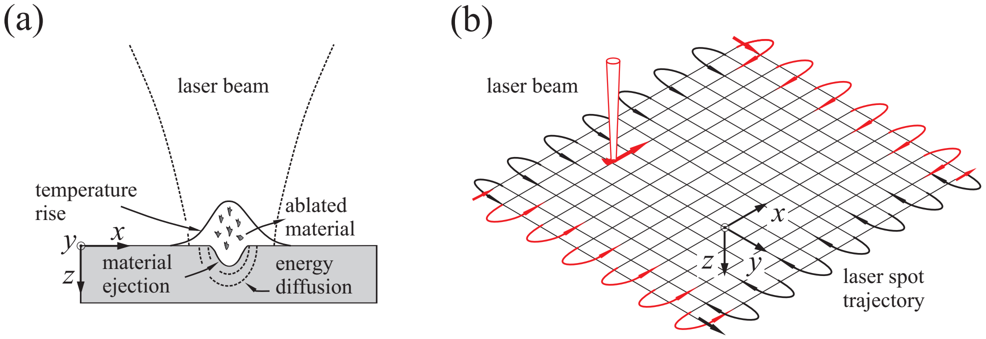

Figure 1.3.: A focused laser beam is employed for material processing (a). A laser beam can be scanned across an area to create micrometric surface topographies (b).

confined into a micro-metric sized focal spot. The absorbed energy triggers then different phase changes, leading to material removal, see figure 1.3(a). In this approach, a laser pulse removes a thin layer, typically of a few tens of nanometer. The high repetition rate of modern laser sources, which can reach up to several tens of GHz [11], allows for increased processing speeds. Beam guiding and focusing techniques allow scanning of the laser spot in arbitrary 2D patterns over the surface of the material, from which the resulting micro-structure emerges, see figures 1.2(b) and 1.3(b). As a focused beam interacts with an area, with a size comparable to that of the focal spot, most areas of the substrate remain unaffected and, therefore, undamaged. The local modification allows accurate processing of a wide range of materials, but limits in turn the processing speed.

Unfortunately, the relation between the created micro-structure and the achieved (fluidic) functionality has been only partially studied and discussed in literature. The surface evolution upon laser-induced material removal, together with key processing parameters like pulse energy, or pulse spatial distribution is not well known. In addition, a model capable of predicting and relating topographical laser-induced changes of the surface with the achieved (fluidic) functionality is missing.

1.3. Problem definition

This thesis is dedicated to the study of the phenomena occurring at the interface between a fluid and the surface of a laser-induced micro-structured substrate. Periodic surface micro-structures with a well-defined geometry are created by processing selected substrates with ultra-short laser pulses. Ultimately, the physical mechanisms that are responsible for the interactions can be demonstrated, along with the required *surface topography* leading to the functional surface.

Only a limited number of studies aimed at predicting surface topographies after processing with short and ultra-short laser pulses are available in literature. Moreover, the accuracy of the predicted surface topography in these few studies is insufficient for studying the effects of a (changing) topography on a particular fluid/micro-structure interaction. That is because small changes on local slopes or depths of the topography can have a significant influence on the fluidic interaction. Therefore, the problem addressed in this thesis is defined as:

"Develop a method to be employed for the prediction of a surface profile emerging from a material removal process by ultra-short laser pulses, to an extent allowing the design of a functional surface and study a particular fluid / microstructured surface interaction."

Two derived questions can be inferred from this problem definition, to which the two main parts of this thesis are dedicated:

I) Is it possible to predict, for a given short pulsed laser source and processing conditions, the resulting geometry of the features on the surface of a substrate?

And secondly;

II) What additional knowledge can be gained regarding the interaction of a particular fluid with a microstructured surface obtained by ultra-short pulsed laser processing?

Some of the mechanisms which are responsible for the particular fluid/microstructured surface interaction are not fully understood. By proper adjustment of the laser machining conditions, well defined surface topographies can be created with sufficient accuracy. The method to be developed should then allow for a systematic study of a changing surface topography, with respect to the fluid micro-structure interaction. Further, the method can be exploited as a design tool to directly obtain processing conditions leading to the functional surface. In addition, a proper selection of processing parameters can substantially minimize the required time for laser processing, which is currently one of the main limitations for industrial application of laser micro-machining with ultra-short laser pulses.

1.4. Thesis outline

This thesis is divided into two main parts. The first part addresses the first research question mentioned above. That is, a method is developed and discussed which predicts the generated surface topography for a given material, laser setup and processing conditions. The limitations and, thus, the applicability range of the method are also discussed.

Chapter 2 introduces previous work aimed at predicting a surface topography resulting from a laser microstructuring process. The different reported modelling approaches are discussed in terms of accuracy and applicability for predicting the resulting fluidic functionality of the generated microstructure.

Chapter 3 addresses the fundamentals of material processing with short and ultra-short laser pulses. A method is proposed for the prediction of the surface evolution upon material removal with ultra-short laser pulses. Chapter 4 is aimed at the experimental validation of the proposed method, in order to find the range of application of the model for a selected combination of material & laser source.

The second part of the thesis addresses the second research question. Chapter 5 introduces several examples of laser-generated functional microstructures. Chapters 6 and 7, employ the method developed in chapter 3 to determine suitable geometries leading to a desired fluid/microstructure interaction. Different micro-structures are created to investigate experimentally the effect of a geometry on the fluidic functionalities. The added functionalities are explained based on the created topographies.

Finally, chapter 8 presents conclusions of the proposed approach, including suggestions for further research.

Part I.

Surface micro-structuring with short laser pulses

2 | State of the art

This chapter describes the state of the art in the creation of surface microstructures by short and ultra-short laser pulses. Existing attempts to predict a surface topography, and the resulting added fluidic functionality after a laser microstructuring process, are presented. The different reported modelling approaches are then discussed in terms of accuracy and applicability for microfluidics.

2.1. Surface microstructuring with pulsed lasers

The material removal process by means of pulsed lasers is commonly referred to as *laser ablation* [12]. The surface modification created by laser ablation from a single pulse, in terms of shape and dimensions, is here referred to as an *ablated profile*. This ablated profile is denoted as *h(x,y)*, where *(x,y)* are the coordinates of a point lying in a horizontal plane, and h is the vertical coordinate, or depth (in meters), at that point. Fundamental research into the laser material interactions leading to ablation, and to the prediction of the resulting ablated profile $h(x, y)$, have been extensively pursued both for practical and scientific reasons. Determining single pulse ablated profiles, $h(x, y)$, is a first step in order to calculate a surface profile, $H(x, y)$, that is the microstructure emerging from a micromachining process involving numerous laser pulses.

The calculation of an ablated profile $h(x, y)$ from the laser & material parameters requires to consider the main physical mechanisms of the laser-material interaction. That is, a laser pulse arriving at an absorbing medium initiates several mechanisms upon absorption, that may result into phase changes, so material is removed from the target. Models for laser ablation can be categorized by the duration of the pulse. That is because different physical mechanisms drive the process as the pulse duration is varied, see figure 2.1. It should be noticed that there is not a sharp transition between a *short* and a *long* pulse processing regime.

In this work, a laser pulse is considered to be *long* when its duration is above

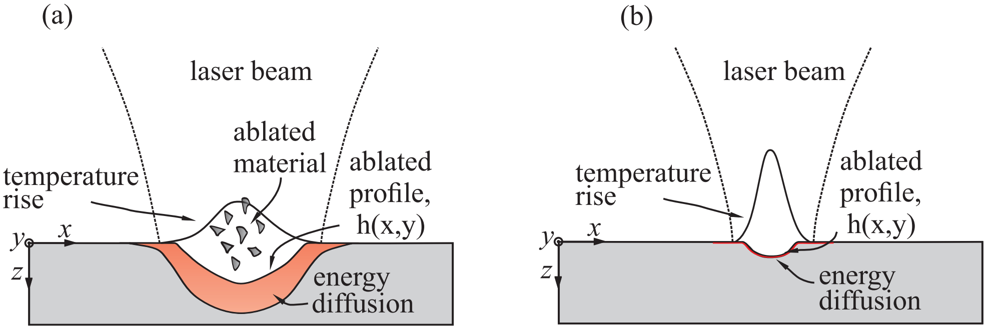

Figure 2.1.: Laser ablation with long (a), and ultra-short (b) laser pulses. Material processing with long laser pulses is characterized by large(r) ablation rates and diffusion of energy deeper into the material than in the case of processing with ultra-short laser pulses. Processing with ultra-short laser pulses leads to reduced ablation rates and a limited heat diffusion into the bulk, which does, in turn, increase the accuracy of a laser micromachining process.

a certain calculated critical value, typically in the order of one nanosecond, and *short* when below, that is, pulse durations in the pico- and femtosecond regimes. The reasons for this division on the basis of pulse duration are discussed qualitatively in sections 2.3 & 2.4, as will be shown, the pulse duration has practical consequences for the calculation of ablated profiles, and thus for the design and selection of a laser micromachining process. The numerical calculation of critical pulse durations is discussed in more detail in chapter 3, section 3.2.1.

Because the response of a material to the irradiation conditions depends strongly on the temporal intensity profiles of a laser pulse, different modelling approaches have been developed, to account for the different phenomena characterizing the *short* and *long* pulse duration regimes. It should be noted that some of these mechanisms, which are responsible for the material removal process, are still under investigation. Previous research efforts have been aimed at demonstrating fundamental mechanisms of ablation, rather than at predicting a particular ablated, *h(x,y)*, or surface profile, *H(x,y)*, for given laser processing conditions.

However, it has been shown that laser ablation with (ultra) short laser pulses is a suitable technique for the creation of microstructures with a relatively high degree of control on the resulting geometry [9, 10], and providing a substrate with a variety of functionalities, which are discussed in section 2.5.

The selection of the laser processing conditions leading to a particular functional microstructure is not a trivial task. That is because a microstructuring process requires to consider, together with the ablation process, the changes on a surface profile created by material removal from subsequent laser pulses.

Further, the strategy of guiding (or the trajectory of) the laser spot over the surface of the substrate, i.e., the “location” of the laser pulses across the area to be processed has to be selected.

Then, the creation of a functional microstructure requires first studying the laser ablation process, to determine the mechanisms leading to material removal. This step allows for the calculation of ablated profiles, $h(x, y)$, which are necessary, in a next step, for the design of a microstructuring process (strategy), and the creation of a functional surface. The next sections summarize previous work on modelling laser ablation, calculating ablated profiles, and the creation of microstructures by pulsed lasers, including both the long and short pulse regimes.

2.2. Fundamentals of laser–material interaction

This section presents a summary on the state of the art in understanding the physical phenomena occurring during laser ablation. The response of a material upon irradiation with laser pulses follows a sequence of possibly overlapping phenomena, depending on the pulse duration, intensity and the physical properties of the substrate [13]. That is, the ablated profile $h(x, y)$ created on a substrate by laser pulses is determined by a combination of the following phenomena:

- absorption of laser energy,
- establishment of an electron temperature,
- thermalization of the lattice,
- phase changes, including ablation, and
- dissipation of residual energy,

which will be discussed in more detail below.

Absorption

The first step in the laser material interaction consists of the absorption of optical energy by the substrate. The energy transfer starts via the interaction of photons with optically active *excitations*, like the free electrons in the conduction band of a metal [14]. An *optically active excitation* is an energy state that can be excited by a photon. In semiconductors, the incident photons can interact with, for example, electron-hole pairs, vacancies or other energetic states, like those associated with defects or impurities [14]. In insulators, the optically active excitations are electrons forming the covalent bonds of the lattice. Due to their large band gap, a direct excitation of these electrons in insulators only occurs if the photon has sufficiently high energy.

Different non-linear processes, like multiple photon absorption, also contribute to the absorption of optical energy, particularly at the high intensities of an ultra-short laser pulse [13, 14]. The existence of defects in a crystalline structure, like vacancies or dopants, can enhance (non-linear) absorption [14]. Once the conduction band has reached sufficient occupancy, processes related to avalanche ionization, are responsible for creating a sufficient amount of *free carriers*, which results in further linear absorption of optical energy via inverse Bremsstrahlung [15].

In the case of a metal, the electrons already occupy the conduction band, thus linear absorption is the dominant absorption mechanism [14].

Establishment of an electron temperature

After the electrons absorbed the laser energy, a temperature distribution is established in the electron gas. Figure 2.2 shows the redistribution of energy in the electron subsystem due to absorbed laser energy, showing the occupancy of density of energy states upon absorption of optical energy, from room temperature conditions, (a), during excitation, (b), and after further thermalization of the electron subsystem. This establishment of a temperature distribution within the electron gas occurs via electron-electron scattering. This process requires a certain time, approximately of a few tens of femtoseconds [16]. During this time interval, diffusion of *ballistic electrons* into the bulk takes place, see figure 2.2(b). If the laser pulse duration is comparable to this time scale, the ballistic motion of electrons has to be considered for an accurate calculation of penetration depth of the absorbed laser energy. The required time for thermalization of the electron gas increases the penetration length (depth) of the absorbed energy beyond the optical penetration depth, δ. The later is related to the linear absorption coefficient α as $\delta = 1/\alpha$.

Thermalization of the lattice

The electron subsystem dissipates its energy into the lattice at a rate, which is related to the so-called electron-phonon coupling strength, which is a material property. The lattice is usually considered to increase its temperature as a result of electron-phonon collisions, that is, the lattice can be modeled as an array of oscillators, being a *phonon* the energy level associated to the vibration of the lattice [17]. The characteristic relaxation time required for the thermal equilibrium between electron and lattice ranges from about 1 to 100 picoseconds, depending on the material under consideration [14, 18]. Hence, the diffusion of energy into the bulk depends on the transfer rate of energy between the thermalized electron system and the lattice. As a consequence, the electron-phonon coupling time has then to be considered for the calculation

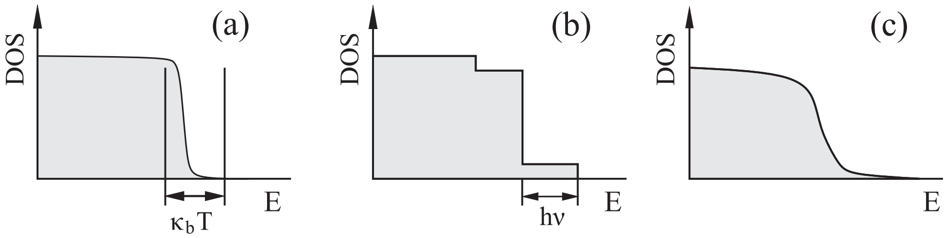

Figure 2.2.: Establishment of an electron temperature distribution upon absorption of optical energy; (a) occupancy of density of states (DOS) at energy levels, E, corresponding to room temperature, T, (b) transitional energy redistribution upon absorption of a photon of energy $h\nu$, where h is Planck's constant and ν is the photon frequency, and (c) re-establishment of an energy distribution upon electron thermalization. Adapted from Wellershoff et al. [16].

of the temperature rise of the lattice.

Phase changes: Ablation

Phase changes in the material may occur when the absorbed intensity reaches a sufficient level. In general, two different ablation regimes have been reported in literature, when processing with short laser pulses [19]. A low fluence regime, in which the maximal depth of the ablated volume is of the same order of magnitude as the optical penetration depth, and a high fluence regime. The later, commonly referred to as the *thermal regime*, is characterized by higher ablated depths, and a reduced machining quality when compared to processing conditions within the optical regime.

Typical removal depths per pulse in the *long* pulse regime are measured to be in the micrometric range [12]. This relatively large removal rate implies a reduced processing time, but limits, in turn, the accuracy of the microstructuring process. The ejection of molten residues and recast material in this fluence regime is prominent, which further reduces the accuracy. As an example, figure 2.3 shows the qualitative effects of the pulse duration on the resulting ablated profile on a stainless steel substrate. As the pulse duration is varied from 200 femtoseconds (a), to 80 picoseconds (b) and 3.3 nanoseconds (c), the amount of recast and molten material significantly increases. For these reasons, it is difficult to create microstructures with a predefined geometry when processing within the long pulse regime.

Processing materials at a low fluence allows for an increased control over the ablated depths and the microstructuring process in general, due to the resulting limited (thermal) energy transfer to zones adjacent to the laser material interaction volume [9, 10].

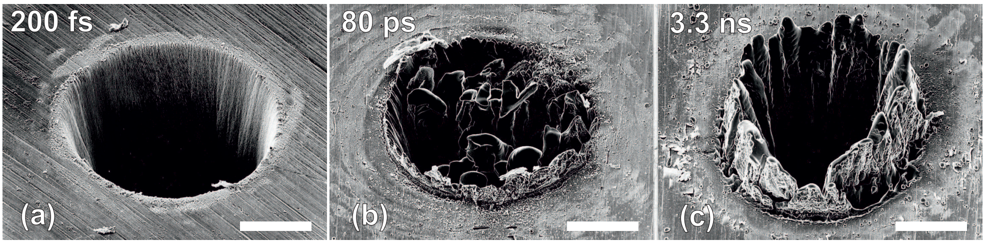

Figure 2.3.: Percussion drilling of stainless steel with pulse durations of: 200 fs (a), 80 ps (b), and 3.3 ns (c), reproduced from [20]. The length of the scale bar is 60 μm.

Dissipation of residual energy
Any residual energy which was not used to remove the material diffuses as heat into the bulk, until thermal equilibrium with environment is reached. A microstructuring process requires a large number of pulses, which arrive at the target with a temporal delay given by the laser repetition rate (or pulse frequency). If the time in between pulses is sufficiently short, the thermalized residual energy may accumulate and increase the temperature of the lattice [17] as a whole. This heat accumulation affects the ablation process [17].

2.3. Laser ablation with long laser pulses

In general, for a sufficiently long pulse, the absorbed incident laser energy can be considered to be instantaneously transferred to the substrate in terms of heat [14]. As a result, the laser (pulse) can be modelled as a heat source, that raises the temperature of the target upon instant absorption of the optical energy. The corresponding classical *heat conduction equation*,

$$c\,\frac{\partial T}{\partial t} = c\,v\,\frac{\partial T}{\partial z} + \frac{\partial}{\partial z}\left(\kappa \frac{\partial T}{\partial z}\right) + I_0\,A \exp(-\alpha\,z), \tag{2.1}$$

where T is the temperature of the substrate, c is the heat capacity, κ is the thermal conductivity, v is the advancing velocity of the ablation front, I_0 is the incident intensity, A is the absorptivity and α is the absorption coefficient. Equation 2.1 can be solved to determine the spatial and temporal temperature evolution of the lattice.

In contrast to shorter laser pulses, the moderate intensity and relatively long duration of the laser pulses, results in a relatively *slow* temperature rise of the lattice. That is, the lattice does not experience significant overheating [14]. As a consequence, the material removal process can ben described as a conventional evaporation process, occurring at quasi-equilibrium conditions [12, 14]. This is of particular relevance, as material evaporation at a temperature close to equilibrium conditions is a well-known process. That is, it is described by a *kinetic* equation relating the evaporation velocity of the material, v, to the surface temperature, T, as,

$$v = v_0 \exp\left(\frac{-T_a}{T}\right), \tag{2.2}$$

where the factor v_0 takes values in the order of the speed of sound and T_a is referred to as the activation temperature [21].

The modelling approach for the calculation of an ablated profile $h(x, y)$ then consists of solving the classic heat equation (2.1), taking into account temperature dependent material properties. When the absorbed energy density at a given location is sufficient to melt and vaporize the substrate, the material can be considered as being removed. The integration, over time, of the evaporation velocity, given by the kinetic equation (2.2), yields then the ablated profile, h, as

$$h = \int v(t)\, dt. \tag{2.3}$$

However, some additional phenomena usually occur when processing with long pulses. Pulse durations of about 10 ns have been shown to interact with the ablation products. Then screening of the surface due to the plasma and/or a vaporized material plume has to be considered [12, 14]. Some authors have modelled the resulting attenuation of the incident energy, by calculating an effective absorption coefficient in the plasma [12, 14]. In addition, the energy diffusion from the interaction zone, as well as the hydrodynamics of the molten layer and the (plasma) plume have also to be considered in order to predict a resulting ablated profile [12].

Surface microstructuring with long laser pulses

Next, modelling of the creation of a full surface profile, $H(x, y)$, after a multipulsed process involves several steps. The previously described quasi-equilibrium thermal model can be employed to calculate the ablated profile, $h(x, y)$, after single pulse processing. Extending the analysis to microstructuring of a surface requires studying additional effects, which are related to progressive (pulse to pulse) change of the overall surface profile.

Although the ablation mechanisms in the *long* regime have been relatively well described, and corrections can be made for taking into account, e.g., the effect of tilted walls on reflectivity [22], there are phenomena related to the formation and redeposition of molten layers that reduce the reproducibility of the material removal process. These molten layers are excited during the *long* excitation stage of the pulse [12]. It has been shown that the hydrodynamics of these excited layers are hard to model [23]. In addition, only a few attempts

Table 2.1.: Modelling approaches for ablation by laser pulses with a FWHM duration equal to, or longer than, 1 ns.

Author	Material	Ablated profile[1]	Surface profile[2]
Anisimov et al. [12]	Polymers	1D	No
Kuper et al. [24]	Polymers	1D	No
Sinkovics et al. [25]	Polymers	3D	No
Vatsya et al. [26]	Metals	3D	No
Schwarz-Selinger et al. [27]	Silicon	3D	No
Pedder et al. [22, 28]	Polymers	3D	3D
Gower et al. [29]	Polymers	3D	3D

[1] An ablated profile is considered to be 1D when the model does not consider a spatial laser intensity profile. [2] A surface profile is considered to be 3D when the effect of spatially overlapping laser pulses on the resulting *surface topography* has been studied.

have been performed to study the surface evolution after partially spatially overlapping laser pulses. Table 2.1 lists a few examples of modelling attempts. The accuracy and applicability of these models for the prediction of a resultant surface topography $H(x, y)$ are, in any case, limited by the stochastic nature of the ablation process with long pulses.

2.4. Laser ablation with short & ultra-short laser pulses

As the pulses become shorter, several mechanisms alter the diffusion of energy into the lattice and the consequent phase changes, providing that the absorbed intensity suffices for phase changes. As a consequence, the laser (pulse) can no longer be considered as a simple surface heat source.

Kaganov et al. [30] first described the mechanism for the energy transfer between electrons and the ions of a lattice. In a series of publications [31–33], Anisimov et al. proposed a model to calculate the energy transfer rate between the electron and lattice subsystems during short pulsed laser processing, which was thereafter called the Two Temperature Model (TTM). The TTM has been widely employed and experimentally validated for the calculation of the temperature evolution of a substrate exposed to ultra-short laser pulses [10, 12, 14, 21, 34, 35].

A description of the ablation process requires, in addition to the TTM, the consideration of the microscopic phenomena leading to a phase change. In the (ultra) short pulse duration regime, the substrate is exposed to different phenomena, as for example the propagation of pressure waves, occurring at the same time scale as the propagation of melting fronts and/or the homogeneous nucleation of liquid and/or void volumes [36,37]. As a consequence, the material removal process differs qualitatively from the classical surface evaporation at quasi-equilibrium conditions, characteristic of processing with long laser pulses, as described in the previous section.

Techniques like Gas Dynamics (GD), Molecular Dynamics (MD) and Monte Carlo (MC) simulations allow the study of the different ablation mechanisms occurring at this short laser pulse regime [18, 36–39]. These numerical tools are capable of including a complete description of the physical phenomena, regardless the nature of the phase changes. That is, a *kinetic* equation (in the form of equation 2.2), accounting for the mechanisms responsible for the phase changes, is not required in this case. In addition, the absorption, energy transfer and consequent temperature rise of the lattice can be simultaneously computed when combining molecular and/or gas dynamics, [18, 38], or employing a standard or modified TTM for the calculation of the temperature evolution of the system [40].

These hybrid modelling approaches allow for a complete description of laser ablation, from the absorption of optical energy to the final ejection of material. An overview of the different modelling approaches that can be found in literature is listed in table 2.2.

Ivanov and Zhigilei [41], Perez et al. [39] and Lorazo et al. [18] applied Molecular Dynamics simulations to identify the thermodynamical pathways leading to material removal from metallic substrates exposed to short & ultra-short laser pulses. The high absorbed intensities were shown to result into a largely overheated lattice. In addition, a collection of transient, thermodynamically unstable, states were shown to take place, as a function of the pulse duration and intensity. These thermodynamical paths are characteristic of different ablation mechanisms, and are further discussed below.

Hence, the combination of optical, thermal and mechanical phenomena, for a given laser pulse temporal and spatial intensity profiles, have to be simultaneously analyzed to determine the ablation mechanisms [18]. Identifying the actual laser ablation mechanisms, occurring at given processing conditions, is a required step for the calculation of an ablated profile $h(x, y)$. The main mechanisms for ablation are further discussed below.

Ablation mechanisms

The possible mechanisms for material removal, at increasing intensity levels, which were identified from detailed MD analysis are, respectively, spallation, homogeneous nucleation, heterogeneous nucleation and fragmentation, [18,36, 39,45]. A schematic overview of these mechanisms is shown in figure 2.4, and will be discussed briefly, with reference to figure 2.5.

Table 2.2.: Modelling approaches for ablation processes with ultra-short laser pulses.

Author(s)	Material	Temperature evolution[1]	Phase change[2]	Ablated profile[3]
Ivanov and Zhigilei [41]	Metals Semiconductors Dielectrics	MD-MC	Spallation Homogeneous nucleation Heterogenous nucleation Fragmentation Vaporization	No
Jandeleit et al. [42]	Metals	TTM	Vaporization	No
Laville and et al. [43]	Metals	GD	Vaporization	1D
Anisimov et al. [38]	Metals	TTM-GD	Vaporization	1D
Momma et al. [15]	Metals	TTM	Vaporization	1D
Hu et al. [44]	Metals	TTM	Vaporization	3D
Perez and Lewis [39]	Metals Semiconductors Dielectrics	MD-MC	Spallation Homogeneous melting Fragmentation Heterogeneous melting Vaporization	3D

[1] GD = gas dynamics, MD = molecular dynamics, TTM = two-temperatures model, MC = Monte-Carlo simulations. [2] Mechanisms phase changes, see text for details. [3] An ablated profile is considered 1D when a direct relation depth / energy input is given, without taking into account an intensity profile. An ablated profile is considered 3D when a spatial laser intensity profile is included.

- Mechanical spallation. This ablation mechanism occurs at low laser fluence levels, and dominates the material removal process for fluences just above the melting threshold [39]. The formation and aggregation of voids below the surface of the substrate, and the consequent relaxation of stresses, results in the ejection of a condensed top layer, see figure 2.4 and figure 2.5(a). The later figure shows a schematic view of the identified temperature-density transient states of the material during the ablation

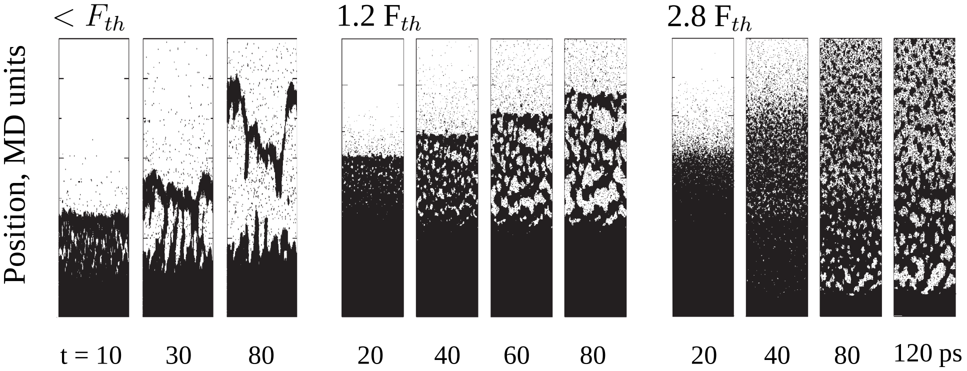

Figure 2.4.: Results of Molecular Dynamic simulations, illustrating several mechanisms for laser ablation with ultra-short laser pulses: spallation, (a), fragmentation, (b) and vaporization, (c). F_{th} represents the minimum absorbed fluence required for material removal. Reproduced from [39].

process. This mechanism becomes significant at the, so-called, regime of stress confinement. This regime is described by the inequality [37]:

$$max\{\tau_{e-ph}, \tau_p\} \leq \ \tau_s \approx \frac{l_c}{C_s}, \tag{2.4}$$

where τ_{e-ph} is the time required for the thermalization of the lattice, τ_p is the pulse duration, τ_s is a characteristic time of mechanical equilibration, l_c is the penetration depth of the absorbed laser energy, and C_s is the speed of sound in the material. As an example, the upper pulse duration leading to stress confinement for stainless steel is about 10 ps, assuming $l_c \approx 10$ nm and $C_s \approx 10^3$ m/s.

- Heterogeneous and homogeneous nucleation. At fluence levels higher than those required for spallation, ablation has been shown to proceed after either the nucleation of gas in the bulk of molten layer (homogeneous nucleation), or from a moving melting front (heterogeneous nucleation) [39]. Some authors consider homogeneous nucleation as a particular case of spallation, as the material removal is mainly the consequence of relaxation of thermoelastic stresses [36]. Sudden homogeneous nucleation of a gas phase within the bulk of a molten layer, and the consequent ejection of largely overheated condensed matter, is the proposed mechanism for the ablation process usually referred to as *phase explosion*, see figure 2.4(b) and 2.5(b).

- Fragmentation. At a sufficiently high level of absorbed intensity, a direct, non-thermal driven, material decomposition takes place. According to

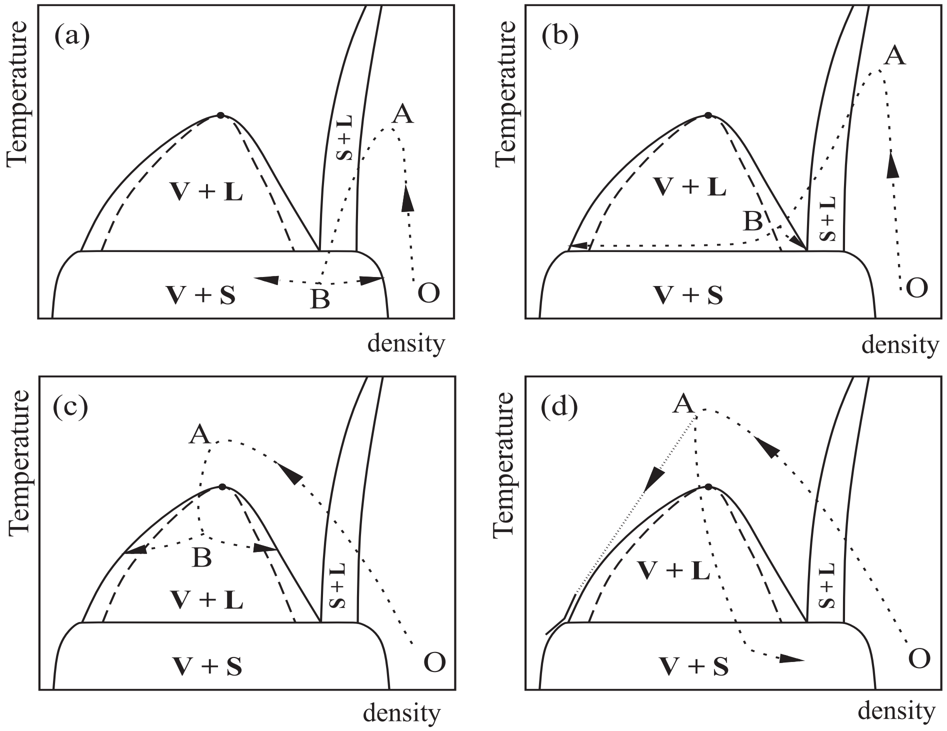

Figure 2.5.: Thermodynamic pathways for the state (V=vapour, L=liquid, S=solid) of ablated material with ultra-short laser pulses at increasing fluence: (a) spallation, (b) heterogeneous nucleation, (c) fragmentation and (d) vaporization. Dotted lines with arrows indicate temperature-density transient states, as calculated via Molecular Dynamics, for example by Perez et al. [39]. The fine dotted line in (d) is meant as a visual guide to follow the time evolution.

this mechanism, material directly decomposes into a collection of clusters and a partially atomized cloud, see figure 2.4(c) and 2.5(c). The decomposition occurs at a pressure-temperature pair *above* the spinodal, see figure 2.5(c). This is an indication of a mechanism that differs qualitatively from nucleation, as the system enters the liquid-vapour unstable area of the temperature-density diagram only after material ejection [39].

- Vaporization. When the fluence is further increased, a direct non–thermal transition into a gas behaving state occurs without cluster formation, see figure 2.5(d) [39].

The calculation of an ablated profile $h(x, y)$, based on the processing conditions, would require exact knowledge of the main ablation mechanisms relevant to these particular conditions for the material under consideration. Unfortunately, this exact knowledge is usually missing. For example, Perez et al. [39], based on MD simulations, proposed a simplified equation for calculating the ablated depth when phase explosion is the dominant mechanism. The ablated depth, $h(\phi)$, as a function of the incident local fluence, ϕ, is then given by

$$h(\phi) = \frac{1}{\alpha} \ln \frac{\alpha\phi[1 - a(\phi)]}{E_{eff-th}}, \tag{2.5}$$

where α is the linear absorption coefficient, $a(\phi)$ is a factor quantifying the energy losses due to the creation of a pressure wave, and E_{eff-th} is threshold energy density required for phase explosion. The predicted values are in accordance with experimental data for a sufficiently large range of incident fluence. However, this model underestimates the ablated depth at relatively low fluence levels [39]. If the energy losses due to the formation of pressure waves are neglected ($a(\phi)$=0), equation 2.5 simplifies to the well-known expression for the ablated depth

$$h(\phi) = \frac{1}{\alpha} \ln \frac{\alpha\phi}{(\alpha\phi)_{th}}, \tag{2.6}$$

which has been widely employed to describe the measured ablated depths obtained after short pulsed laser processing [14, 15, 19, 20], and it is further discussed later on this section.

Calculation of ablated profiles

An accurate calculation of an ablated profile, $h(x, y)$, based on laser processing conditions, requires overcoming several practical issues. First, the actual ablation mechanisms leading to material removal from a single pulse, particularly when the pulse has a given spatial intensity profile, are not unique. In addition, quantitative values of material properties are frequently unknown for most of the common paths for laser ablation in this regime. Further, the dynamics of pressure waves, are highly dependent on temperature gradients [39]. As a consequence, the mechanisms of material removal may vary strongly both in space and time.

In spite of the complex nature of the ablation process, laser microstructuring with ultra-short laser pulses has been experimentally shown to be a reproducible process, in terms of average ablated depth per pulse and generated ablated profiles [10, 20, 46]. Further, the generated surface features show a well defined geometry that can be adjusted by selecting an adequate pulse energy and pulse duration [9, 10].

Experimental determination of ablated profiles

Besides modelling based on physical phenomena, the ablated profile $h(x, y)$ could be determined by experiments. Nolte et al. [19] studied for the first time the ablation of copper with pulses ranging from 500 fs to 5 ps . Two different ablation regimes were identified, as a function of the absorbed fluence. The ablated depth per pulse, h, obtained at fluence levels below 0.5 J/cm^2, was found to be described by

$$h = \alpha^{-1} \ln \frac{\phi}{\phi_{th}^{\alpha}}, \tag{2.7}$$

where α is the linear absorption coefficient, ϕ is the absorbed fluence and ϕ_{th}^{α} is the experimentally determined fluence threshold for the onset of ablation. When the fluence was increased over 0.5 J/cm^2, a second ablation regime, characterized by larger ablated depths, was observed. The ablated depth for this regime was found to be described by

$$h = l \ \ln \frac{\phi}{\phi_{th}^{l}} \tag{2.8}$$

where l was identified as the energy diffusion length due to electronic heat diffusion, and ϕ_{th}^{l} is the fluence threshold for the onset of ablation in this regime. When the pulse duration was increased over 20 ps, the logarithmic dependency of equation(2.8) was lost, and the measured ablated depths decreased. The accuracy of these empirical expressions, equations (2.7) and (2.8), for the calculation of ablated profiles is further discussed in chapter 3.

Calculation of surface profiles

Few studies have been performed aimed at predicting the resultant ablated profile $H(x, y)$ emerging from a microstructuring process with multiple ultra-short laser pulses, [47, 48]. Due to the difficulties in establishing accurate relations between applied fluence and ablated depth or profile $h(x, y)$, an empirical approach is typically employed. In particular, calibration curves were determined in order to relate the incident fluence to the resulting ablated depths [47, 48]. A complete description of a microstructuring process would require, in addition, a description of the effects of a multi-pulsed response and, further, the selection of a path (x, y, t) of the laser pulses that leads to a desired microstructure.

2.5. Laser-generated functional microstructures

Processing with ultra-short laser pulses has been employed by several authors for the creation of a number of functional microstructures in the field of fluidics. The surface profiles after laser processing were found to show improved characteristics, such as better water repellency or reducing the drag experienced by a fluid in contact with the microstructured surface.

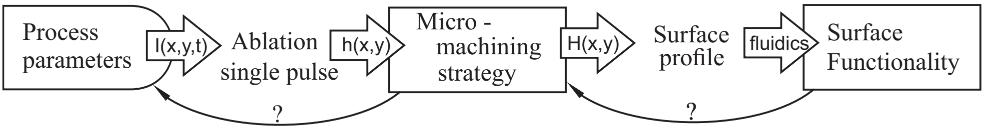

Figure 2.6.: Creating functional microstructures can be accomplished by following the surface evolution from a suitable microstructuring process. A laser pulse with an intensity density profile $I(x, y, t)$ generates an ablated profile $h(x, y)$. Multiple laser pulses create a surface profile $H(x, y)$ providing a surface with a desired fluidic functionality.

More specifically, Zorba et al. [3] and Baldacchini et al. [49] employed a femtosecond pulsed laser source to create water repellent surfaces on a silicon substrate. Similar wetting behaviour was accomplished by Cardoso et. al [2] and Yoon et al. [50] on polymeric substrates with picosecond pulses.

Kietzig et al. [51], Bizi-Bandoki et al. [52] and Wu et al. [53] have shown how certain metallic substrates may gain water repellent properties directly after processing with femtosecond pulses. Picosecond pulsed lasers have been employed for the creation of master moulds, from which a functional replica showed to gain water repellent properties [54, 55].

Different micrometric-sized structures were also achieved by direct material removal to obtain surfaces with new functionalities. Channels for microfluidic applications were created with femtosecond pulsed laser processing of polymeric substrates [56–59]. Osellame et al [60] employed a femtosecond laser to fabricate both microfluidic channels and optical waveguides on a glass substrate. Ribleted microstructures created on metal substrates by picosecond laser pulses have been shown to reduce the drag experienced by a fluid flowing over the microstructure [61].

Unfortunately, the relation between the different observed (fluidic) functionalities and the laser processing parameters is unknown. The above studies do not provide insight, nor guidelines on how to select an adequate laser machining strategy to achieve the desired microstructure, nor how geometrical changes might be adjusted to gain or control the (fluidic) effects. Figure 2.6 illustrates this lack of knowledge. That is, starting from a desired surface functionality (utmost right in figure 2.6), it is not known how to choose the required micro-machining strategy. Or for that matter, how to choose the required process parameters (utmost left in figure 2.6). The question marks indicate this lack of knowledge.

However, when tracing figure 2.6 from left to right, the calculation of a surface profile created by a microstructuring process with laser pulses would allow for the design and optimization of surface microstructures with respect to the desired functionality. A model of the micromichining process can then be employed to reveal the mechanisms causing a given fluid-microstructured substrate interaction. The present work is therefore aimed at developing a method for predicting the geometry of the microstructures emerging from an ablation process, that can be employed to study the influence of a changing geometry on the gained functionality.

2.6. Conclusions

The ablation of material by short and ultra-short laser pulses has been extensively studied over the last decades. In addition, the main mechanisms and physical phenomena responsible for the material removal process have been identified. However, an accurate prediction of the ablated profile $h(x, y)$ created by laser pulses in this regime has been shown to be cumbersome, particularly at low absorbed laser intensities.

Laser ablation with relatively long laser pulses, in the nanosecond regime, where the material removal process occurs at conditions close to thermodynamic equilibrium, is a relatively well-known process that allows for the calculation and prediction of ablated profiles. However, the existence of relatively thick molten layers during the excitation stage, and the consequent hydrodynamics, introduces uncertainties in the calculated ablated profiles. Moreover, the accuracy in the creation of microstructures, and the process repeatability in this regime is limited.

Processing with shorter laser pulses in the picosecond & femtosecond regime results in a higher microstructuring accuracy, due to the typical low ablated depths per pulse, and a more reproducible process, as a result of the limited presence of molten layers and residue. These two characteristics can be exploited not only to create functional microstructures, but also allow to analyze their (fluidic) properties by properly adjusting and varying the geometry of these microstructures. Therefore a model is desired capable of predicting the surface topography after a multi-pulsed laser exposure. A systematic study on how a surface profile emerges from a multi-pulsed exposure is still missing in the literature. Such an (empirical) model will be developed in the next chapter.

3 Surface microstructuring with short & ultra-short laser pulses

In this chapter a method is introduced for the calculation of the surface profile created on a solid target by laser ablation with short and ultra-short laser pulses. To that end, the calculation of energy diffusion lengths, and laser ablation of solid targets, are discussed first. An empirical method capable of determining surface profiles, based on the calculation of average ablated profiles per pulse, is presented next.

3.1. Simulation of a micro-machining process

The simulation of a microstructuring process first requires a calculation of the ablated profile, $h(x, y)$ [m] or "crater", induced by a single laser pulse. The accuracy of this calculation has a significant effect on the accuracy of the model, because of the large number of pulses that are required to create a full surface micro–structure. Relatively small inaccuracies in the estimated profile $h(x, y)$ accumulate, which may result into large deviations in the calculated surface profile $H(x, y)$.

A model capable of predicting the microstructures emerging from this process, requires several steps, and involves considering a variety of physical phenomena. The main steps of such a model are addressed in this chapter; and include (see also figure 2.6 on page 23):

1. the calculation of an average ablated profile, $h(x, y)$, or ablated profile, by a single laser pulse,
2. the design of a micro-machining strategy, consisting of a trajectory for the laser spot, scanning the surface of the sample,

3. the calculation of the resulting surface profile, $H(x, y)$ after numerous pulses along the trajectory and

4. the evaluation of geometrical properties and requirements, with respect to the (fluidic) application.

Each step involves assumptions, which are discussed below, and will be validated experimentally in chapter 4. The design of a micro-machining strategy (step 2) requires the definition of an *ideal* surface profile, $S(x, y)$, which provides a substrate with a (fluidic) functionality. The geometry of this targeted profile depends on the application.

Chapters 6 and 7 provide examples demonstrating the applicability of this model for the design of functional surface profiles. Further, the model is employed for the design of microstructures to study the fundamental mechanisms of certain fluid-microstructure interactions.

In the remainder of this chapter, a model for the calculation of functional surface profiles is developed. The calculation of average ablated profiles, based on a one dimensional approach, is first investigated. Calculated ablated profiles are thereafter employed for the simulation of a multi-pulsed process, in which partially overlapping pulses remove material from a substrate.

3.2. Calculation of the average ablated profile

As discussed in chapter 2, different numerical and experimental approaches provide relations between the temporal and spatial intensity profile of a laser pulse, $I(x, y, t)$, and the resulting ablated profile, $h(x, y)$. However, the accuracy of these relations is limited to certain processing conditions, and experimental and calculated data deviate. These inaccuracies can be attributed to uncertainties in material's properties, and the mathematical complexity of including all the relevant physical phenomena. An alternative approach is therefore required for the estimation/calculation of an ablated profile, $h(x, y)$, with an accuracy that allows for the subsequent calculation of a surface profile, $H(x, y)$.

The laser processing conditions leading to ablated depths close to the optical penetration depth, have been shown to result in surface microstructures with reproducible and well defined geometries [9, 10, 19]. To illustrate this, the processing conditions leading to limited diffusion depths of energy into the material are compared to the resulting ablated depths, in the following. This comparison establishes the basis for the development of a semi-empirical and an empirical approach for the calculation of $h(x, y)$, which are respectively discussed in sections 3.2.2 and 3.3.

3.2.1. Calculation of energy diffusion depths

The absorption of the optical energy of a laser pulse occurs near the surface of a substrate, with typical penetration depths ranging from 10 to 100 nm for metals [14, 36]. The typical diameter of a focused beam on the surface of the material, employed for micro-machining is of several μm up-to about 100 μm [9,10,38]. As a result, the effects of gradients in the material in radial direction can be neglected when compared to gradients in the vertical direction into the bulk of the material [12, 36]. Hence, a one dimensional Two Temperature Model can then be employed for the calculation of the temperature rise of the lattice of the material, see also section 2.4, starting on page 16.

In the TTM, the temperature increase of the lattice depends on the rate of energy transfer from the electron subsystem to the lattice. Two coupled differential equations describe the spatial and temporal temperature distribution of the electronic and lattice subsystems, denoted respectively as T_e and T_i. The velocity of the ablated front into the material, v[m/s], can be taken into account in these differential equations as [12]

$$c_e \frac{\partial T_e}{\partial t} = c_e v \frac{\partial T_e}{\partial z} + \frac{\partial}{\partial z}\left(\kappa_e \frac{\partial T_e}{\partial z}\right) + \frac{\partial I}{\partial z} - \mu (T_e - T_i), \tag{3.1}$$

$$c_i \frac{\partial T_i}{\partial t} = c_i v \frac{\partial T_i}{\partial z} + \frac{\partial}{\partial z}\left(\kappa_i \frac{\partial T_i}{\partial z}\right) + \mu (T_e - T_i), \tag{3.2}$$

where c_e and c_i are the heat capacities of the electron and lattice subsystems respectively, κ_e and κ_i are the thermal conductivities of the electron and lattice subsystems respectively, $v(t)$ is the velocity of the ablation front into the material, I is the absorbed laser intensity, and μ is a parameter characterizing the electron–phonon rate of energy exchange, $\mu = c_e/\tau$. The parameter μ is commonly known as the electron–phonon coupling coefficient. Further, τ is a characteristic relaxation time, which ranges typically from 0.5 to 100 ps [10]. The laser energy is absorbed first by the electron subsystem, as is described by equation(3.1).

When the duration of the laser pulse is significantly longer than the characteristic relaxation time, τ, the electronic system dissipates its energy already during the pulse to the lattice. In that case, there is no significant temperature difference between the electron and lattice subsystems [10]. The coefficient μ tends then to infinity and the temperature of the system is well described by the classical heat diffusion equation

$$c_i \frac{\partial T_i}{\partial t} = c_i v \frac{\partial T_i}{\partial z} + \frac{\partial}{\partial z}\left(\kappa \frac{\partial T_i}{\partial z}\right) - \frac{\partial I}{\partial z}. \tag{3.3}$$

Two different responses can then be expected for a given material exposed to laser pulses: A short pulse regime, in which the penetration length of energy into the material is dominated by the diffusion of hot electrons into the material, and a long pulse regime, in which the diffusion length of hot electrons can be neglected, and the energy penetration depth is governed by the classical thermal diffusion length. The respective calculation of these lengths, and a criteria for determining a *critical* pulse duration, separating both regimes, has been the subject of previous research [14, 16, 62] and is briefly summarized below.

Calculation of characteristic diffusion lengths

A characteristic diffusion length can be expressed in terms of the classic thermal diffusion length or, for a short pulse, in terms of the thermal diffusion length of hot electrons [14, 16, 62]. These lengths can be employed as an estimate of the spatial resolution that can be achieved when processing with (ultra) short laser pulses. This analysis has been proposed by Wellershoff et al. as an explanation of the sub-micrometric accuracy that can be obtained when processing with laser pulses in the femto– and picosecond regimes [16].

For the classical thermal approach, when electrons are responsible for the thermal conduction (e.g. metals), the diffusion term for the lattice in equation (3.3), that is, $\frac{\partial}{\partial z}\left(\kappa_i \frac{\partial T_i}{\partial z}\right)$, can be neglected. Then equation (3.3) can be solved for different cases. As an example, for the common case of a pulse with a Gaussian spatial intensity profile, equation (3.3) has been numerically solved to yield the thermal diffusion length, $l_{th,Tmax}$, at the time when the surface reaches its maximum temperature [14, 16]. This length equals

$$l_{th,Tmax} = 2\sqrt{D\tau_p}, \tag{3.4}$$

where τ_p is the Full Width at Half Maximum (FWHM) pulse duration and D ($\mathrm{m^2/s}$), is the thermal diffusivity of the material. As an example, table 3.1 lists the numeric value of $l_{th,Tmax}$ for various metals, for a pulse duration of 6 ps and 6 ns, respectively. As can be concluded from this table, the thermal diffusion length due to a ns pulse is (much) larger that that of a ps pulse.

For short pulses, typically below 1 ns for metals [16], the diffusion length of thermalized electrons, l_{e-ph}, can be employed for estimating the penetration length of energy into the material [62]. An estimate for the length of energy diffusion into the bulk can be obtained by considering the diffusion of thermalized electrons into the bulk, before thermal equilibrium with the lattice is reached. The later is governed by the electron–coupling strength. Wellershoff et al. [16] arrive to the following expression for this energy diffusion length,

Table 3.1.: Typical length and times scales in laser–material interaction for various metals. Values for h from Spiro et al. [46], for Gaussian pulses of 6 ps and 6 ns FWHM, at 2 times the respective ablation threshold of the material. The critical pulse duration, τ_{cr}, was calculated according to equation (3.6) [16]. The physical properties of the selected materials are summarized in appendix 8.2.

Material	α^{-1},	$l_{th-Tmax}$,(nm)		l_{e-ph},	h,(nm/pulse)		τ_{cr},
	(nm)	6 ps	6 ns	(nm)	6 ps	6 ns	(ps)
Al	7	35	1435	68	27–85	100–390	12
Ni	13	17	693	31	19–46	84–580	11
Mo	11	32	1020	66	4–22	20-260	23
SS302	11(Fe)	7	219	**	5–25	20–242	**

**Data are not available.

l_{e-ph}

$$l_{e-ph} = \left(\frac{128}{\pi}\right)^{1/8} \left(\frac{\kappa_{e,o}^2 c_i}{A_e T_m \mu^2}\right)^{1/4} , \tag{3.5}$$

where A_e and κ_{e0} are constants describing the specific heat c_e and conductivity κ_e of the electrons, via $c_e = A_e T_e$ and $\kappa_e = \kappa_{e0}\, T_e/T_i$, respectively [16]. T_m is the melting temperature of the lattice.

The fifth column of table 3.1 lists numeric values of l_{e-ph}. As can be observed, the penetration of energy into the material by electronic diffusion is about twice the thermal diffusion length, for a pulse duration of 6 ps. The maximum penetration length of energy is therefore given by the thermal diffusion length l_{th}, for a pulse duration of 6 ns, and by the diffusion length of energy by thermalized electrons l_{e-ph}, for a pulse duration of 6 ps.

Now, the diffusion length of the electrons during the time required for the establishment of thermal equilibrium between electrons and phonons can be compared to the thermal diffusion length [16, 62], to find a pulse duration from which the electronic diffusion dictates the maximum diffusion depth of energy into the material. This critical pulse duration, τ_{cr}, is then defined by the condition $l_{th} = l_{e-ph}$. This condition gives the pulse duration for which the diffusion length of electrons equals the thermal penetration depth [16]. Equating equations (3.4) and (3.5) yields

$$\tau_{cr} = \left(\frac{1}{2\pi}\right)^{1/4} \left(\frac{c_i^3}{A_e T_m \mu^2}\right)^{1/2} . \tag{3.6}$$

The last column of table 3.1 lists values of τ_{cr} for different materials. In materials with a strong electron–phonon coupling, the absorbed energy is confined near the surface, due to the reduced time that is required for the thermalization of the lattice [10, 16, 35]. As a result, the temperature rise of the lattice occurs in a shorter time and in a reduced volume, when compared to materials with a weak electron-phonon coupling. Therefore, the energy transfer of residual energy to the bulk is potentially reduced. In these cases, ablated profiles with a typical maximum depth in the order of a few tens of nanometer per pulse can be achieved. This allows for a high accuracy in the material removal process, while diminishing undesired effects on the surrounding material due to residual energy.

The critical pulse duration can be employed as an estimate to select the pulse duration of the laser source to achieve small diffusion lengths. In principle, selecting a laser source with a laser pulse duration as short as possible leads to a better machining quality, due to the reduced diffusion lengths. However, non-linear effects, such as optical breakdown, become of increasing relevance at reduced pulse duration, due to the high intensity [10]. Then, the laser intensity profile becomes significantly disturbed, and the machining results are less reproducible [10]. Therefore, for a given material, the selection of a laser system for microstructuring involves considering the following steps:

- selection of a pulse duration which is short enough, to decrease the energy penetration depth. The critical pulse duration of equation (3.6) can be employed as a guideline.
- selection of the laser beam quality, or M^2, wavelength and power density profile, $I(x, y, t)$. These parameters affects the effective focal spot size, which in turn determines the minimum feature size that can be achieved.

The limited penetration depths of energy in the material for a short pulse, when compared to the typical lateral dimensions of a laser spot, justify a one dimensional analysis of the ablation process, which is developed in the following.

3.2.2. A simplified analytical model

The analysis in the previous section can be employed to obtain a simplified analytical expression for the ablated profile $h(x, y)$, considering one dimensional diffusion of energy in the vertical direction. Then the ablation depth at a given location along the z axis can be calculated as the deepest point that is exposed to an intensity that is *high enough* for material removal. A simplified analytical expression for the ablated profile can be obtained by considering the attenuation of optical intensity of the laser light within a semi-transparent material. The intensity decay within the absorbing material is given by

$$\frac{\delta I}{\delta z} = -\left(\alpha + \beta I\right) I, \tag{3.7}$$

where I is the absorbed intensity, α (m^{-1}) and β (m/W) are the linear and two–photon absorption coefficients, respectively. For materials whose primary absorption mechanism leads to a linear response to the laser energy, i.e., linear absorption, equation (3.7) simplifies to the well-known Beer-Lambert law

$$\frac{\delta I}{\delta z} = -\alpha I, \tag{3.8}$$

Under the assumption of one-dimensional diffusion of energy, equations (3.7) and (3.8) can be integrated along the z axis, to relate the ablated depth h, to the absorbed local intensity I, as

$$\int_{I_0}^{I_{th}} \frac{\delta I}{I} = -\alpha \int_0^h \delta z, \tag{3.9}$$

where I_{th} is the minimum intensity at a depth h, that suffices to trigger ablation of the substrate. With this approach, an intensity *threshold* for ablation, I_{th}, is introduced. The integrated equation yields the depth h at a point exposed to an incident intensity I_0, which reads

$$h = \frac{1}{\alpha} \ln\left(\frac{I_0}{I_{th}}\right). \tag{3.10}$$

In the case of a temporal rectangular shaped pulse of τ_p seconds, the absorbed intensity I is related to laser incident fluence ϕ_0 as

$$\phi_0 = I_0 \tau_p = \frac{I \tau_p}{(1 - R)}, \tag{3.11}$$

where R is the reflectivity of the material at the wavelength under consideration. Then, it follows from equations (3.10) and (3.11) that

$$h = \frac{1}{\alpha} \ln\left(\frac{\phi_0}{\phi_{th}}\right). \tag{3.12}$$

The analysis can be extended to include the spatial intensity profile of the pulse, which is justified by the 1D analysis. For a spatial Gaussian distribution, the incident fluence $\phi(r)$ reads

$$\phi(r) = \phi_0 \exp\frac{-2r^2}{w_0^2}, \tag{3.13}$$

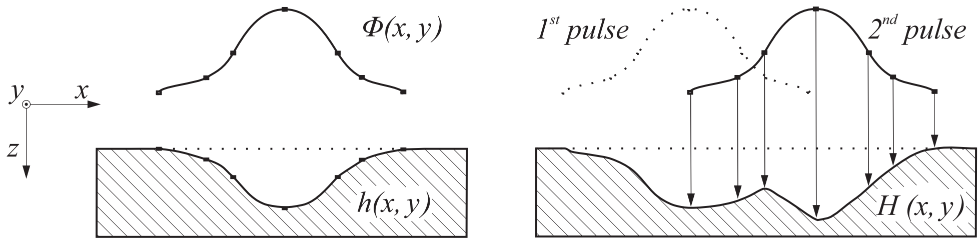

Figure 3.1.: Left: a calibration curve, $h(x, y)$, is obtained by measuring the surface profile created by a laser pulse of intensity $\phi(x, y)$. Right: the calibration curve is successively employed to calculate the surface profile created by processing with from partially overlapped laser pulses.

where r is the radial coordinate, and w_0 is the radius of the laser beam at the surface. Then, by using equation (3.11), the ablated depth $h(r)$, at a location r, reads

$$h(r) = \frac{1}{\alpha} \ln \frac{\phi(r)}{\phi_{th}}. \tag{3.14}$$

The logarithmic dependence of the ablated depth and fluence has been experimentally observed for a broad range of processing conditions and materials, when processing with short and ultra-short laser pulses [14, 15, 19, 20]. Both the optical penetration depth, α^{-1}, and the ablation threshold, ϕ_{th}, are usually treated as fit parameters. The fitted values for α are not consistent with the corresponding tabulated values, even when averaged values are considered [63]. These discrepancies have been attributed to the surface condition, the absence of an inert atmosphere or to surface instabilities [63].

Relatively small deviations between experimental data and the values predicted by the fitted equation (3.14) are however present, particularly at low fluence levels. This leads to large prediction errors because the errors are accumulating during the simulation of a multi-pulsed process.

3.3. Modelling a laser micromachining process

As concluded in the previous paragraph, the simplified analytical expression for the ablated profile, $h(r)$, as a function of the laser fluence, equation (3.14) does not provide the accuracy that is required for the simulation of an ablated surface profile $H(x, y)$. Further, the numerical calculation of $h(r)$ from the laser pulse intensity profile $I(x, y, t)$ and material properties has been shown in chapter 2 to be cumbersome, due to the uncertainties in the mechanisms responsible for the material removal process.

An experimental approach can be considered to circumvent the difficulties in the calculation of an ablated profile $h(x, y)$. A typical micro–structuring process employs a focused laser beam with lateral dimensions typically ranging between 10-100 micrometers [10, 20, 38], while the typical ablated depths have been shown to be at least two orders of magnitude below these values [46]. As discussed in section 3.2.1, the one-dimensional assumption for the diffusion of energy may then be extended to the ablation process. Following this reasoning, the measured depth at a location can be related to the total local incident fluence, $\phi(x, y)$, arriving at (x, y). A calibration curve can then be directly constructed by measuring the ablated depths at points exposed to different incident (local) fluences, which yields the desired curve $h(x, y)$.

A laser source generates pulses with a given spatial intensity profile, typically of Gaussian shape in the focal plane. The exposed area is therefore usually irradiated with varying fluence levels within a single pulse. The ablated profile produced by a laser pulse with a given fluence profile can then be employed directly as a *calibration curve*, $h(x, y)$, see figure 3.1 (left). With this approach, the actual fluence profile on the surface of the substrate does not have to be measured nor calculated. This is of practical interest as deviations from the ideal shape do occur, like beam ellipticity or those typically produced by aberrations, e.g., due to imperfect optics. These effects are difficult to implement with alternative approaches, but do modify the ablated profile significantly.

Due to the small ablated depths per pulse, a direct measurement of $h(x, y)$ is hard to obtain. As a consequence, a minimum number of laser pulses have to be applied to resolve the ablated profile. The ablated profile $h_N(x, y)$, generated after N pulses, can be measured by different microscopy techniques in order to obtain an averaged, single-pulse, ablated profile, $h_{av}(x, y)$. The average ablated profile per pulse, $h_{av}(x, y)$, is obtained by normalizing the measured ablated profile by the number of applied pulses N, to yield

$$h_{av}(x, y) = h_N(x, y)/N, \tag{3.15}$$

This procedure is based on several implicit assumptions. The selected substrate is considered to be homogeneous, and the processing conditions, i.e. the spatial and temporal laser intensity profile, are assumed to remain constant during processing. In addition, the ablated depth is assumed to show a linear increase with the applied number of pulses N.

Some considerations have to be taken into account when assuming a constant ablated depth for each (subsequent) pulse during a multi-pulsed exposure. Deviations from the linear response, related to changes in the response of the material to the laser radiation and/or due to the changing geometry, have to be considered. The applicability and range of this linear process is further investigated and discussed in chapter 4.

The average profile $h_{av}(x, y)$ is subsequently employed for the calculation

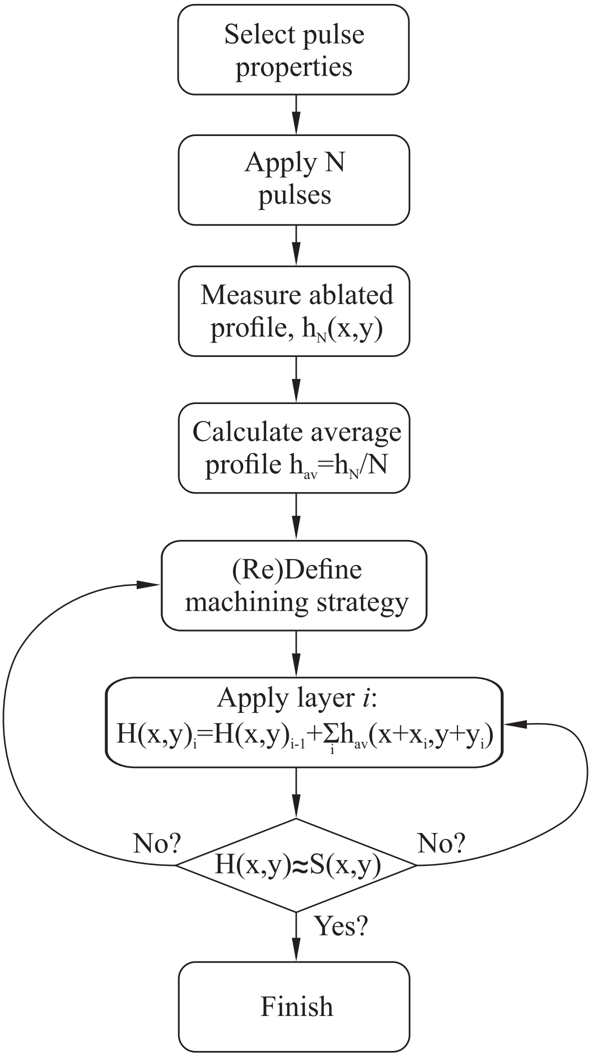

Figure 3.2.: Flow chart for the modelling approach. The ablated profile generated after applying N pulses, $h_N(x, y)$, is measured, in order to obtain an average ablated profile, $h_{av}(x, y)$. The average profile is afterwards employed for the calculation of a surface profile $H(x, y)$, according to a predefined machining strategy. The simulation is concluded when the ideal surface $S(x, y)$, which provides the functionality, is obtained.

of a surface profile $H(x, y)$. The one-dimensional approach, and the assumed linearity of the multi-pulsed process, allow for a direct simulation of the surface profile obtained after a displaced second (and subsequent) laser pulse(s) remove material from the substrate, see figure 3.1(right), which results in $H(x, y)$. The simulation of a micromachining process consists then of dis-

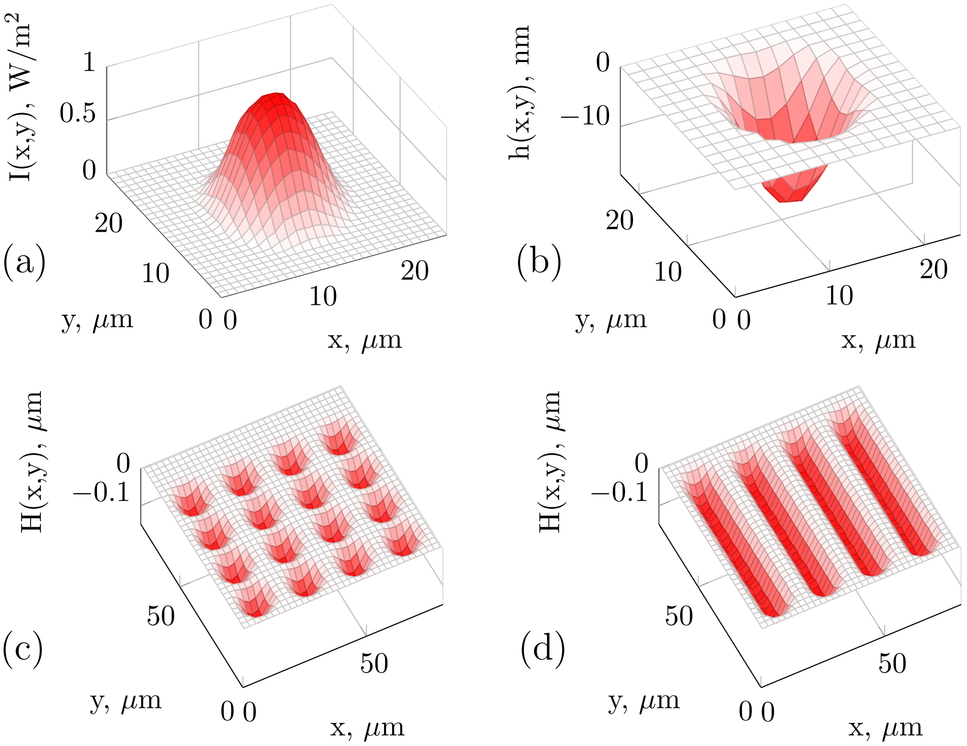

Figure 3.3.: Modelling a microstructuring process with short laser pulses of spatial intensity $I(x, y)$, (a), based on the measurement of the average ablated profile $h_{av}(x, y)$, (b), created by the laser pulse. The ablated profile is scanned following laser tracks at low, (c), or high pulse to pulse overlap, (d).

tributing the laser pulses across an area, according to the machining strategy, which defines the position (x_i, y_i) of a laser pulse within a *layer i*. In general, several layers are required to obtain the desired surface profile. The simulation is concluded when the ideal surface $S(x, y)$ providing a functionality is reached. The flow chart in figure 3.2 illustrates the main steps of this experimental approach.

3.4. Simulation of a micro–machining process

The surface profile $H(x, y)$ created by the microstructuring process can be directly calculated once the average ablated profile $h_{av}(x, y)$ is known. That is, the surface profile follows from

$$H(x, y) = \sum_{i=1}^{N} h_{av}(x + x_i, y + y_i), \tag{3.16}$$

where N is the number of applied pulses located at positions (x_i, y_i), according to the *machining strategy.* Here, the term *machining strategy* refers to the spatial locations of the applied pulses on the surface.

The laser pulses are usually arranged into *laser tracks*, which consist of straight lines scanned across the substrate at a given scan velocity v of the laser beam relative to the substrate. The scanning velocity and the laser repetition rate f both determine the spatial separation between consecutive laser pulses. In most cases, the laser pulses spatially overlap. The *pulse overlap*, OL, is then a design parameter and is defined here as

$$OL = 1 - \frac{v_B}{f \cdot d}, \tag{3.17}$$

where v_B is the beam velocity, f is the repetition rate of the laser, and d is the beam diameter at the surface of the substrate. The laser tracks have to be arranged according to a suitable pattern, to create a desired microstructure $S(x, y)$. In the case the required depth of $S(x, y)$ can not be achieved by a single pass of the laser spot in the trajectory (given by the machined strategy), several “layers” along the z axis are required. Hence, the positioning and relative orientation of consecutive layers is an additional design parameter.

The simulated area consists of a rectangular regular grid which initial height is set to zero. The first pulse will generate a surface profile according to the calibration curve, $h(x, y)$ which is illustrated in figure 3.3(b). The surface profile $H(x, y)$ is then updated, correcting the depth at each location of the grid according to its relative location with respect to the previous pulse. This is given by $H(x, y)_i = H(x, y)_{i-1} + h(x_i + dx, y_i + dy)$, where dx and dy are respectively the lateral displacements of the laser spot in the (x, y) plane, given by the selected machining strategy.

Figure 3.3 summarizes the modelling approach. A laser pulse with a given spatial intensity profile, figure 3.3(a), generates an ablated profile $h(x, y)$, figure 3.3(b), which is employed for the simulation of two surface profiles, figures 3.3(c) and (d). That is, these surface profiles are created from parallel laser tracks, which are machined respectively with a low, figure 3.3(c), and a high, figure 3.3(d), pulse overlap.

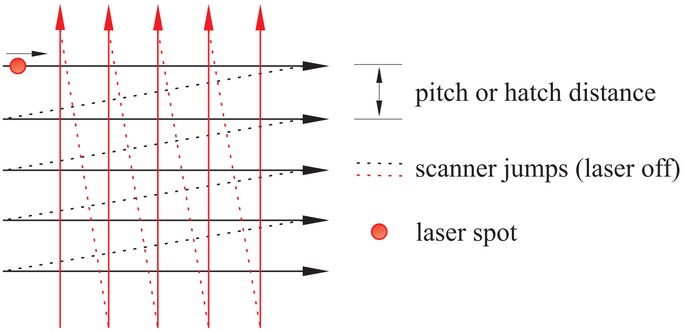

Figure 3.4.: Example of a machining strategy. The trajectory of the laser spot is arranged into two sets of straight and parallel tracks, which are scanned orthogonally. This machining strategy is referred here to as a *hatched pattern.*

3.5. Evaluation of geometrical requirements

In general, achieving a functional microstructure requires the creation of surface features with an adequate geometry. The fulfillment of the geometrical requirements may consist of achieving, for example, microstructures with a certain shape, depth, aspect ratio or slope.

In the remainder of this thesis, a given *machining strategy*, consisting of a regular hatched pattern, is selected as an example. The hatched pattern consists of two sets of straight and parallel laser tracks, which are scanned orthogonally, at a constant speed and repetition rate, see figure 3.4. As a result of the material removal process, pillar–like features will result from the process, see figure 3.5(b). In chapter 6, this pillar–like structure is shown to provide a substrate with water repellent properties. In order to achieve this functionality, the pillars should reach a minimum slope at the sides of the pillars, and the separation between the peaks of the microstructure should not exceed a certain value. These geometrical requirements are further described in chapter 6. For the remainder of this chapter, as well as chapter 4, is suffices to summarize the main geometrical parameters of the hatched pattern as:

- the distance between parallel lines, referred to as the hatch distance (h_d)
- the pulse overlap, (OL)
- the number of laser cycles $(\mathrm{N_L})$, that is, the number of times a machining strategy is repeated

Figure 3.5(c) shows the cross section of a surface profile created by applying the hatched pattern, for increasing number of laser cycles. The procedure to achieve the desired profile $S(x, y)$ runs iteratively, calculating the average

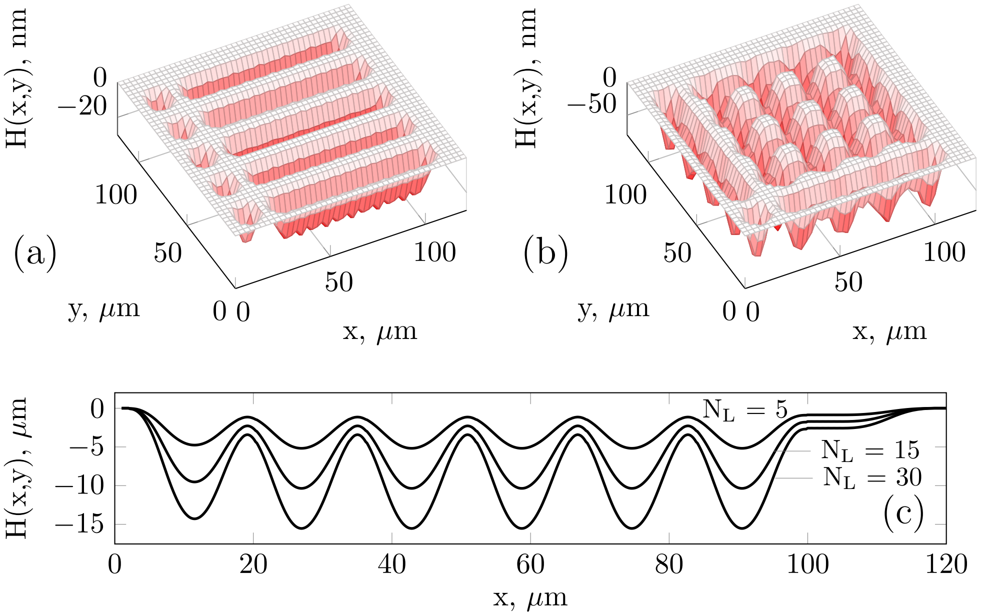

Figure 3.5.: Evolution of the cross–section of a simulated microstructure, $H(x, y)$, after increasing number of applied laser cycles, $\mathrm{N_L}$. The increased depth and/or slope of the surface features is calculated after each laser cycle. The simulation is stopped when the required geometry, $S(x, y)$, is achieved.

slope of the pillars after a laser cycle is finished, and stopping when the requirement regarding the slope is met. The separation between the laser tracks is also systematically varied. The model yields then as an output the required machining strategy, that is, the pulse overlap, distance between laser tracks h_d and number of laser cycles, that are required to fulfill the geometrical requirements.

3.6. Application range

The proposed model of the microstructuring process has so far been considered as the result of a repeated single-pulsed process, from which a surface profile $H(x, y)$ can be calculated from the accumulated contribution of individual and independent pulses. However, a number of phenomena may become relevant during a multi–pulsed process, introducing inter-pulse interactions that may modify the ablation process and therefore limit the applicability of the model.

These effects are related to, among others, the changing geometry, the rate of residual energy diffusion into the bulk and to the accumulation of removed matter nearby the interaction zone. As a result, the linearity of the removal process is limited to certain processing conditions. These effects are further discussed below.

Pulse energy

As discussed in section 2.4, the local fluence level of a laser pulse determines the actual mechanism(s) responsible for material removal. The ablation rate, and the size and morphology of the profile depend strongly on this parameter. Increasing the fluence does increase the ablation rate, but the processing quality is greatly disturbed when the pulse energy exceeds a certain value. This can been attributed to a change in the ablation mechanism, as the *thermal regime* is approached with increasing pulse energy, as discussed in section 2.2. The modelling approach presented in the previous section is not applicable to this thermal regime.

Therefore, the selection of the pulse energy consists of experimentally identifying the range of pulse energies which limits the ablation to a depth close to the optical penetration depth (section 3.2.1). The ablation process in this regime leads in general to a more controllable process, where the maximal ablated depths, as well as the presence of molten layers and residue, are significantly reduced [10].

Heat accumulation

The ablation of material is considered to be completed before the next pulse arrives at the surface of the material. This assumption is applicable for moderate pulse frequencies and energies. That is, if the pulse frequency and/or the pulse energy increases, the time between pulses may not be sufficient for the diffusion of residual thermal energy out of the laser-material interaction zone. As a consequence, the temperature of the substrate will increase with each subsequent pulse.

Luther-Davies et al. [64] have investigated the influence of heat accumulation when processing materials with low thermal conductivity at high repetition rates. Repetition rates in the MHz regime were required to produce a noticeable change in the ablation process of glass, which is a thermal insulator. The effect of heat accumulation in a multi-pulsed process has to be analyzed for each particular case.

Particle confinement

In the case of deep microstructures, ablated material may not be ejected in time from the interaction zone, resulting in a partial shielding of the incoming laser pulses. Material may also re-condense on the surface of the material and in the created micro-structure. As a result, the amount of energy available for material removal, and the efficiency of the process, decreases. If the intensity of the pulse suffices, the ejected material may also be ignited, providing an additional mechanism for material removal. The ignition of ejecta, or optical breakdown, simultaneously increases the reflectivity. The combined effect of these phenomena results into a non-linear relation between the applied number of pulses N and the depth at that location $h(x, y)$. The microstructures which are the subject of study in this work gain their functionality when relatively shallow structures are created, so these effects are presumed to have a negligible effect.

Multiple reflections and surface roughness

It is known that the absorption of optical energy is further enhanced due to multiple reflections within the created microstructures. Percussion drilling experiments with linear polarized laser light have revealed the existence of two different ablation regimes, as a function of the hole depth [65, 66]. The material removal process proceeds at a constant rate per pulse, up to a certain number of applied pulses [66]. After a certain number of pulses, new mechanisms modify, and eventually dominate, the material removal process. As a consequence, the linearity is lost. These have been related to different coupling mechanisms between reflected polarized rays [65].

Material removal by laser ablation creates rough surfaces, which may result into an increased absorption for successive pulses, due to multiple local reflections. The creation of rough surfaces has been suggested as an explanation for an increased absorption of laser light [67,68]. This effect would then result in an extended linear range, as an increased (local) absorption reduces the relative contribution of the coupling effects introduced above.

3.7. Conclusions

A method, capable of predicting the surface profile emerging after a microstructuring process with short laser pulses has been developed. The applicability of the model for the prediction and design of microstructures with a functionality, depends on the range of sizes and depths that can be predicted. As a structure becomes deeper, several effects alter the ablation mechanisms. These can be related to geometrical changes and particle confinement. The relative contribution of such effects strongly depends on the system in consideration, that is, the laser source, the material to be processed and the particular microstructure. Hence, the applicability range for this approach needs to be assessed for each specific case. Therefore, the main assumptions of the model, and its applicability are experimentally verified and discussed in chapter 4.

4 Empirical model & validation

In this chapter, the model developed in the previous chapter is experimentally verified. More specifically, the range of application (or process-window) of the model is experimentally determined. To that end, average ablated profiles are measured and used for the simulation of a laser microstructuring process. Different processing conditions are selected and systematically varied, to assess the accuracy of the model by a direct comparison between predicted and measured surface profiles.

4.1. Introduction

In the previous chapter, a model was developed which predicts the surface profile emerging from a laser micromachining process, on the basis of a predefined machining strategy. It was stated that the validity of this model is limited to the laser processing conditions within the so-called optical regime.

This chapter is aimed at establishing the range of processing conditions, or process window, for which a multi–pulsed ablation process remains within a linear regime, in terms of ablated depth per pulse. The application range of the model will be defined in terms of the maximum energy per pulse, and maximum number of pulses. Next, several surface profiles calculated by the model, will be directly compared to experimental data, to assess the applicability and accuracy of the model for the creation of functional surfaces.

4.2. Experimental setup, material and methods

Laser setup

A Yb:YAG picosecond pulsed laser source was employed, operating at a central wavelength of 1030 nm, and delivering pulses with a duration of about 7 ps, with a nearly Gaussian beam spatial profile ($M^2 < 1.3$). The laser radiation

Table 4.1.: Properties of the picosecond laser source.

Property	Central wavelength 1030 nm	Second harmonic 515 nm	Third harmonic 343 nm
Average power	50 W	25 W	15 W
Max. pulse energy	125 μJ	62.5 μJ	37.5 μJ
Repetition rate		1 – 400 kHz	
Pulse duration		$<$ 7ps	
Beam quality M^2		$<$ 1.3	
Polarization		Linear	
Intensity profile		Gaussian	

was linearly polarized. Second, as well as third, harmonic generation units, referred to as respectively SHG and THG, were available for converting the central wavelength to, respectively, 515 nm and 343 nm. This laser source is capable of delivering a maximum average laser power of 50 W at its maximum repetition rate of 400 kHz. The corresponding maximum pulse energies are 125 μJ in infrared, 63 μJ in green and 38 μJ in ultraviolet. Table 4.1 summarizes the main properties of the laser source.

Manipulation of the laser beam over the samples was accomplished by a two-mirror Galvo-scanner system. A telecentric f-θ lens with a focal length of 103 mm was employed for beam focusing. This optical setup has an estimated absolute positioning accuracy of 1 μm. The beam diameter at the focus was measured using the well-known D^2 method [69]. The diameters were found to equal 30 and 16 μm at the laser central wavelength (1030 nm), and at its second harmonic (515 nm) respectively. The resulting beam diameter at the focus, and the depth of focus of the selected lens, of about 400 μm at 515 nm, allowed obtaining surface features with a similar geometry across areas of typically 40x40 mm^2, which are large enough for testing their fluidic functionality. A combination of a $\lambda/2$ and a polarizing beam splitting cube were employed for beam attenuation. The materials were machined under environmental conditions at constant temperature with control of the relative humidity. Figure 4.1 shows a schematic view of the employed experimental setup.

Material

A stainless steel X5CrNi18-10 grade (EN 1.4301), was selected for the experimental validation of the model. Stainless steel has a relatively low thermal diffusivity (0.04 cm$^2/s$), and it is mainly composed of transition metals, see table 4.2. Transition metals have a strong electron–phonon coupling, thus re-

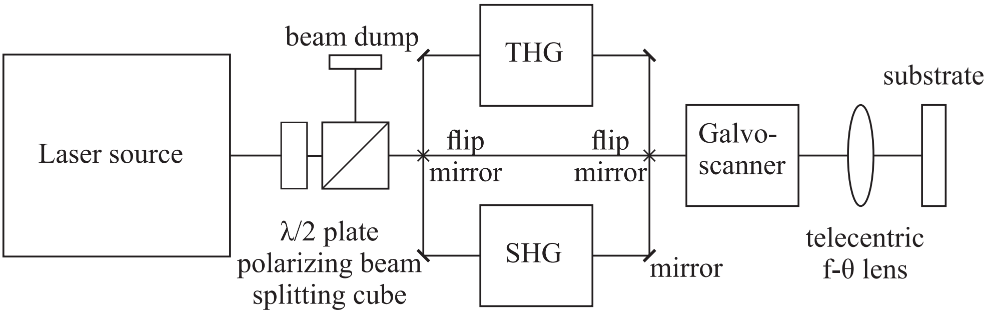

Figure 4.1.: Laser setup.

quire a relatively short time for the thermalization of their lattices. The thermalization time for iron is remarkably short, of around 0.5 picoseconds [70]. As a result, this substrate effectively confines the absorbed energy close to the surface and the laser-material interaction zone, which suits well the hypothesis of the model regarding the limited energy transfer to the material surrounding the laser-material interaction zone. The samples were mechanically polished to a roughness R_{RMS} below 50 nm, which is a roughness level comparable to the typical feature size obtained after laser ablation with single pulses.

Methods

The orthogonal hatched pattern introduced in chapter 3, see figures 3.4 and 1.3(b), was selected for the creation of test surface profiles and, via a direct comparison between measured and calculated surface profiles, for validation of the model. The surface profile emerging from this pattern shows changes in both slopes and depths. Further, in this pattern some areas are exposed to a doubled energy input, at the crossing of the laser tracks, while some areas have less exposure to the laser radiation, i.e. at the lateral edges of the laser tracks. This machining strategy therefore allows to study the process window of the model.

The laser created surface profiles were analyzed by means of confocal laser scanning microscopy (CLSM). The acquired data contained depth information at each location on the xy plane. The resolution in the *xy* plane of this instrument is 45 nm, at the maximum magnification of the microscope. This allowed for a sufficient lateral resolution, considering the micrometric-sized

Table 4.2.: Typical composition of stainless steel X5CrNi18-10, atomic %.

Material	C	Mn	P	S	Si	Cr	Ni	Fe
SS304	0.08	2.0	0.045	0.030	1.0	18.0-20.0	8.0-10.50	Balance

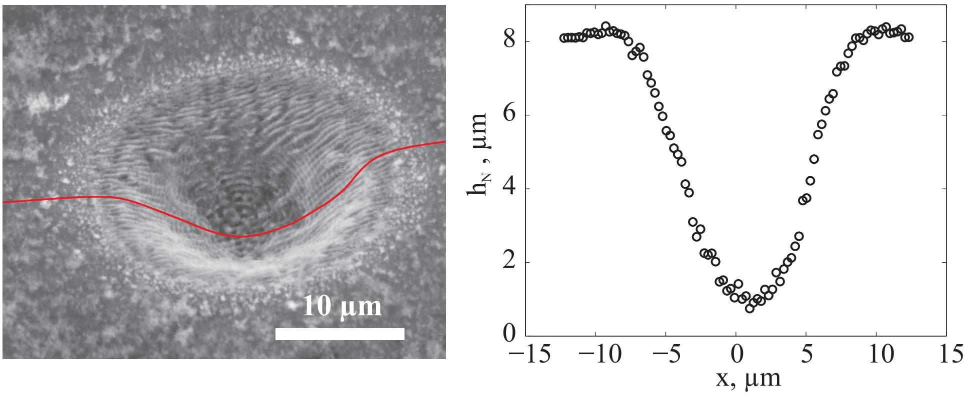

Figure 4.2.: SEM image (left) of a crater generated by 400 pulses at a peak incident fluence of 0.43 J/cm^2. The corresponding surface profile shown in this image (red curve) was acquired by CLSM. The SEM image reveals details that cannot be resolved by CLSM, like redeposited material around the perimeter of the crater or the so-called Laser Induced Periodic Surface Structures (LIPSS). The length of the scale bar in the SEM picture is 10 μm. The graph to the right shows the surface profile acquired by CLSM.

features created in this work. At locations in the xy plane exposed to a low intensity of the laser radiation, e.g. at the wings of the Gaussian intensity profile, the ablated depth is too small to be resolved by the CLSM. Therefore, a sufficient number of pulses were applied. The surface profiles created by the first tens of pulses were then excluded from the calculation of the average ablated profiles $h_{av}(x, y)$.

4.3. Process window & pulse energy range

As discussed in section 2.4, the pulse energy directly affects the ablated depths, the geometry of the resulting ablated profile and the reproducibility of the material removal process. In general, this parameter has the largest influence on both the quality of a created microstructure and the processing speed.

Further, as discussed in section 3.3, a linear relation between ablated depth, $h_N(x, y)$, and applied number of pulses, N, can be expected, for a limited range of pulse energies as well as for a limited number of pulses. In order to determine these ranges, several ablated profiles were created by laser pulses at increasing energy levels, on the same location of the surface. These profiles were measured by confocal microscopy, obtaining depth information at each exposed location.

Figure 4.2 shows an example of a SEM image of a crater generated by 400 pulses at a peak incident fluence of 0.43 J/cm^2. The corresponding surface profile is acquired by CLSM and it is shown in figure 4.2 (right). The SEM

Table 4.3.: Process window for the linear multi-pulse material removal process by short laser pulses. Processing conditions: <7 ps pulses at 515 nm. Substrate: polished stainless steel X5CrNi18-10.

Pulse energy, μJ	Peak fluence, J/cm^2	Max. number of pulses	Max. depth, μm
0.45	0.43	>500	>10
0.55	0.52	>500	>10
0.8	0.76	≈200	≈5
1.3	1.23	≈200	≈5
2.7	2.67	<200	<5

image reveals details that cannot be resolved by CLSM, like redeposited material around the perimeter of the crater or the so-called Laser Induced Periodic Surface Structures (LIPSS) [71, 72]. These features have typical lateral sizes below 1 μm, which are dimensions below the scope of the current analysis. The effect of submicrometric surface features on the fluidic functionality is further discussed in section 6.4.

Figure 4.3 shows measured ablated profiles created with an increasing number of pulses, ranging from 100 to 500, at four peak fluence levels. As can be observed from this figure both the ablated depth at any given location, and the diameter of the ablated profile, or ‘‘crater’’, increase with (peak) fluence as well as with number of applied pulses.

For each combination of peak fluence and number of pulses N=200, an average ablated profile $h_{av}(x, y)$, solid red curves in figure 4.3, was fitted following a procedure described in appendix I. This fit is just a visual aid to guide the eye, and it is not based on any physical relation. As mentioned above, the average profile, following tightly the experimental data points, was determined for the profile generated by 200 laser pulses. Next, to assess the linearity of the process, the curve was accordingly multiplied by the ratio of $N/200$, where N is the actual number of applied pulses, to obtain curves at N number of pulses (see dashed curves in figure 4.3). This gives a qualitative indication of the linear dependency of the ablated depth, $h(x, y)$ with the number of applied pulses, N. This linearity in the multi-pulsed ablation process is further assessed in section 4.4.

The ablated profile was measured down to a depth of about 10 μm, when processing at a peak fluence of 0.43 J/cm^2, figure 4.3(a). However, when the pulse energy was further increased, voids were formed at the bottom of the craters and hampered the CLSM measurements, for peak fluences of and above 0.76 J/cm^2, see figures 4.3(b) to (d). These effects were observed after a few tens of pulses. This limits the model to processing conditions which would

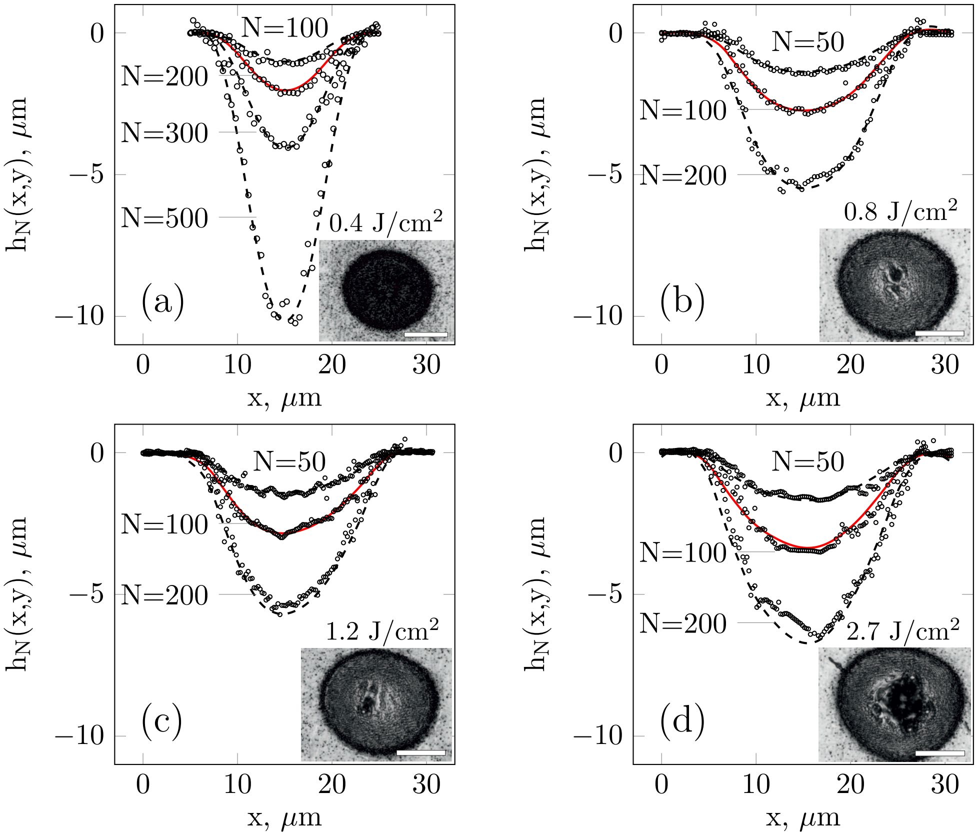

Figure 4.3.: Cross-section along the x-axis of a surface profile of a stainless steel X5CrNi18-10 polished substrate after exposure to increasing number of pulses at a fixed location, at a wavelength of 515 nm. Number of pulses 100, 200, 300 and 500, (a), and 50, 100 and 200, (b), (c) and (d). Applied peak fluence levels, (a) 0.4, (b) 0.8, (c) 1.2 and (d) 2.7 J/cm^2, respectively. The solid red lines represent average profiles, see text for details. The insets show confocal microscope images of the resulting craters after 500 pulses, (a), and after 300 pulses (b), (c) and (d). The size of the scale bar in the insets is 10 μm.

result in craters not deeper than about 5 μm. The insets in figure 4.3 show confocal intensity images of the ablated profiles after 500 pulses, figure 4.3(a), and after 200 pulses for figures 4.3(b), (c) and (d). The formation of voids and the observed increased reflectivity at the bottom of the ablated profiles can be attributed to the presence of increasingly thick molten layers, and to the nucleation of gas and/or liquid phases within these, as a result of the energy excess. The formation of voids indicates the transition from the optical to the thermal ablation regime, see section 2.2. It therefore can be employed as a criterion for selecting the upper limit of the pulse energy range.

The linearity of the relation ablated depth and applied number of pulses is in general lost at these higher fluence levels. The onset for these effects occurs for this material at about 200 pulses, at a peak incident fluence value of 0.76 J/cm^2. As the pulse energy is further increased, the non-linear effects become more prominent. That is, the ablated depths increase strongly, as the thermal regime is reached. Hence, the determination of the processing window regarding the pulse energy should be based on finding the limit for the transition into the thermal regime.

Applying laser pulses with a peak fluence in the range up to 0.76 J/cm^2 ensures a reproducible process, in terms of ablated depth per pulse, to a sufficient depth, see figure 4.3(a). The maximum number of pulses that can be applied, at this fluence level, is about 200, which corresponds to an ablated profile with a maximum depth of about 5 μm. When the peak fluence is decreased to 0.43 J/cm^2, the number of pulses that can be applied showing a linear relation between ablated depth and applied number of pulses increases to 500, corresponding to a maximum depth of the ablated profile of about 10 μm.

4.4. Calculation of ablated profiles

The material removal process at moderate pulse energies below 0.76 J/cm^2 was further studied in order to determine the average ablated profile, $h_{av}(x, y)$. This average profile will be employed for simulation of the micromachining process at a later stage. Based on the results from the previous section, two pulse energies below the transition from the optical into the thermal ablation regime, with peak fluences of 0.43 and 0.52 J/cm^2, were selected for further study.

Figures 4.4 (a) and (b) show the fitted ablated profiles obtained after laser processing with an increasing number of pulses, at the two fluence levels. The applied number of pulses is varied from 100 to 500, with increments of 50 pulses. The plotted smooth curves follow tightly the measured data, and were obtained after applying the curve-fitting procedure described in appendix I. The experimental data are not depicted here for clarity, but the relative deviation to the curves is similar to the data shown in figure 4.3(a).

The fitted smooth curves allow for a qualitative study of the depth increase of the ablated profiles as the number of applied pulses increases. Figures 4.4(c) and (d) show average ablated profiles, obtained by normalizing each fitted profile in (a) and (b) by the respective number of pulses, i.e. $h_{av}(x, y) = h_N(x, y)/N$. These normalized average profiles in figures 4.4(c) and (d) practically overlap, which indeed indicates a linear increase of the depth with the number of pulses, at each location, for a given pulse energy.

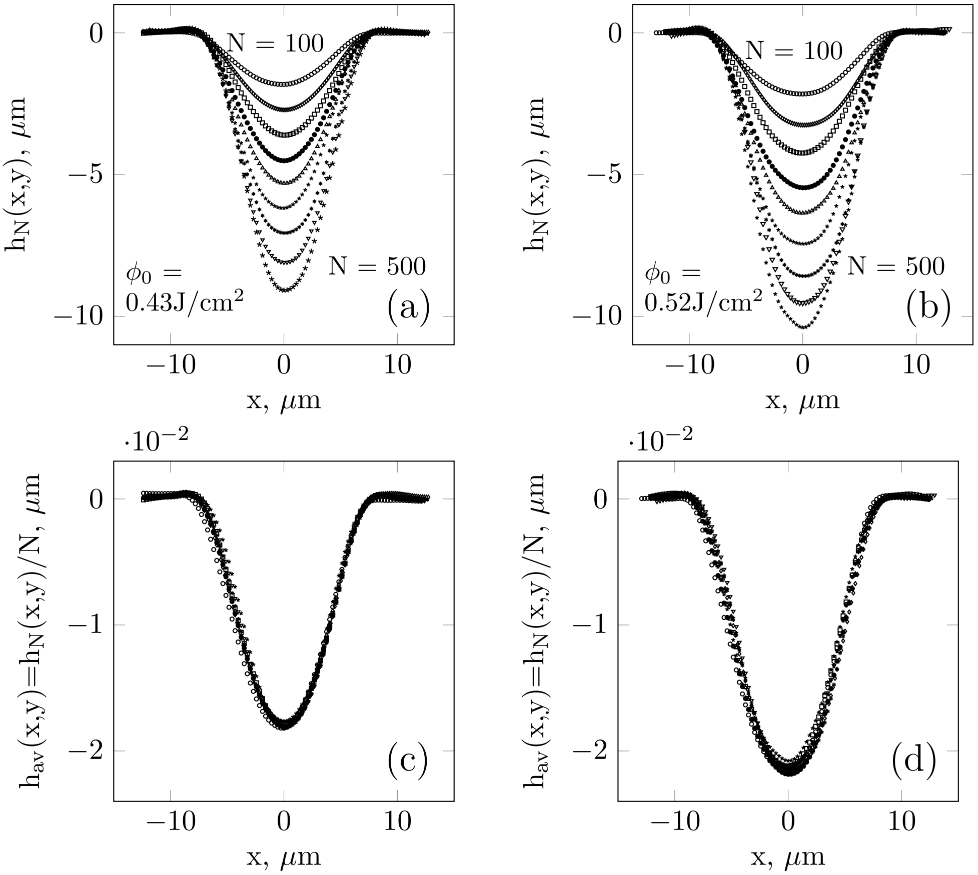

Figure 4.4.: Cross section of fitted ablated profiles obtained by CLSM, (a) and (b), and corresponding average ablated profiles $h_{av}(x, y)$, (c) and (d), created on a stainless steel X5CrNi18-10 surface after a number of pulses, N, ranging from 100 to 500. Peak incident fluence levels 0.43 J/cm^2, (a) and (b), and 0.52 J/cm^2, (c) and (d). Note the scale difference in depth between (a), (b) and (c), (d).

Next, a linear fit, in the form $h_N(x, y) = h_{av}(x, y) \cdot N$, was therefore attempted, to relate the ablated depth at each location, $h_N(x, y)$, to the applied number of pulses, N. Each measured ablated profile was first centered and subsequently averaged, following the procedure described in appendix I. At least 5 independent measurements were employed per pair of pulse energy and number of pulses, to reduce statistical errors. The slope of the linear fit yields the average ablated depth per pulse at a location, in nm/pulse, for the given material and range of applied pulses at a given energy per pulse. Figure 4.5 shows the location of 4 points across the diagonal of a measured ablated profile, which are below used to illustrate the performed linearity analysis at these

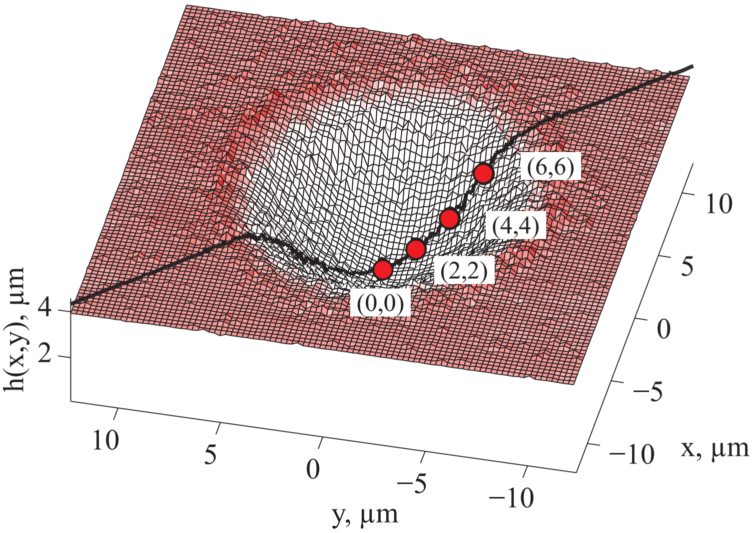

Figure 4.5.: Average ablated depth (nm/pulse) at 4 locations situated at increasing radial distance, r, from the center of the modified area, across the diagonal; (a) to (d), respectively, 0 (center), 2, 4 and 6 μm. Processing conditions: <7 ps pulses at 515 nm, peak incident fluence 0.43 J/cm^2. Substrate: polished stainless steel X5CrNi18-10.

locations.

Figure 4.6 shows four typical linear fits calculated at four locations within the ablated profile created at 0.43 J/cm^2, in figure 4.5. That is at: the central point, (a), and three points successively displaced 2 μm across the diagonal, following the radial direction, respectively (b), (c) and (d). The average ablated depth at each location, calculated from the fit, results in an ablated depth rate of 18, 12, 8 and 4 nm/pulse. The distribution of the residuals (bar plots in Figure 4.6) does not suggest systematic deviations from the linear fit. This confirms the linear relation between ablated depth and applied number of pulses for the selected fluence range and range of number of pulses.

An average ablated profile was obtained by simply repeating the calculation to include all the locations in the xy plane. Figures 4.7(a) and (b) shows the resulting averaged ablated profile, for the the selected peak fluences of respectively 0.52 J/cm^2 and 0.43 J/cm^2. Figures 4.7(c) and (d) depict two typical cross sections across the ablated profiles, showing the mean ablated depth at each location along the x-axis. The error bars indicate 95% confidence intervals for the calculated depth values. It can be noticed that, the maximum ablated depths, of respectively 18 and 21 nm, fall within typical values for the optical penetration depth of metals at these energy levels, see table 3.1. The

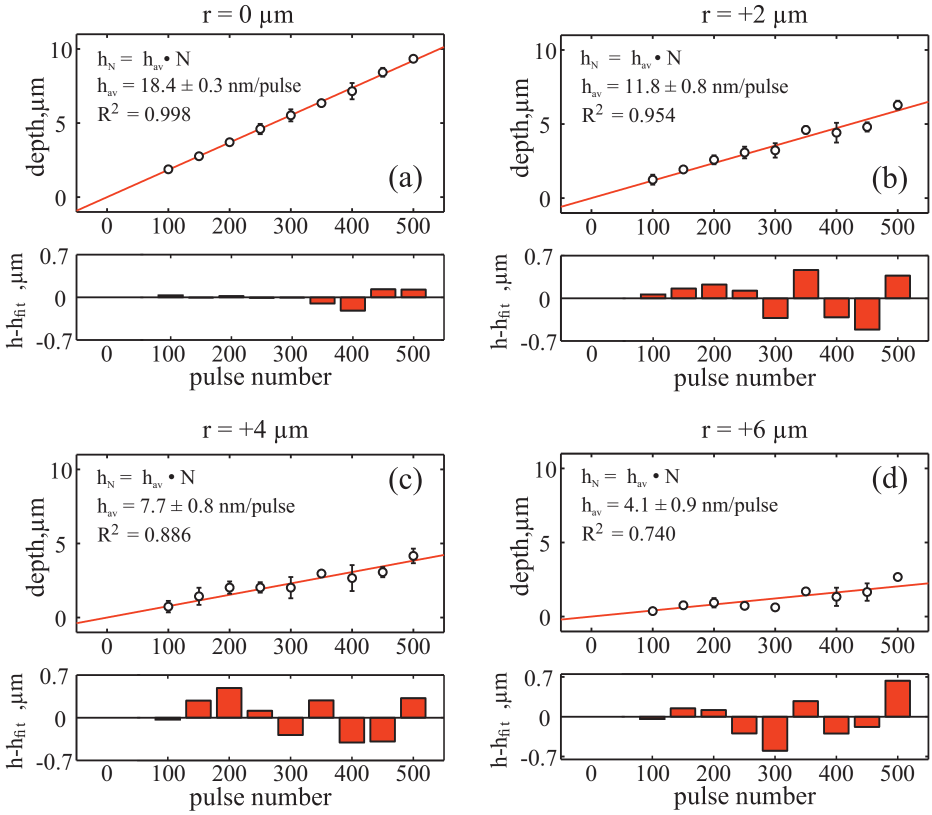

Figure 4.6.: Average ablated depth (nm/pulse) at 4 locations situated at increasing radial distance, r, from the center of the modified area, across the diagonal; (a) to (d), respectively, 0 (center), 2, 4 and 6 μm. Processing conditions: <7 ps pulses at 515 nm, peak incident fluence 0.43 J/cm^2. Substrate: polished stainless steel X5CrNi18-10.

cross-sections, figures 4.7(c) and (d), also reveal a certain asymmetry of the surface profile, which was attributed to the (measured) asymmetry of the laser intensity profile.

4.5. Pulse frequency range

Heat accumulation effects have to be addressed before the simulation of a multi-pulsed process based on the calculation of average ablated profiles derived in the previous section. That is because the model assumes that dissipation of residual heat into the bulk is negligible.

As mentioned before, stainless steel has a short thermalization time, which may be approximated by the electron–phonon relaxation time of iron, which is approximately 0.5 picoseconds [10]. The energy transfer from the electron

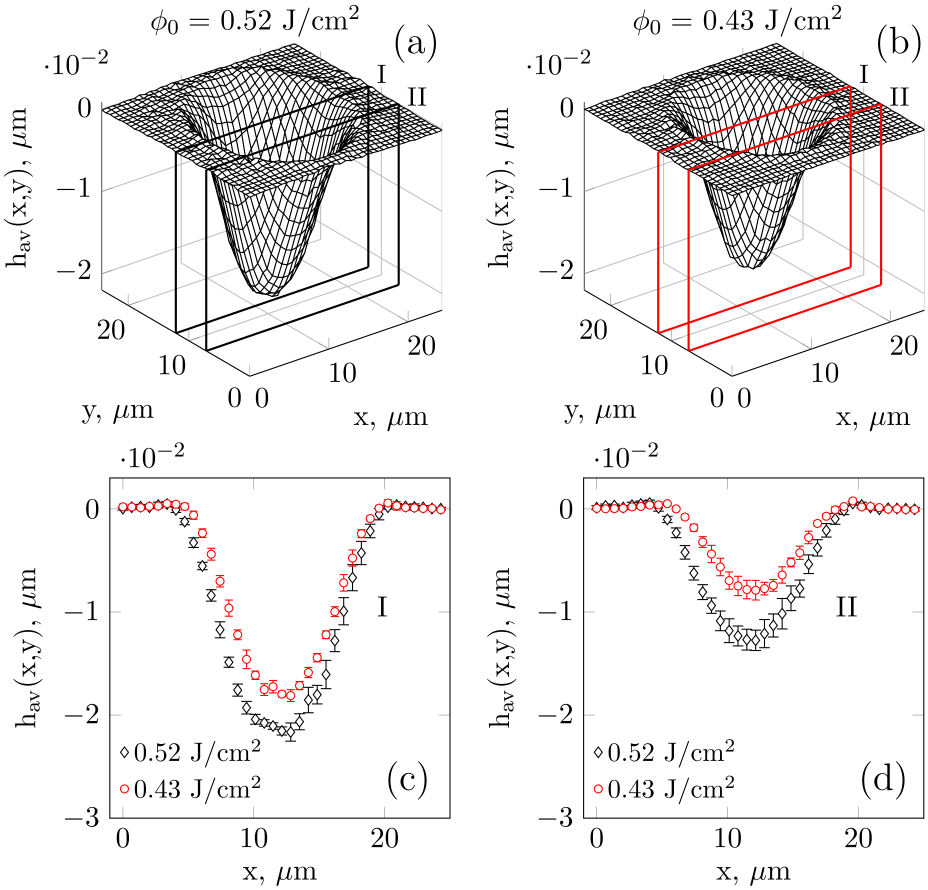

Figure 4.7.: Average ablated profiles (a) and (b), and cross sections at two selected locations: plane I, center (c), and plane II, 5 μm parallel displaced from the center plane, (d). Processing conditions: <7 ps pulses, 515 nm, peak incident fluence 0.52 J/cm^2, (a), and 0.43 J/cm^2 (b). Substrate: polished stainless steel X5CrNi18-10.

subsystem to the lattice occurs then rapidly. In addition, the relatively low thermal diffusivity of stainless steel reduces the rate of heat dissipation into the bulk. As a result, the absorbed energy is efficiently confined to the surface of stainless steel. These optical and thermal properties are in agreement with the hypothesis of negligible heat dissipation into the bulk, provided that the time between laser pulses is long enough to allow for a quick dissipation of the residual heat from the laser-material interaction zone. If the pulse repetition rate is increased, the time between subsequent laser pulses reduces. Hence, it is expected that at a certain pulse rate accumulation of heat may alter the linearity of the multi-pulsed material removal process.

Ancona et al. [73] studied the effects of processing with high repetition rates on the number of pulses required to drill through a 0.5 mm thick stainless steel sheet with picosecond laser pulses. The required number of pulses to drill through the sheet was constant for repetition rates up to 400 kHz and fluence levels above 10 J/cm^2. For pulse rates over 400 kHz, the required number of pulses to drill through the sheet decreased. This was attributed to the additional contribution due to heat accumulation. The laser source employed in this thesis operates at a maximum repetition rate of 400 kHz and, therefore, does not allow for a complete study of heat accumulation effects on metallic substrates.

The material removal in a multi-pulsed process was considered to proceed without significant heat accumulation. In order to assess the validity of this hypothesis, the average ablated profiles from the previous section will be directly employed in the following to predict the surface profiles, according to a predefined machining strategy. In order to trigger any heat accumulation, the repetition rate of the laser source was fixed to its maximum of 400 kHz. If relevant inter-pulse effects, e.g., due to heat accumulation are significant at this pulse rate, the average ablated depth per pulse $h(x, y)$ should increase, resulting in an underestimation of the ablated depth per pulse. This inaccuracy would become apparent when comparing calculated and measured data from the resulting surface profiles, $H(x, y)$. The accuracy of the predictions of the model is examined in the next section, by comparing calculated and measured surface profiles which are micromachined at the maximum repetition rate of the laser source.

4.6. Simulation & validation of a surface microstructuring process

The calculation of average ablated profiles $h_{av}(x, y)$ allows for the simulation of a microstructuring process. Recall that, this process consists, in general, of scanning a laser spot according to a given machining strategy (i.e. a trajectory of the laser spot over the surface), resulting in partially overlapping laser pulses to remove material from a surface. This material removal process by multiple laser pulses leads to a microstructured surface, $H(x, y)$.

The hatched pattern, introduced in section 3.5, was employed as the machining strategy for this validation. Here, the distance between parallel laser tracks, referred to as the hatch distance h_d, and the number of layers to be applied, were systematically varied from 16 to 19 μm and from 40 to 70 laser cycles, respectively, to calculate several microstructures. The ablated profile $h(x, y)$, obtained at a peak fluence value of 0.43 J/cm^2, shown in figure 4.7(c), was employed for the simulations.

The accuracy of the predictions of the model was examined by comparing

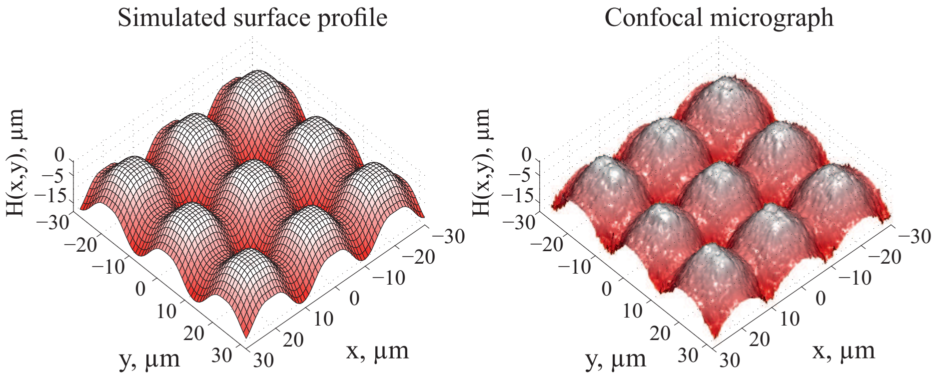

Figure 4.8.: Calculated surface profile (left) and measured surface profile (right) obtained from the following processing conditions: peak fluence 0.43 J/cm^2, <7ps pulses at 515 nm, 94% pulse to pulse overlap, distance between the laser tracks: 19 μm. 40 laser cycles are applied.

calculated surfaces and measured surface profiles obtained after laser processing. As the coordinate systems of the simulations and the confocal microscope do not coincide, the x-y coordinates of the measurements need to be aligned to the x-y coordinates of the simulations, for a fair comparison between model and experiment. Figure 4.8 shows a simulated and a measured surface profile after the alignment process. This alignment was based on a procedure to find a reference position, $(x_{ref}, y_{ref}, H_{ref})$ as well as a relative orientation, ψ, of the coordinates of the model, $(x, y, H)_{model}$, and the coordinates of the measurement, $(x, y, H)_{measured}$, that minimizes the root–mean square deviation, $\sigma_{x,y,\psi}$ as

$$\sigma_{x,y,\psi} = \sqrt{\frac{1}{n-1} \sum_{\forall H(x,y)} (H_{model} + H_{ref} - H_{measured})^2} \tag{4.1}$$

Figure 4.9 shows the result of the comparisons between simulations and measured surface profiles. The simulated surfaces are depicted, employing the calculated relative error $(100 \cdot (H_{measured} - H_{model})/H_{measured})$ at each location to color the surface. As can be observed from this figure, the relative error increases with number of laser cycles. For 60 laser cycles or less, the relative error of the model is less than 8 %.

Figure 4.10 shows a comparison between simulated and measured surface profiles, (a) and (b) respectively, as well as two cross sections, (c) and (d), respectively aimed at a direct visual comparison of the results of this modelling approach, for the following processing conditions: peak incident fluence 0.43 J/cm^2, <7 ps pulses at 515 nm, 94% pulse to pulse overlap, distance between

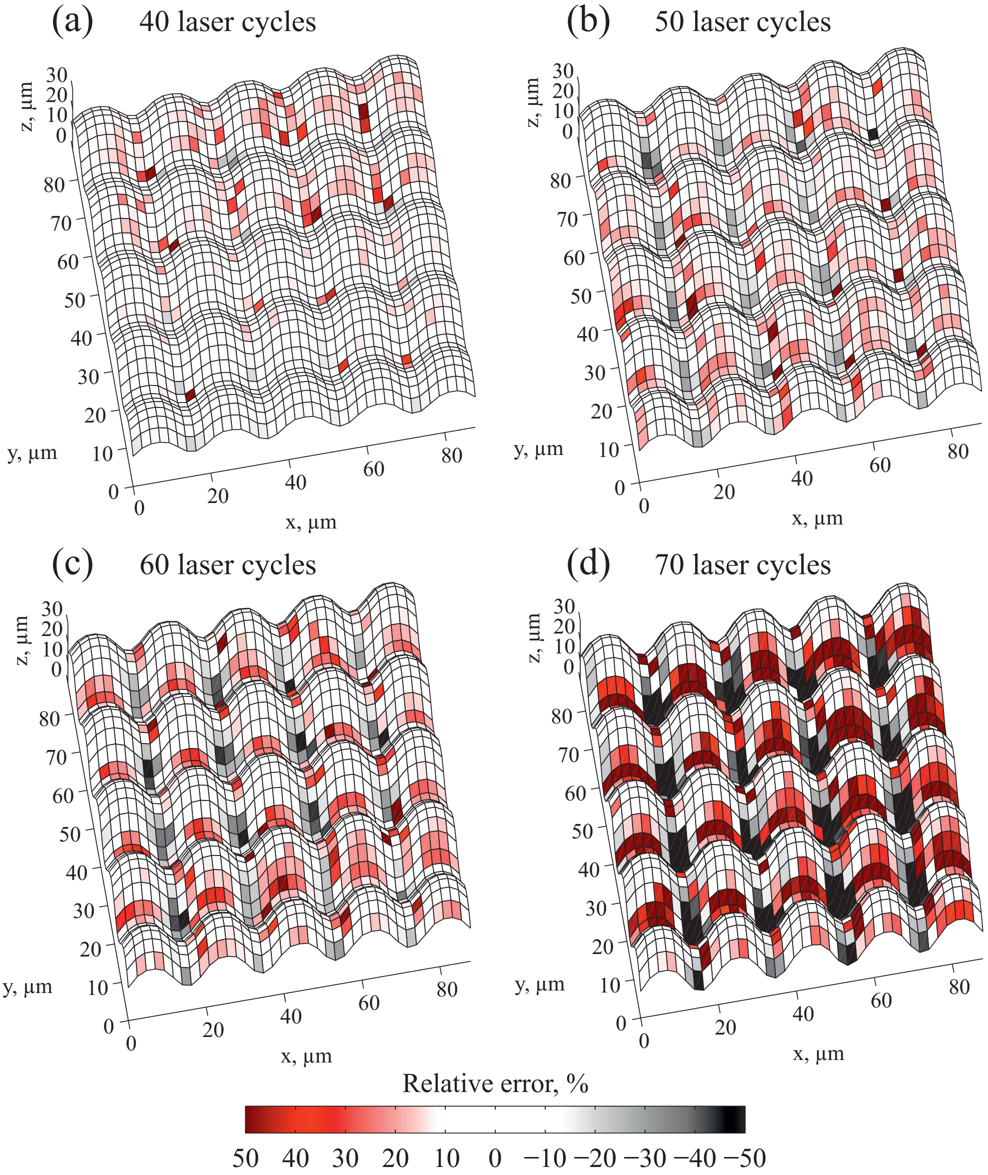

Figure 4.9.: Comparison between the simulated surface profiles and experimentally obtained surface profiles after increasing number of laser cycles, 40, 50, 60 and 70 respectively (a), (b), (c) and (d). Processing conditions: peak incident fluence 0.43 J/cm^2, <7 ps pulses at 515 nm, 94% spatial pulse to pulse overlap, distance between parallel laser tracks, $h_d = 19$ μm. The relative error between the simulation and the experimental data (in %) is visualized by the colormap indicated by the colorbar.

Table 4.4.: Root mean squared (RMS) and normalized root mean squared of the deviations of a cross section of a simulated area of 90x90 μm and a 2D profile, along the diagonal of the simulated area, as a function of the number of laser cycles. Processing conditions: peak incident fluence 0.43 J/cm^2, <7 ps pulses at 515 nm, 94% pulse to pulse overlap, distance between parallel laser tracks 19 μm.

Figure	Laser cycles	RMS area, μm	NRMS area, %	RMS diagonal, μm	NRMS diagonal, %
4.10	40	1.2	6.5	0.9	5.1
4.11	50	1.5	6.8	1.5	7.2
4.12	60	2.0	7.7	1.5	6.7
4.13	70	2.8	12.1	2.8	12.2

the laser tracks: 19 μm and 40 laser cycles. Figures 4.11 to 4.13 show similar comparisons for 50, 60 and 70 laser cycles, respectively.

For further numerical comparison between simulations and experiments, the root–mean square (RMS) and normalized root–mean square (NRMS) of the deviations of the simulated areas and cross sections across its diagonals were determined. Table 4.4 summarizes these results. These respective calculated and measured surfaces and the cross sections are shown in Figures 4.10 to 4.13, on pages 57 to 60. As can be observed from these figures and from the statistical values in table 4.4, the model is capable of predicting the resulting surface profiles with an error less than 8%, up to 60 laser cycles.

Finally, figure 4.14, on page 61, shows a last comparison between simulated and measured surfaces, in the case the hatch distance h_d between the laser tracks is varied from 16 to 20 μm. It can be observed that the accuracy of the predictions does not qualitatively change as the hatch distance is varied, for a fixed number of laser cycles.

The accuracy of the model is progressively reduced as the number of laser cycles increases, but it is insensitive to the separation of the laser tracks. The areas showing larger deviations between calculated and experimental data are located at the cross of the laser tracks, where the deepest valleys are created. In addition, for an increasing number of cycles over 60, the prediction at the center of the (deeper) laser tracks becomes inaccurate as well.

As a microstructure becomes deeper, multiple reflections within the generated cavities may enhance the absorption of optical energy, resulting in an increased efficiency for the material removal process. This effect would explain the underestimated ablated depth at the center of the laser tracks. As the number of laser cycles is further increased, the predicted depth at the slopes of the microstructure is also underestimated, see red areas in figure 4.9.

This might be attributed to additional mechanisms for material removal, such as the generation of a plasma after ignition of the ablated particle cloud. With increasing number of laser cycles, the ejected particle cloud becomes confined by the created microstructure, so it might not diffuse quick enough out of the interaction volume, before the next pulse arrives to the substrate. The ignition of the ablated vapour cloud has been proposed as an additional mechanism for material removal by short laser pulses [74].

Further, as a microstructure becomes deeper, the removed material might accumulate within the generated cavities, reducing the efficiency of the material removal process, see black areas of figure 4.9. These effects are in accordance with the onset of the phenomena occurring at deep valleys, as discussed in section 3.6. However, the accuracy of the CLSM measurements also depends on the depth of the microstructure. The CLSM employs an optical signal coming from the reflection of a laser beam on the surface that is being measured. As a structure becomes deeper, the strength of the reflected optical signal decreases, and measurement uncertainty is introduced. This effect reaches a maximum when measuring the depth at the cross of the laser tracks, black areas in figure 4.9. This uncertainty in the measured depth would also justify the apparent inaccuracy of the model at the deepest locations. In spite of these uncertainties, the model will be shown to suffice for the simulation of the functional microstructures which are the subject of study in this work.

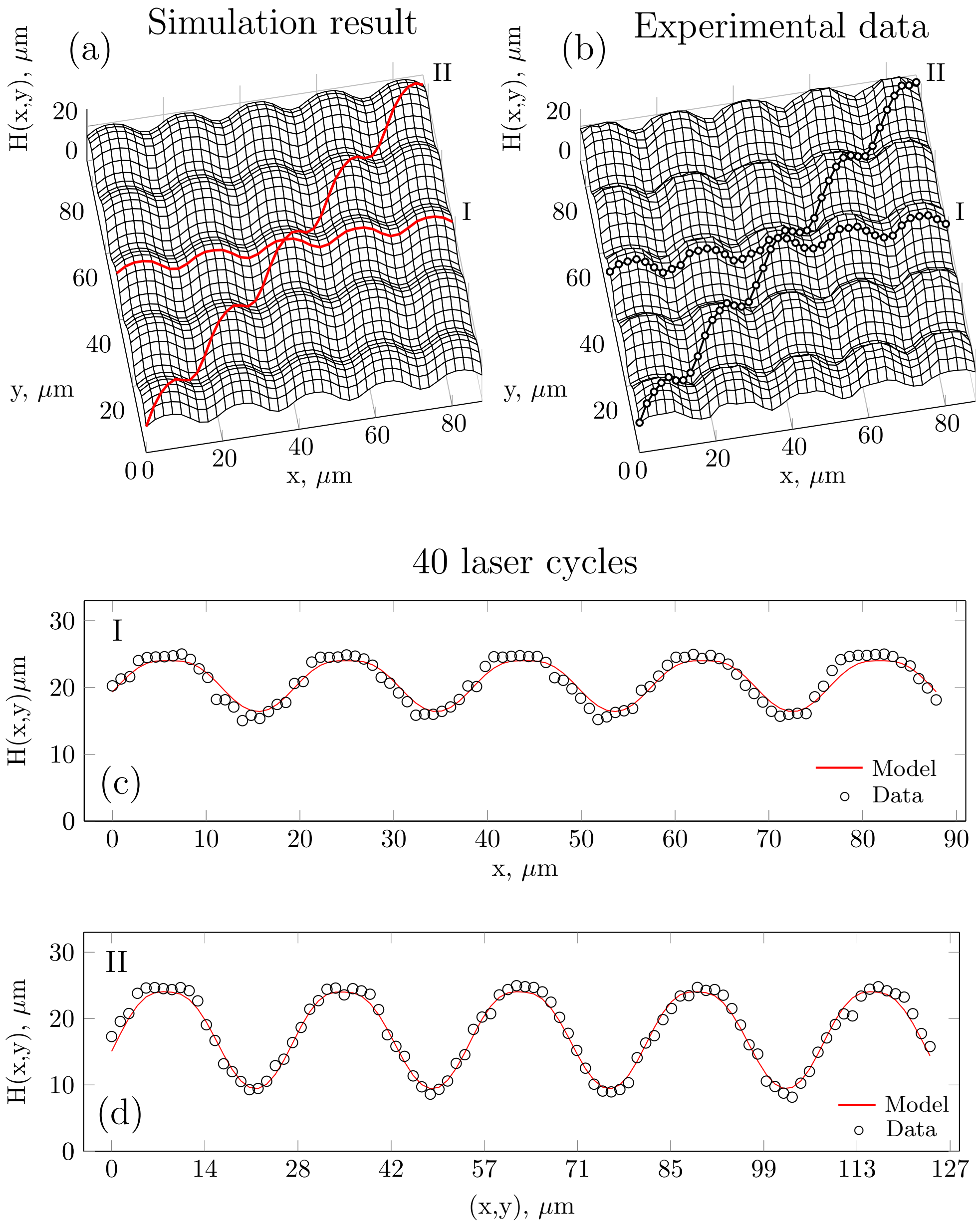

Figure 4.10.: Simulated (a) and experimental (b) surface profiles measured by CLSM, as well as cross sectional comparisons, (c) and (d), between simulated and measured structures at processing conditions: peak incident fluence 0.43 J/cm^2, <7 ps pulses at 515 nm, 94% pulse to pulse overlap, distance between the laser tracks: 19 μm. 40 laser cycles are applied.

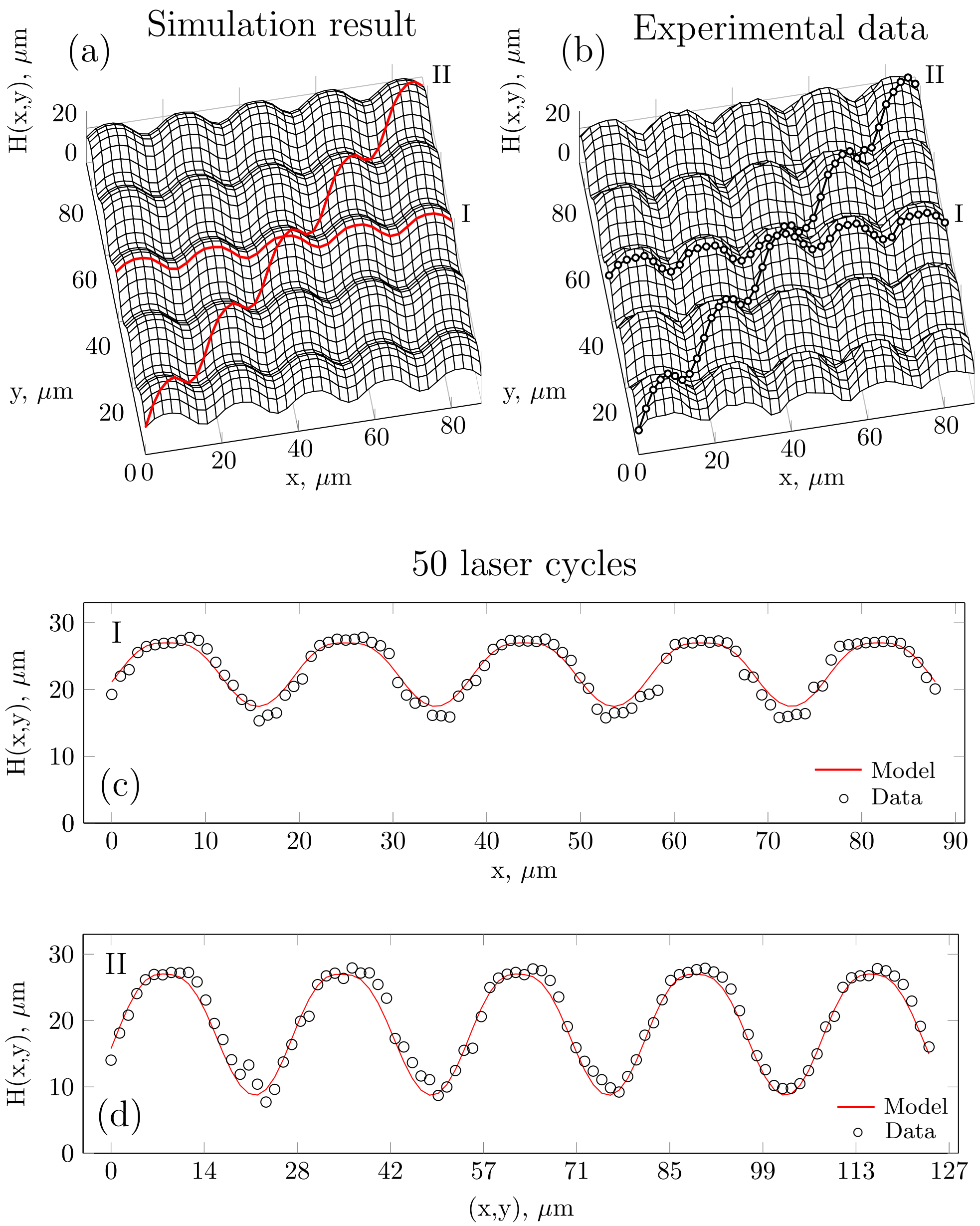

Figure 4.11.: Simulated (a) and experimental (b) surface profiles measured by CLSM, as well as cross sectional comparisons, (c) and (d), between simulated and measured structures at processing conditions: peak incident fluence 0.43 J/cm^2, <7 ps pulses at 515 nm, 94% pulse to pulse overlap, distance between the laser tracks: 19 μm. 50 laser cycles are applied.

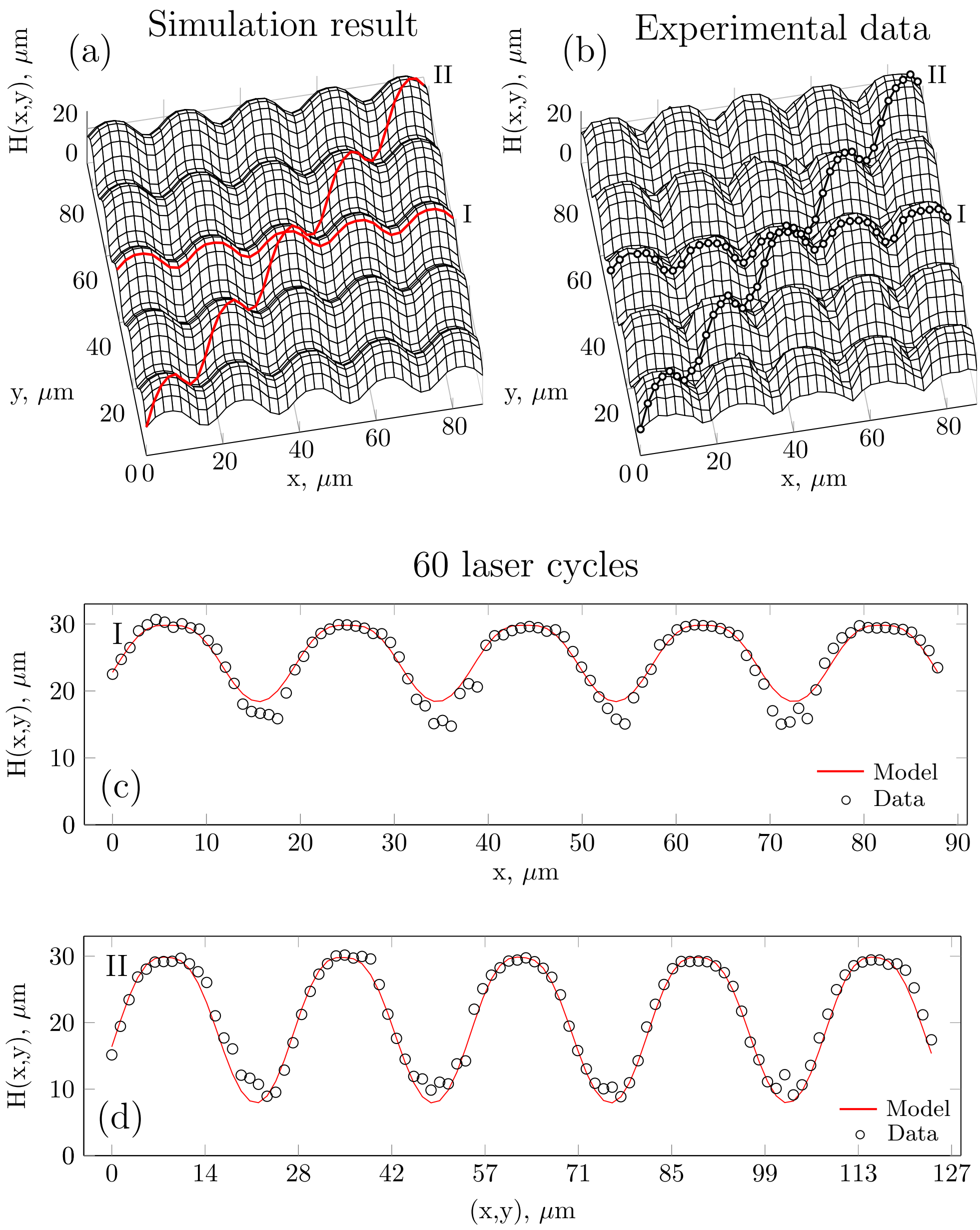

Figure 4.12.: Simulated (a) and experimental (b) surface profiles measured by CLSM, as well as cross sectional comparisons, (c) and (d), between simulated and measured structures at processing conditions: peak incident fluence 0.43 J/cm^2, <7 ps pulses at 515 nm, 94% pulse to pulse overlap, distance between the laser tracks: 19 μm. 60 laser cycles are applied.

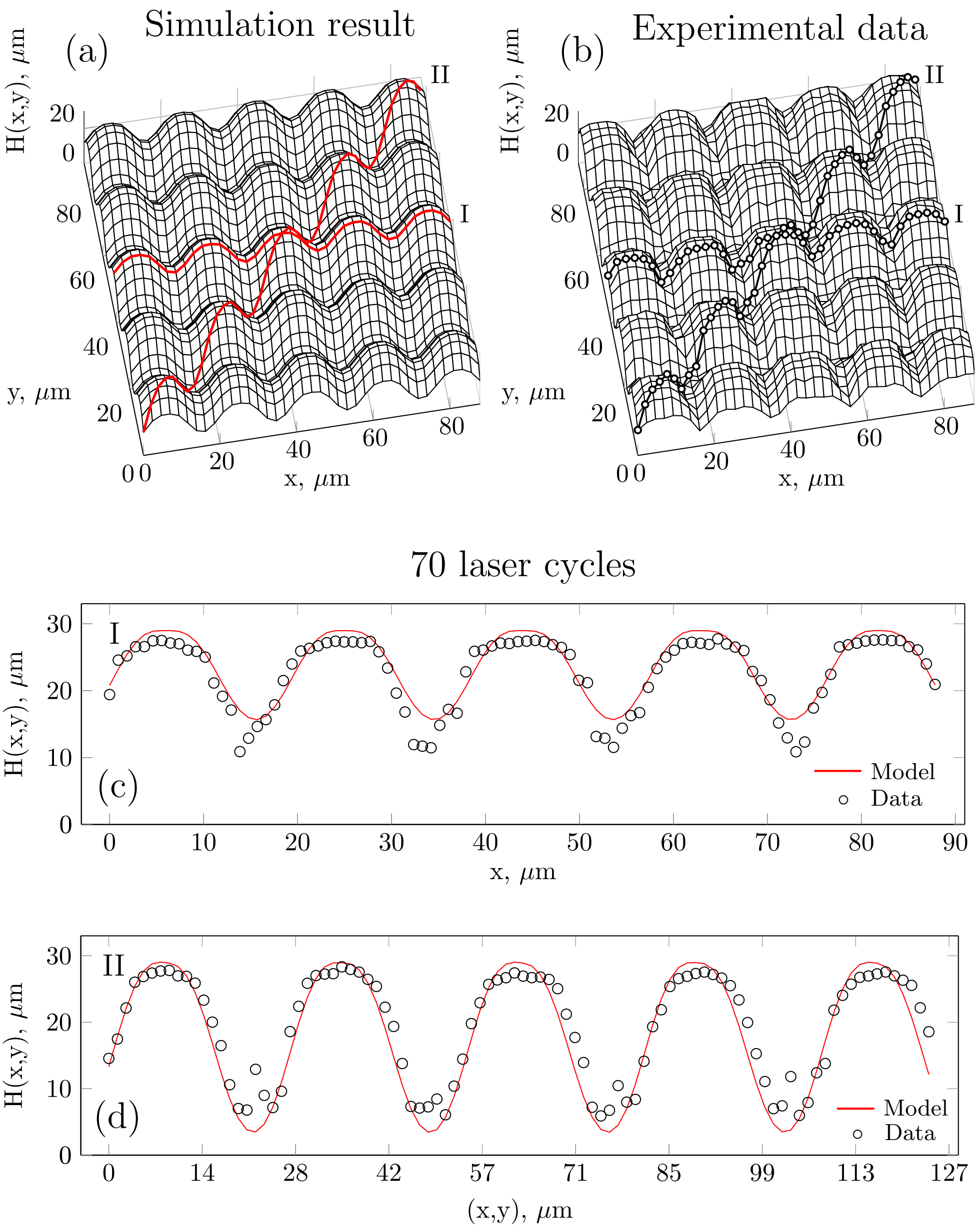

Figure 4.13.: Simulated (a) and experimental (b) surface profiles measured by CLSM, as well as cross sectional comparisons, (c) and (d), between simulated and measured structures at processing conditions: peak incident fluence 0.43 J/cm^2, <7 ps pulses at 515 nm, 94% pulse to pulse overlap, distance between the laser tracks: 19 μm. 70 laser cycles are applied.

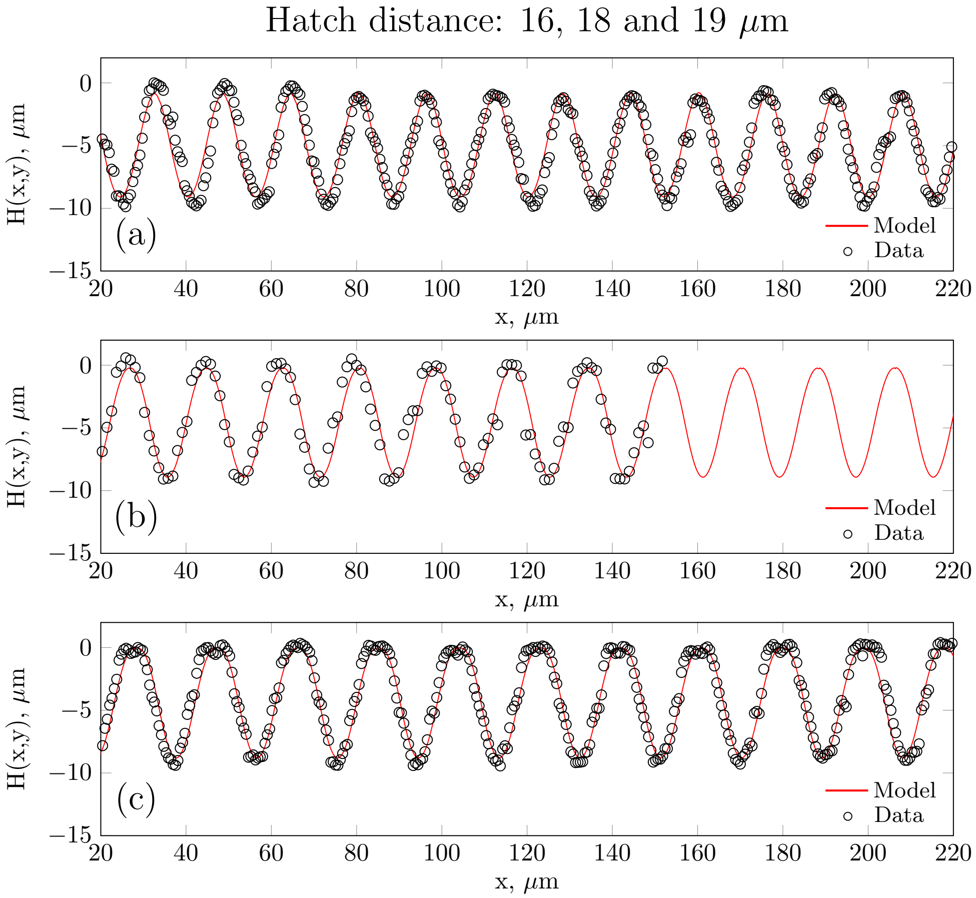

Figure 4.14.: Cross sectional comparison of simulated and experimental structures for three values of the hatch distance h_d between laser tracks, respectively top figure to bottom figure: 16, 18 and 19 μm. Processing conditions: peak incident fluence 0.43 J/cm^2, <7ps pulses at 515 nm, 94% pulse to pulse overlap, 40 laser cycles.

4.7. Conclusions

The material removal process of a stainless steel X5CrNi18-10 grade by picosecond laser pulses was shown to be linear with respect to the applied number of pulses, for a limited regime. Average ablated profiles were calculated by extending a linear fit, relating depth with the applied number of pulses, to all locations exposed to the laser radiation. The process window of the linear model was determined in terms of the applied pulse energy. The processing conditions leading to the so–called cold ablation regime were shown to give a reproducible linear multi-pulsed process, for a range of incident fluence below 0.8 J/cm^2, and number of applied pulses ranging from 100 to 500.

An extended analysis for the selected substrate revealed the applicability of the model for the simulation of microstructures, up to a maximum depth of about 20 μm. Experimental data showed that the multi-pulsed material removal process is linear with the number of pulses up to a pulse repetition rate of at least 400 kHz.

Part II.

Laser-generated functional microstructures

5 Laser-generated functional microstructures

5.1. Introduction to part II

The model developed in chapter 3 and validated in chapter 4 is employed in this second part of this thesis, as a tool for the design of fluidic microstructures, as well as for the investigation of different fluidic functionalities based on these structures. Moreover, simplified fluidic models are introduced, to relate the geometry of a microstructure to the fluid-microstructure interaction. This step allows for the calculation of the laser processing parameters, i.e. the laser machining strategy, that is required to obtain a desired functional microstructured surface. Further, modifying key geometrical parameters, as for example depths or slopes of the microstructure, allows investigating some of the fluidic mechanisms responsible for the functionality. Hence, additional knowledge on the fluid-microstructured surface interaction can be (and will be) gained by this approach. The following functional surfaces are further considered in the second part of this thesis:

- superhydrophobic surfaces,
- Leidenfrost point reduction on microstructured surfaces, and
- capillary droplets on Leidenfrost micro-ratchets,

each of which will be briefly introduced in the remainder of this chapter.

5.2. Superhydrophobic surfaces

As already indicated in chapter 1.2, laser micromachining can be employed as a tool for creating surfaces with extreme water repellent properties. That is, water drops bed up and roll easily of these surfaces, which are therefore referred to as superhydrophobic. In chapter 6, the hatched crossed pattern introduced in the previous chapters (see for example section 3.5 and figure 3.4) is exploited to create microstructures on a stainless steel substrate which is afterwards coated to obtain surfaces with water repellent properties. The geometry obtained after applying selected laser processing conditions is combined with the chemical properties of the material, to predict the resulting water repellency.

The contribution of multiple scaled surface roughnesses to water repellency has also been the subject of extended research [75–78]. That is, dual micrometric & sub-micrometric scaled roughnesses can be created, by proper selection of the laser processing conditions. The relative contribution of each roughness scale to the wetting properties of a substrate is experimentally verified and discussed in chapter 6, as well as in two papers:

- Arnaldo del Cerro, D. and Römer, G.R.B.E. and Huis in 't Veld, A.J. *Picosecond laser machined designed patterns with anti-ice effect.* In: 11th International Symposium on Laser Precision Microfabrication (LPM 2010) Stuttgart, June, 7-10, 2010 , referred to as paper A.
- Römer, G.R.B.E. and Arnaldo del Cerro, D. and Sipkema, R.C.J. and Groenendijk, M.N.W. and Huis in 't Veld, A.J. *Ultra short pulse laser generated surface textures for anti-ice applications in aviation*, pp. 30-37 in Proceedings of the ICALEO 2009, Orlando, USA, November, 2-5, 2009, referred to as paper B.

Paper A analyses the relation between the wetting properties of several laser-machined microstructures. Both the geometry of the microstructures, as well as their chemical composition, are shown to lead to the desired functionality. Paper B provides an extended experimental analysis of the water repellent properties of a superhydrophobic surface in order to achieve a substrate with ice-repellent properties. Both papers can be found after chapter 6, starting from page 83.

5.3. Leidenfrost point reduction on microstructured surfaces

A liquid droplet levitates above its own vapour, when deposited on a hot surface exceeding a critical temperature, which is referred to as the Leidenfrost point [79]. The Leidenfrost point depends on several factors. One of the most studied factors has been the surface roughness. Traditionally, the surface roughness has been shown to increase the temperature required to observe the phenomenon [80–83]. However recently, micrometric surface patterns have been shown to be capable of decreasing the Leidenfrost point [84].

In chapter 7, laser micromachining is employed as a tool for the design of surface microstructures that substantially reduce the Leidenfrost point. The relation between the decrease of the Leidenfrost point and the geometry of the microstructures is further discussed. In the paper Arnaldo del Cerro, D. and Marín, Á.G. and Römer, G.R.B.E. and Pathiraj, B. and Lohse, D. and Huis in 't Veld, A.J. *Leidenfrost Point Reduction on Micropatterned Metallic Surfaces*, Langmuir 28(42):15106-15110, 2012, referred to as paper C, the contribution of the size and spatial distribution of the created surface features to the measured temperature reduction is analyzed. This paper can be found after chapter 7, starting from page 95.

5.4. Capillary droplets on Leidenfrost micro-ratchets

A liquid drop levitating on a surface at a temperature above the Leidenfrost point drifts freely across the surface. However, when the surface is covered with an asymmetric ratcheted microstructure, a force is exerted on the droplet and as a result it will move in a preferential direction. The mechanisms responsible for this directional flow are the subject of current fundamental research [85–88]. The laser microstructuring process employed in this work is exploited for the creation of well–defined asymmetric surface microstructures, which promote the directional flow of droplets.

More specifically, in chapter 7, several machining strategies leading to micrometric sized ratchets are analyzed & discussed. The resulting micrometric-sized ratchets allow propelling capillary drops and, as a consequence, studying the physical mechanism for the directional flow. The paper Marin A.G. and Arnaldo del Cerro D. and Romer G.R.B.E. and Pathiraj, B. and Huis in 't Veld A.J. and Lohse D. *Capillary droplets on Leidenfrost micro-ratchets*, Physics of Fluids, 2012;24(12):122001-10, referred to as paper D, includes measured accelerations and velocities of the droplets, which are fitted to a simplified model for the force exerted on the drop, to provide evidence supporting one of the proposed mechanisms for the flow. This paper can be found after chapter 7, starting from page 105.

6 Superhydrophobic surfaces

Microstructuring by (ultra) short laser pulses can be employed to modify the wetting properties of a surface. This chapter is aimed at determining a suitable laser micro-machining process that allows for the creation of a surface topography with water repellent properties. An additional study on the potential ice-repellent properties of a water repellent surface is discussed in papers A and B, which are part of this chapter.

6.1. Introduction

As discussed in chapters 1 and 3, the wetting properties of a broad range of materials can be modified by texturing the surface using laser micromachining with short and ultra short laser pulses. Adjusting the surface profile of a substrate to create a microstructure allows the generation of water-repellent surfaces. First, the wetting properties of microstructured substrates are discussed in the following, in order to relate the geometry of a micrometric structure to the desired water repellent functionality. Next, the model developed in chapter 3 is employed to establish the laser processing conditions required to obtain such geometries. Finally, an extended analysis of the potential use of a laser-generated water repellent surface as an anti-ice substrate is further discussed in papers A and B at the end of this chapter.

6.2. Wetting of solid surfaces

The wetting properties of a solid–liquid–vapour system are commonly assessed by means of contact angle measurements. The contact angle that a liquid drop exhibits, when sitting on top of an ideal flat surface, is given by the balance of capillary forces acting at the liquid–solid–vapour interface [89], see figure 6.1.

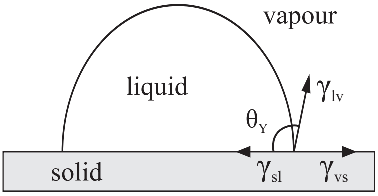

Figure 6.1.: Solid-liquid-vapour system and definition of contact angle.

This angle is referred to as the Young contact angle, θ_Y [90], and follows from

$$\cos\theta_Y = \frac{\gamma_{vs} - \gamma_{sl}}{\gamma_{lv}} \tag{6.1}$$

where γ_{vs}, γ_{sl}, and γ_{lv} are the vapour–solid, solid–liquid and liquid–vapour interfacial tensions respectively. When water is the liquid under consideration and θ_Y takes values above 90°, the surface is commonly referred to as hydrophobic, and hydrophilic, if θ_Y is below 90°. The maximum value that θ_Y can take for water drops on a smooth surface is about 120° [6, 91].

The wetting properties of a surface depends both on the chemical composition and topography of the surface. If chemical heterogeneities and/or a certain roughness level are present on the surface, the contact angle cannot be calculated by Young's relation of equation (6.1). However, a liquid drop frequently adopts the shape of a spherical cap when sitting on a rough substrate. Then, an *apparent* contact angle, APCA, can be defined to measure the tendency of a liquid to spread across a rough or chemically heterogeneous substrate [89].

Apparent contact angles above 150°, and up to a maximum of 174°, have been measured for water drops sitting on different natural and artificial surfaces [7, 76, 89, 91]. On such surfaces, millimetric sized drops tend to bead up and roll-off when the surface is slightly tilted. Surfaces with these characteristics are commonly referred to as superhydrophobic.

When a solid-liquid-vapour contact line is in motion, e.g. when a droplet rolls-of a sloped surface, or when a droplet volume is increased/decreased by pumping, two different *dynamic* contact angles can be measured at the moving contact line. These angles will in general take different values, while the contact line advances or recedes across an area, see figure 6.2. These angles are respectively referred to as the *advancing* and *receding* contact angles. The maximum difference between these angles is referred to as the *contact angle hysteresis*, CAH [6, 7].

If the contact angle hysteresis approaches zero, a liquid drop offers little resistance towards movement when an external force is applied to it. On a perfectly homogeneous flat surface, the contact angle hysteresis approaches zero. A small contact angle hysteresis is also a fundamental property of a

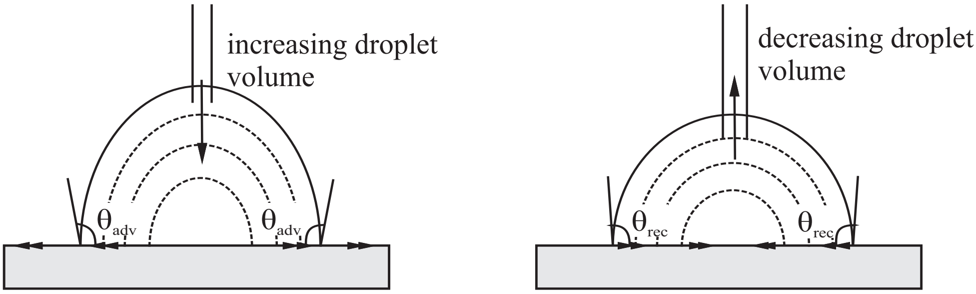

Figure 6.2.: Definition of contact angle hysteresis. The contact angle hysteresis is the difference between the advancing and receding contact angles, respectively θ_{adv} and θ_{rec}.

superhydrophobic surface. A superhydrophobic surface is defined by that surface having both a high water apparent contact angle, which is larger than 150°, and a low contact angle hysteresis which is below 10° [4].

It is worth to mention that, as the maximum θ_Y that can be achieved on a perfectly flat surface is limited to about 120°, a surface can only be superhydrophobic when a suitable topography (or roughness level) is present. Therefore, in the next section, the wetting properties of rough substrates are further discussed.

6.3. Wetting of rough substrates: Cassie–Baxter and Wenzel states

The apparent contact angle of a droplet sitting on a rough surface can be estimated using two different models, depending on the *wetting state* of the liquid-solid-vapour system. If the wetting state is such that a liquid drop is in full contact with the solid, see figure 6.3(b), the so called Wenzel model applies [92]. According to this model, the apparent contact angle, θ_r^w [deg] follows from

$$\cos\theta_r^w = r\cos\theta_Y, \tag{6.2}$$

where r [$-$] is the ratio between the actual area and the geometric (projected) area of the surface, and θ_Y is Young's contact angle, as defined by equation (6.1) [90]. It follows from the Wenzel model that, when a surface has a low tendency to be wet by a liquid or, in other words, has a low surface energy, and if θ_Y is above 90° as well, increasing its roughness will further decrease the spreading of the liquid over the surface, and vice versa.

Equation (6.2) is not appropriate for describing the wetting of rough surfaces beyond a certain roughness level. In that case, a different wetting state, in

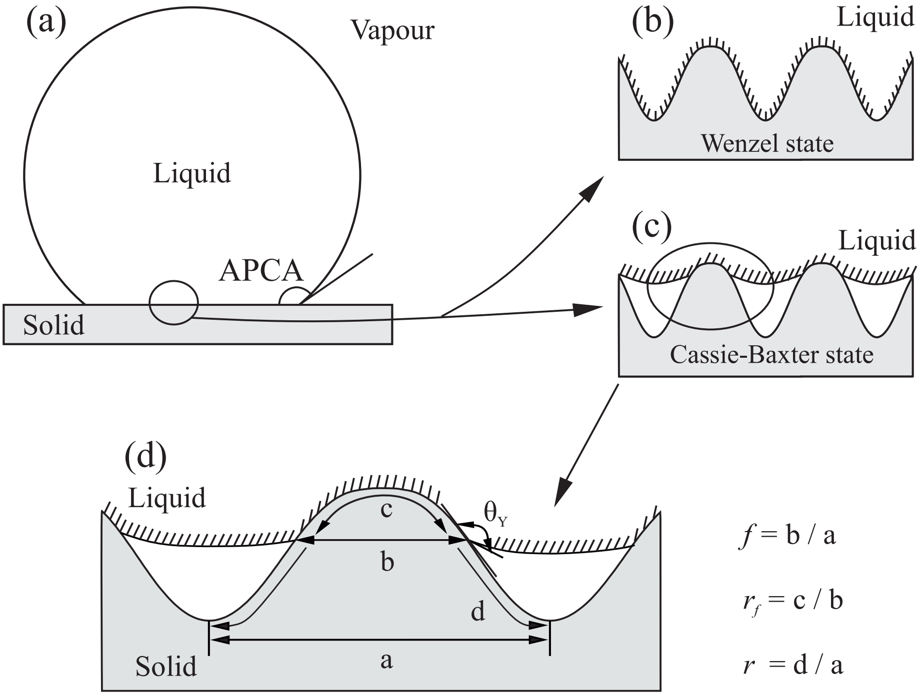

Figure 6.3.: (a) A droplet sitting on top of a rough substrate showing an apparent contact angle, APCA. (b) Wenzel state, (c) Cassie–Baxter state. (d) Roughness definition for the Cassie-Baxter state.

which the liquid drop sits on top of the peaks of the rough substrate may occur, see figure 6.3(c). In this situation, air is trapped at the deeper parts (valleys) of the surface roughness, so the liquid is not in full contact with the solid. This wetting state is usually referred to as the Cassie–Baxter state [93], and may occur when a surface topography consists of micro-metric sized features which are ‘‘tightly packed’’. The apparent contact angle for the Cassie–Baxter state, θ_r^c [deg], follows from

$$\cos\theta_r^c = r_f f\ cos\theta_Y + r_f f - 1, \tag{6.3}$$

where $f\,[-]$ is the fraction of the projected solid area that it is in contact with the liquid, r_f $[-]$ is the roughness ratio of the wet area, and θ_Y is Young's contact angle, see equation (6.1). Equations (6.2) and (6.3) have shown to provide a good approximation for the apparent contact angle of liquid drops sitting on top of many different micro-structures [94].

From the previous analysis, it can be concluded that increasing the roughness level can be employed to promote high apparent contact angles on an initially hydrophobic substrate. However, the actual wetting state which will occur, either Wenzel or Cassie-Baxter, is in principle unknown. The wetting state can be predicted from geometry of the surface features, following a free energy minimizing approach [95, 96]. This approach is briefly discussed in the next section. A simplified method for determining the actual wetting state can also be based on finding the location of the solid-liquid-vapour contact line, see figure 6.3(d) [97–99]. The later method is employed as a design criterion for the creation of a laser-generated superhydrophobic surface in section 6.5.

The particular shape of a microstructure determines whether the Cassie-Baxter wetting state will occur. The location of the solid-liquid-vapour contact line is given by the locations where Young's condition is met (locally), see figure 6.3(d). The local slope determines the position of the solid-liquid-vapour contact line [97–99].

If the surface consists of features with steep slopes, Young's condition is met at points close to the peaks of the surface features. In that case, air can be trapped beneath the liquid drop, see figure 6.3(d). Then a liquid drop in the Cassie–Baxter state has a limited contact with the solid. Solid-liquid contact fractions as low as 5 to 10% have been estimated for liquid drops in such a wetting state [100]. The easy roll-off and other properties of technological interest, like self-cleaning and anti-ice, have been attributed to the limited solid-liquid contact of water and a *superhydrophobic* surface (SHS) [100, 101]. Designing a surface microstructure with the desired water repellent properties then consists of finding the proper geometry of the surface features that minimizes the liquid-solid contact beneath the drop, ensuring that a Cassie-Baxter state can be achieved.

The Wenzel wetting state may be energetically favoured over the Cassie-Baxter state, even if a solid-liquid-vapour contact line can be formed around the peaks of the surface features. Based on free energy minimization approaches, an additional condition has been proposed to determine the stable wetting state [102],

$$cos\ \theta_C = \frac{r_f f - 1}{r - r_f f} \tag{6.4}$$

where θ_C is the so-called critical angle. Equation (6.4) is obtained by equating the apparent contact angle in equations (6.2) and (6.3), i.e. $\theta_W = \theta_{CB} = \theta_C$. When $\theta_C < \theta_Y$ the Cassie–Baxter state is energetically favoured, if $\theta_C > \theta_Y$ then the Wenzel state is energetically favoured [100]. In the following, this criterion is applied to different substrates to determine whether the Cassie–Baxter state is the favoured wetting state.

The determination of the required geometry leading to a Cassie–Baxter wetting state consists of finding the location of the solid-liquid-vapour contact line for a given microstructured substrate, from which the parameters r_f and f of equations (6.3) and (6.2) can be directly calculated. Equation (6.4) can be employed afterwards to find the stable wetting state (either Wenzel or Cassie-Baxter).

In the remainder of this chapter, a material removal strategy using short laser pulses is developed in order to create well–defined surface features that allows reaching the superhydrophobic state. The location of the solid-liquid-vapour interface is first calculated for different processing conditions, and equation (6.4) is afterwards applied to determine the stable wetting state.

6.4. Wetting properties of dual-scaled rough surfaces

Natural superhydrophobic surfaces often show a dual–scaled roughness, that is, the micrometric sized surface features show a superimposed sub-micrometric roughness level [103]. The presence of this *hierarchical* dual-scaled roughness is known to enhance the stability of the Cassie–Baxter wetting state [1, 100]. Laser microstructured surfaces also present multiple scaled roughness levels.

In general, an increased roughness tends to locate the solid–liquid–vapour contact line at a higher point closer to the peaks. As a result, the solid-liquid fraction f decreases. It follows from equation (6.4) that the stability of the Cassie–Baxter state of a substrate with a dual–scaled roughness also vary as a result of changes in the product $r_f \cdot f$. When considering rough substrates, r_f is, in general, a function of the location of the solid–liquid–vapour contact point. As a consequence, the product $r_f \cdot f$ is unknown. Since for rough substrates $r \gg r_f \cdot f$ [6], a good approximation of equation 6.4 is

$$\cos\theta_c \approx -1/r, \tag{6.5}$$

for real rough substrates [6]. According to this approximation, an increased roughness r reduces the critical angle, which promotes a stable Cassie–Baxter wetting state. The water repellent properties of a rough substrate can therefore be considered to increase, with respect to its equivalent smooth surface.

Unfortunately, there is not a direct method to predict the shape of the hierarchical structures obtained after laser processing, to establish a direct comparison between predicted and measured wetting properties of real surfaces. The contribution of the dual-scaled roughness, created after laser micromachining, to the stability of the Cassie–Baxter state is therefore unknown. However, an experimental approach can be employed to study the effect of the multiple-scaled roughness to the wetting properties of a laser-generated superhydrophobic surface. This is further discussed in the following.

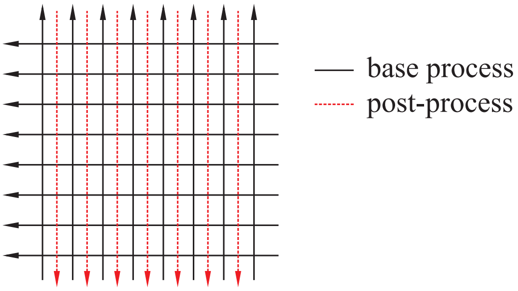

Figure 6.4.: Machining strategy for the creation of smooth peaks by post-processing. A base hatched pattern (black lines) is first applied to create a microstructured surface. A post-processing step (red dotted lines) is afterwards employed for smoothening the peaks of the created microstructure.

Creating multi–scaled surface features by picosecond laser pulses

Laser microstructuring allows modifying the roughness level of the peaks of a previously created microstructure. By properly adjusting the processing conditions, smoothened peaks could be created by applying a laser post-processing step. This step consists of displacing the laser tracks with respect to their original position, in order to process the peaks of the just generated microstructure. By increasing the energy per pulse to a sufficient level (peak fluence of 0.95 J/cm^2), material was removed from the peaks, and the resulting microstructure showed smooth peaks, see figure 6.5. In this manner, samples with and without a dual scaled roughness, sharing the same base microstructure, could be created.

In order to investigate the contribution of a dual-scaled roughness to the water repellent properties of a laser micromachined substrate, several samples were produced by the previously described technique. The resulting microstructures showed contrasting smooth or rough "peaks", as a function of the processing conditions, see figure 6.5. The samples were micromachined on a stainless steel substrate and subsequently coated by chemical vapour deposition with a thin layer of Perfluorinated OctylTrichloro-Silane (FOTS) hydrophobic coating, to achieve a superhydrophobic surface. FOTS coatings form an ideal monolayer on top of the created microstructure. As a consequence, the coating preserves the original shape of the surface profile. Details on the coating procedure can be found in paper B .

The wetting properties of the resulting samples were measured in terms of apparent contact angle and contact angle hysteresis. Table 6.1 shows the results. As discussed before, the sample showing a single-scaled roughness showed reduced water repellent properties. The sample with a hierarchical roughness showed both a high apparent contact angle and a low hysteresis.

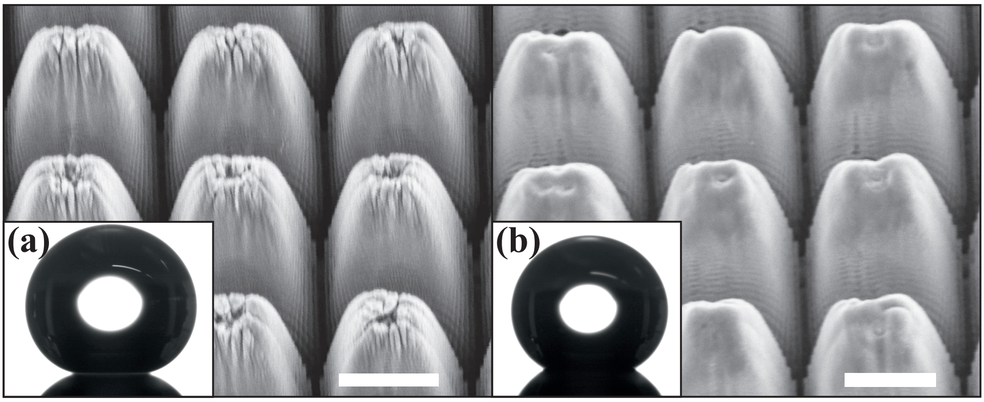

Figure 6.5.: Wetting properties of two laser micromachined substrates. Substrate (a) presents a dual scale roughness, and water contact angle of 163°. Substrate (b) has been postprocessed, resulting in smooth peaks and water contact angle of 151°. The length of the scale bar is 20 μm.

Table 6.1.: Wetting properties of laser generated microstructures with and without a dual–scaled roughness. Processing conditions: peak fluence 0.76 J/cm^2, laser pulses of <7 ps 515 nm, 80 laser cycles, track separation of 22 μm. Sample smooth was (post)processed with a peak fluence of 0.95 J/cm^2, 2 cycles.

Pattern	Measured APCA	Measured CAH
Hierarchical microstructure	163	$\approx$5
Smooth microstructure	151	>30

The contact angle hysteresis could not be determined for the sample showing a single–scaled roughness, as the solid-liquid-vapour contact line remained stationary *pinned* at a fixed location. These results support the idea that surfaces showing a hierarchical dual-scaled micro- & submicro-metric roughness can enhance the water repellent properties of a substrate [104–106].

6.5. Design of laser micromachined superhydrophobic surfaces

The design of a laser micromachined superhydrophic surface is based in this work on minimizing the total solid area in contact with the liquid, that is, reducing the parameter f of equation 6.3. In this manner, high APCA can be obtained. An additional requirement to achieve the superhydrophobic effect is to ensure that the CAH remains below 10°. Unfortunately, there is not a

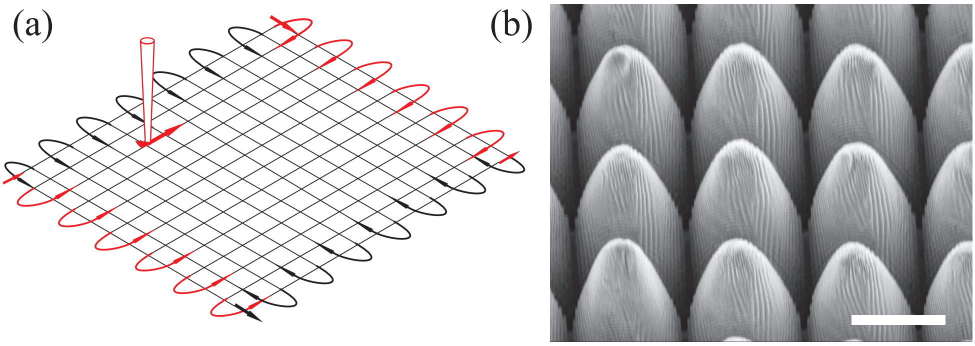

Figure 6.6.: (a) A laser beam guiding strategy for the creation of superhydrophobic surfaces. (b) SEM micrograph of the resulting surface microstructure. The length of the scale bar is 20 μm.

direct method to correlate the CAH and the geometry of a microstructure, see for example the discussion on this regard in reference [107]. Some of the available models for the prediction of the CAH require a precise knowledge of the wet area [96], which is in principle unknown for the laser-micromachined substrates. Alternative models rely on relatively complex numerical approaches, such as Lattice-Boltzmann simulations [108], which are difficult to combine with an arbitrary chosen surface profile, like those employed in this work. In the following, an alternative method for the design of a superhydrophobic surface, based on ensuring a stable Cassie-Baxter state, is developed. In any event, a Cassie-Baxter state has been traditionally related to low CAH values [109].

The hatched orthogonal pattern introduced in chapter 3 allows to generate suitable superhydrophobic surfaces, see figure 6.6(a). A surface topography consisting of micrometric sized features emerges as a result of the material removal process by this machining strategy, see figure 6.6(b). The slope of the surface features can be adjusted (i.e. chosen) by changing the separation between the laser tracks, and the number of times that the machining strategy is repeated (laser cycles). As a typical laser microstructuring process is based on material removal by laser ablation from a normal incident laser beam, the surface curvature that is obtained is up–concave. As reported by Tuteja et al, a top hydrophobic coating is then required for reaching the superhydrophobic effect [8].

The geometrical design parameters, namely the laser track separation and the number of laser cycles, have a direct influence on both r_f and f, as they modify the local surface slopes, and thus the location of solid-liquid-vapour interface. A systematic study and comparison of the wetting properties of the resulting surfaces is then possible by simply varying the hatch distances and the number of laser cycles.

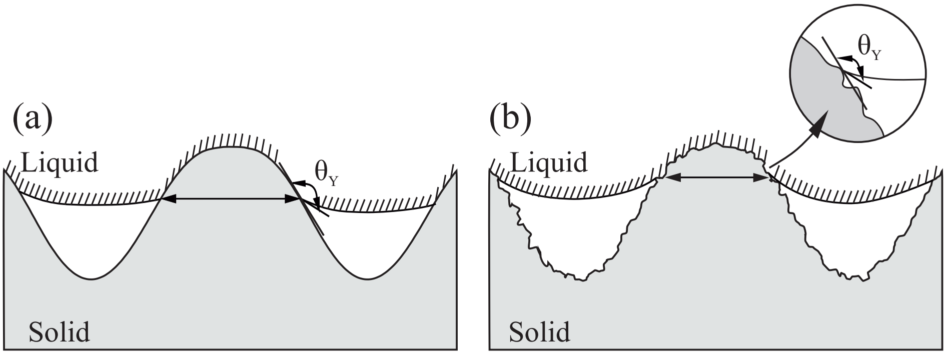

Figure 6.7.: Location of the liquid-vapour-solid contact line for a smooth ideal surface (a) and a surface showing a superimposed dual-scaled roughness (b).

The model for laser microstructuring introduced in chapter 3, can be employed to determine the required number of cycles and the track separation leading to a stable Cassie–Baxter state. The main steps of this procedure consist of:

1. Simulation/calculation of the surface topography, $H(x, y)$, for a predefined hatch distance, h_d, and a predefined number of laser cycles N_L, as described in section 3.5 in chapter 3.
2. Calculation of the solid-liquid-vapour contact line, by applying equation (6.6).
3. Calculation of r_f and f, and estimation of an apparent contact angle by equations (6.2) and (6.3).
4. Determination of the stable wetting state, by applying equation (6.4).

In the following, this geometrical design of a laser-generated superhydrophobic surface is further discussed. Different model surfaces are simulated on a first step, and their predicted wetting properties are subsequently calculated, to obtain the processing conditions leading to the superhydrophobic effect. As a criteria aimed at comparing and designing an optimized microstructure, ideal smooth surfaces are considered here.

Although the effect of a multi–scaled roughness is known to enhance the wetting repellent properties of a substrate [104–106], it is expected to have a limited effect on the optimization process of the microstructure. If a substrate is rough, see figure 6.7, the actual contact line will in principle fall anywhere *inside* the calculated wet perimeter of the equivalent smooth surface. As the optimization process consists of minimizing the wet perimeter, a rough structure will perform at least as good as the ideal smooth surface, allowing for a comparison between the different microstructures.

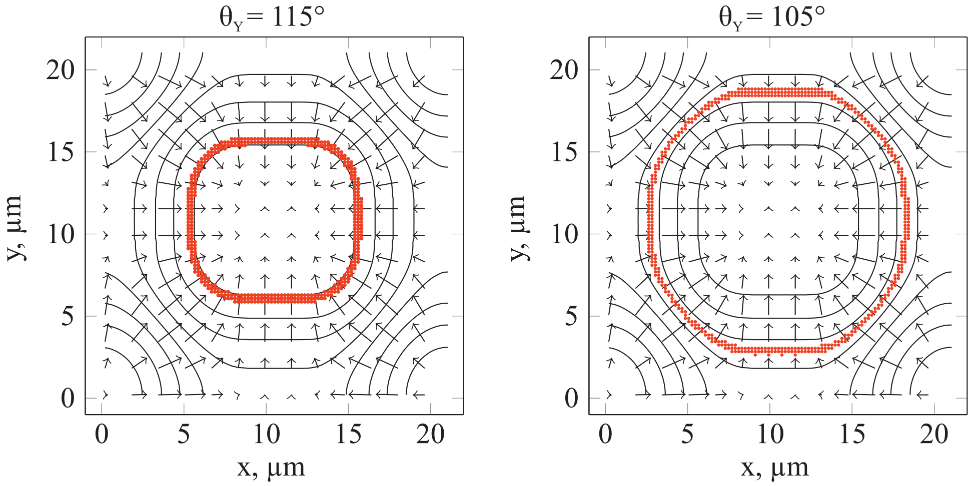

Figure 6.8.: Examples of contour plots showing the height (in isolines) of a microstructure and the gradient of the surface (arrows) of a unit cell. The calculation of the solid-liquid-vapour contact line is made for two substrates with changing surface chemistry, $\theta_Y = 115°$ and $105°$ (left and right, respectively). The red dotted line indicates the average height of the points where the condition given by equation (6.6) is met. Simulated processing conditions: 19 μm track separation, 50 laser cycles, peak incident fluence 0.43 J/cm^2, <7 ps laser pulses at 515 nm.

As the laser–generated structures created here show periodic profiles, they can be described well by the repetition of a "unit cell" (i.e. a single peak). The magnitude of the gradient of the unit cell determines the highest slope at each point on the surface. The wet perimeter can then be calculated as the closed curve that meets Young's condition around a peak of the unit cell, see equation (6.1) [90]. This calculation allows taking simultaneously into account the intrinsic wetting properties of the material, via θ_Y, and the geometry of the microstructure. The wet perimeter is then, based on simple geometrical considerations, given by

$$\arctan\left(\|\nabla H(x,y)\|\right) = \pi - \theta_Y, \tag{6.6}$$

where $H(x,y)$ corresponds to the height value of the calculated surface profile at the location (x,y). Equation (6.6) allows to calculate the location of the contact line for an arbitrary shaped smooth surface, as a function of θ_Y. The solution of this equation is not unique across the unit cell. The wet perimeter is defined here as the closed curve which is nearest to the peak of the microstructure.

Figure 6.8 shows the calculation of the wet perimeter for a given laser–generated structure, for two different θ_Y. The red dotted line indicates the

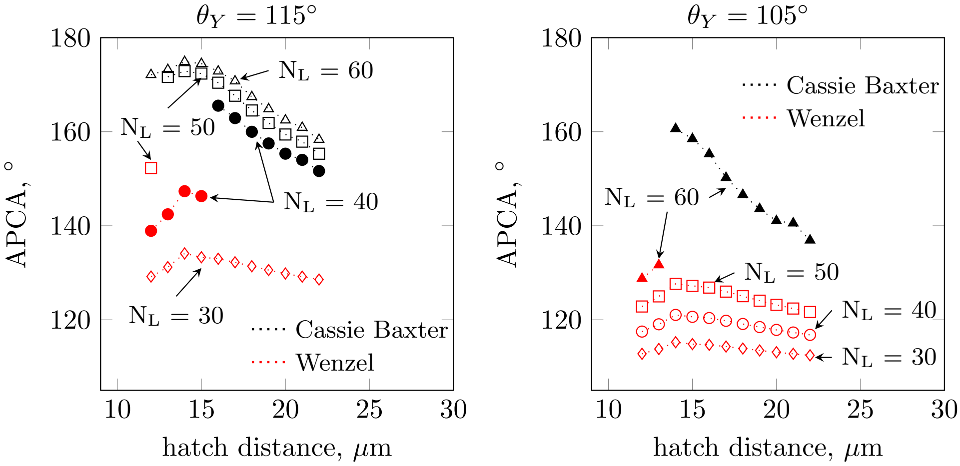

Figure 6.9.: Effect of substrate chemistry (θ_Y) and processing conditions (hatch distance and N_L) on the calculated apparent contact angle (APCA). Simulated processing conditions: hatch distance 12 to 22 μm, 30 to 60 laser cycles, peak incident fluence 0.43 J/cm^2, <7 ps laser pulses at 515 nm. Substrate is assumed to be stainless steel X5CrNi18-10, coated with two different materials with $\theta_Y = 115°$, left, and $\theta_Y = 105°$, right. Only the favoured wetting state, either Cassie Baxter or Wenzel is depicted.

average height of the points where equation (6.6) is met. It can be observed that the area inside the wet perimeter is larger for the less hydrophobic material (smaller θ_Y), figure 6.8 (right), when compared to the more hydrophobic material, figure 6.8 (left). As a consequence, the microstructure has a higher solid-liquid contact area, and thus, decreased water repellent properties (see section 6.3).

Once the location of the wet perimeter is known, the parameters r, r_f and f in equations (6.2) and (6.3) can be calculated to estimate the apparent contact angle. The calculation of the surface areas is based on a standard triangulation. Details on the numerical calculation of the parameters r, r_f and f are given in appendix III. A systematic quantitative comparison of the wetting properties of different surfaces can now be established, based on finding the substrate with a higher apparent contact angle, as the number of laser cycles N_L and the hatch distance h_d are varied. Equation (6.4) can be simultaneously employed to determine, for each processing conditions, the stable wetting state (Wenzel or Cassie-Baxter).

Figure 6.9 shows the calculated apparent contact angle plotted versus h_d and N_L, for two materials with different θ_Y of 115° and 105° respectively. The red and black dotted lines indicate, respectively, a stable Wenzel and Cassie-Baxter state. It can be observed that there is an optimal separation ($h_d \approx 15$ μm) between the laser tracks that leads to the highest apparent

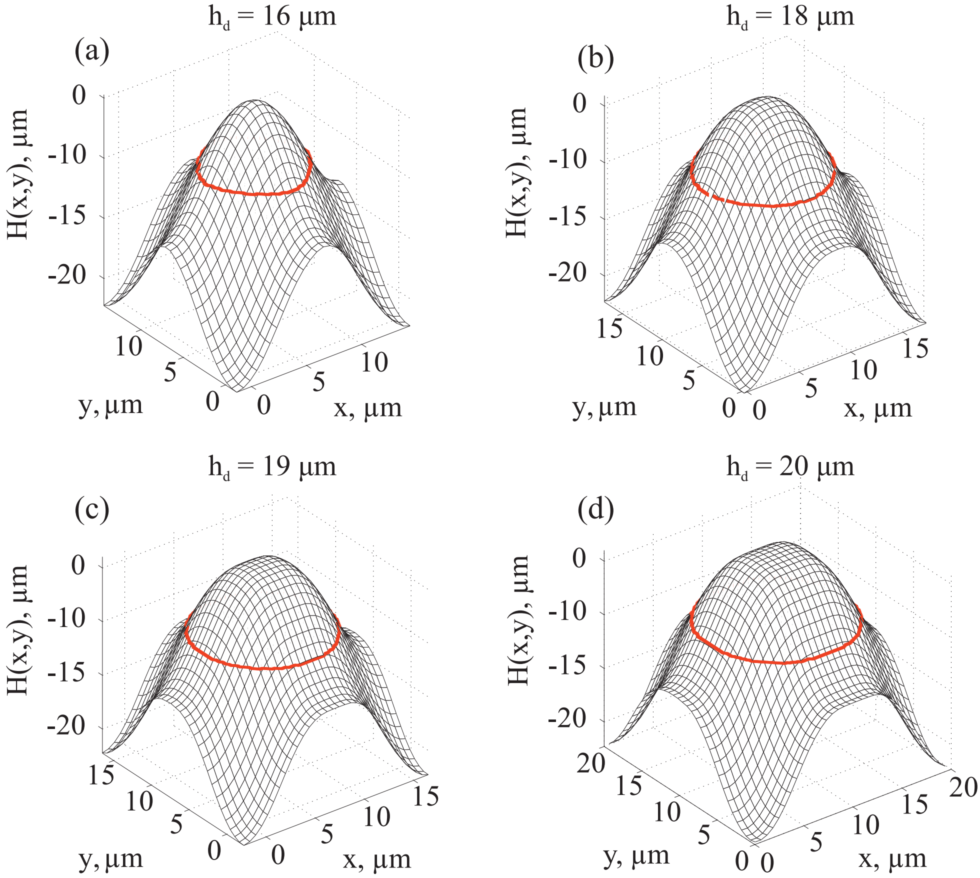

Figure 6.10.: Location of the solid–liquid–vapour contact line for samples with decreasing slope, which is achieved by increasing the separation h_d between the laser tracks respectively, from (a) to (d): h_d = 16, 18, 19 & 20 μm, 50 laser cycles, θ_Y=115°.

contact angle for a given number of laser cycles. The procedure can also be employed to determine the minimum number of cycles that are required to achieve a stable Cassie–Baxter state, for a given track separation.

Figure 6.10 qualitatively shows the effects of changing the hatch distance on the wet area. As h_d decreases, the solid-liquid area also decreases, leading to higher apparent contact angles. However, at a certain value, further decrease of the hatch distance results in a relatively strong laser processing (ablation) of the peaks, which reduces the local slopes. As a consequence, the criteria for the contact line calculation, equation (6.6), cannot be met anymore, and Wenzel is the stable wetting state. For a hydrophobic substrate with a θ_Y = 115°, it is found that a minimum of 40 laser cycles are necessary for reaching the superhydrophobic state, for a hatch distance between 15 and 20 μm. When a less hydrophobic material is employed as a top-coat, the number of required laser cycles increases to 60.

6.6. Experimental analysis

The laser processing parameters required to reach a stable superhydrophobic state have been determined by employing the model developed in chapter 3. In order to experimentally assess their water repellent properties, several trials patterns were created. The water repellent properties were measured and further discussed in papers A and B, for laser microstructured surfaces with hatch distances varying from 15 to 24 μm, number of layers ranging from 40 to 50 and for several materials with different wetting properties.

A superhydrophobic state, characterized by high apparent contact angles and low contact angle hysteresis, was achieved for selected samples. In addition, an extended experimental analysis was conducted in papers A and B, to confirm the potential use of a superhydrophobic surface as an ice repellent coating, under simulated environmental conditions in an ice chamber. Further, the contribution of a multiple scaled roughness to the water repellency of a superhydrophobic surface has been experimentally determined in section 6.4.

Paper A

Picosecond laser machined designed patterns with anti-ice effect

D. Arnaldo del Cerro, G.R.B.E. Römer and A.J. Huis in ‘t Veld.

In proceedings of the 11th International Symposium on Laser Precision Microfabrication (LPM 2010), 7 June 2010 - 10 June 2010 , Stuttgart.

URL: `http://purl.utwente.nl/publications/79815`

Paper B

Ultra short pulse laser generated surface textures for anti-ice applications in aviation

D. Arnaldo del Cerro, G.R.B.E. Römer, R.C.J. Sipkema, M.N.W. Groenendijk and A.J. Huis in ‘t Veld

In proceedings of the 28th International Congress on Applications of Lasers & Electro-Optics (ICALEO), 2-5 November 2009, Orlando.

URL: `http://purl.utwente.nl/publications/82890`

7 | Surface microstructuring for the Leidenfrost Effect

Droplets are able to levitate when deposited on a heated substrate. Laser-generated microstructures can be employed for modifying the vapour flow beneath the drop, to reduce the temperature that is required to observe the phenomena, or to create a force responsible for the movement of the drop following a desired direction. The mechanisms responsible for these effects have been investigated in papers C and D, respectively [1], [2].

7.1. The Leidenfrost effect

A liquid drop deposited over a surface, which is at a temperature sufficiently above the liquid saturation point, does not experience a sudden boiling. Instead, the droplet floats over a vapor layer that prevents the droplet from boiling. The vapor layer prevents contact between the liquid and the heated surface, providing an effective thermal isolation of the droplet. This phenomenon is known as the Leidenfrost effect, after Johann Gottlieb Leidenfrost, who discussed the effect in a paper in 1756 [79]. When in this situation, the droplet is not subjected to contact and friction with the solid and thus the so–called "Leidenfrost state" is often considered as a perfect superhydrophobic state. To reach such a state, the surface temperature has to be over a critical value known as the Leidenfrost point (LFP) [79], which has been often related and identified to the onset temperature for film boiling [80, 110].

---

[1] Reproduced in part with permission from Arnaldo del Cerro, D. and Marín, Á.G. and Römer, G.R.B.E. and Pathiraj, B. and Lohse, D. and Huis in 't Veld, A.J. *Leidenfrost Point Reduction on Micropatterned Metallic Surfaces*, Langmuir 28(42):15106-15110, 2012. Copyright 2012 American Chemical Society.

[2] Reproduced in part with permission from Marín, Á.G. and Arnaldo del Cerro D. and Römer G.R.B.E. and Pathiraj, B. and Huis in 't Veld A.J. and Lohse D. *Capillary droplets on Leidenfrost micro-ratchets*, Physics of Fluids. 2012;24(12):122001-10. Copyright 2012 American Institute of Physics.

The Leidenfrost effect is of relevance for practical applications. On the one hand, the effect has a clear detrimental influence on heat transfer, and therefore has to be taken into account when using liquids to cool heated surfaces. In this context, extensive theoretical & experimental research has been performed in order to make predictions on the LFP, with the attendant difficulties due to the amount of parameters involved. Experimental studies were mainly focused on methods to increase the LFP of a system, which would give a wider dynamic range for cooling applications. Several authors have reported that the roughness of the surface substantially increases the LFP [80–82]. Traditionally, this was achieved by etching or sand blasting the surface, giving it a random micro or nano–roughness. More recently, Kim et al. have studied the effect of sparse surface micro–defects on the LFP and the stability of the Leidenfrost state [83].

On the other hand, the effect can be interesting to study, as it provides a perfect hydrophobic state, lacking any contact with the surface. For this reason, the droplet moves freely following the slope of the surface until it encounters a geometrical obstacle. Recent studies with designed micro–patterned surfaces were able to control the movement of the Leidenfrost drop [87, 111–113]. Other studies have used the Leidenfrost effect to reduce the drag of a heated metallic object immersed in a liquid, achieving a reduction of drag coefficients up to 40% [114]. Another potential application would be to use the effect as a controlled droplet evaporation technique for evaporating complex droplets e.g. to produce capsules on–demand [115]. For such applications it is therefore interesting to find ways to reduce the LFP and be able to reach such a state by using the least energy possible.

7.2. Surface microstructuring for decreasing the Leidenfrost Point

Surface microstructuring has been shown to play a role in either stabilization [84, 116], or destabilization [83, 117] of the vapour film sustaining a ‘‘Leidenfrost drop’’. Kim et al [83] reported a patterned surface which disturbed the formation of the vapour film, promoting the nucleation of small bubbles at the sharp edges of the microstructure, leading to higher LFP. Recently, Adera et al [84] reported a transition to a non-wetting state of water droplets sitting on top of hydrophilic microtextured surfaces, at temperatures slightly above the saturation point, far below the LFP for the equivalent smooth substrate.

Hence, the formation of a vapour film capable of levitating a liquid drop can be promoted or disturbed by the presence of a microstructure. A microstructure provides with surface cavities for the heterogeneous nucleation of vapour bubbles. Bernardin and Mudawar [118] proposed a cavity activation model

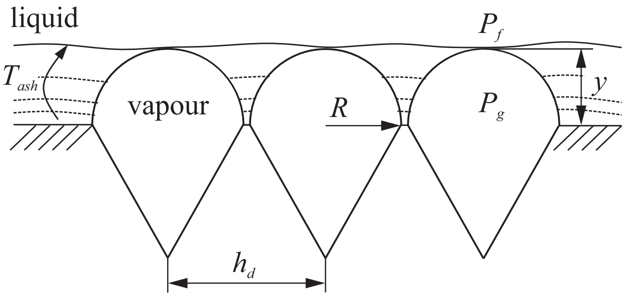

Figure 7.1.: Geometrical properties of surface cavities which are able to promote the nucleation of a vapour bubble. A vapour bubble of radius R nucleates on a surface cavity of the same radius, when the available overheat, T_{ash}, reaches a thickness $y = R$. The separation between active cavities, h_d, can be selected to study the formation of a stable vapour film below the liquid droplet.

capable of predicting the LFP of rough substrates. This model can be employed to calculate the size of the cavities that are available for the nucleation of vapour bubbles after a drop is in contact with a heated surface.

In the following, see section 7.2.1, this model is briefly summarized, and subsequently employed to calculate the required size of the surface features that can act as nucleation sites. Next, section 7.3, laser micromachining is discussed as a tool for the creation of such surface cavities with sizes which can promote the formation of vapour bubbles. Then, paper C includes an extended analysis on the effect of laser microstructured surfaces on the LFP.

7.2.1. Film boiling and bubble nucleation on rough substrates

The first step in the formation of a vapour film on a rough substrate consists of the heterogeneous nucleation of vapour bubbles in cavities of an adequate size. In the model of Bernardin and Mudawar [118], the equivalent cavity radius that is required for the nucleation of a vapor bubble, at a given temperature, is first calculated. The temperature that is required for the heterogeneous nucleation of a vapor bubble, is that providing sufficient gas pressure P_g to overcome the Laplace pressure, see figure 7.1. The pressure drop across the liquid–vapour interface is given by the Laplace equation,

$$P_g - P_f = \frac{2\gamma_L}{R_d}. \tag{7.1}$$

where γ_L is the surface tension of the liquid, R_d is the radius of the vapour bubble, P_g is the pressure in the vapour bubble and P_f is the pressure in the liquid. The temperature required for the heterogeneous nucleation of a bubble of radius R can be calculated by combining equation (7.1) with the

Clausius–Clapeyron relation along the saturation line [119],

$$\int_{P_f}^{P_g} dP = \int_{T_s}^{T_s+\Delta T_s} \frac{\lambda}{T\Delta v_{fg}}\, dT. \tag{7.2}$$

Solving this equation for T yields the required temperature for the heterogeneous nucleation of a vapour bubble,

$$T_{het} = T_s \exp\left(\frac{2\gamma_L \Delta v_{fg}}{R_d \lambda}\right), \tag{7.3}$$

where Δv_{fg} is the change of the specific volume from the liquid to the vapour phase, T_s is the saturation temperature and λ is the latent heat of vaporization.

Next, the temporal temperature evolution of the liquid in contact with a solid substrate can be described as a heat transfer problem between two semi–infinite bodies [120]. The temperature of the liquid will increase from the instant it is brought in contact with the surface until the instant at which a vapour bubble can be formed. The available superheat at a given time, T_{ash}, can be expressed as

$$T_{ash} = T_i + (T_f - T_i)\,\mathrm{erf}\left(\frac{y}{2\sqrt{D_f t}}\right) \tag{7.4}$$

where T_f is the temperature of the liquid, y is the distance normal to the solid surface and D_f is the thermal diffusivity of the liquid and $\mathrm{erf}(\cdot)$ is the error function. The temperature at the interface, T_i, is given by the solution to the one dimensional energy equation with semi–infinite body boundary conditions [120],

$$T_i = \frac{T_s\sqrt{(\kappa\rho c_p)_s} + T_f\sqrt{(\kappa\rho c_p)_f}}{\sqrt{(\kappa\rho c_p)_s} + \sqrt{(\kappa\rho c_p)_f}}, \tag{7.5}$$

where κ is the thermal conductivity, ρ is the density and c_p is the specific heat at constant pressure. The subindexes s and f indicate the properties of respectively the solid and the liquid.

When an overheated liquid layer reaches a thickness y with a temperature equal or above T_{het}, heterogeneous nucleation of a vapour bubble occurs. This situation can be mathematically described by equating equations (7.4) and (7.3), for a liquid layer of thickness y, when it equals to the radius R of the bubble, see figure 7.1. It is therefore implicitly assumed that a spherical bubble of radius R will nucleate at a surface cavity of the same radius, see figure 7.1.

The two roots of the equality $T_{het} = T_{ash}$, yield the minimum and maximum radii of surface cavities which are ‘‘active’’ for vapour nucleation at a specific

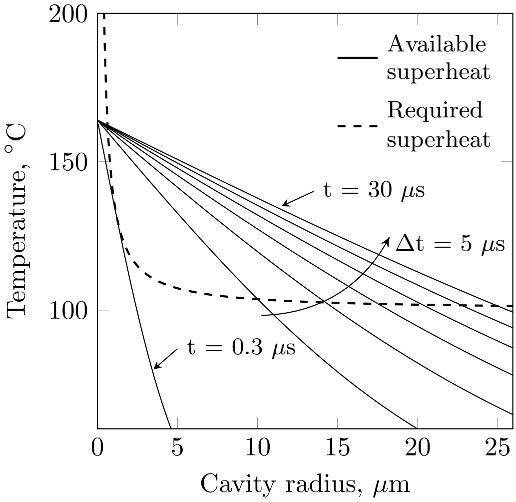

Figure 7.2.: Temperature evolution of a water layer on a stainless steel substrate at a surface temperature T_i=145°C during the first 50μs. When the available superheat (solid lines) exceeds the required superheat (dashed line), heterogeneous nucleation of vapour bubbles within a given range of radii occurs.

time. To illustrate this numerically, figure 7.2 shows the temperature evolution of the overheated liquid layer up to 50 μs after a water drop is brought in contact with a stainless steel surface. The later is assumed to be at a temperature T_i=145 °C. It can be concluded from this graph that shortly after the drop is brought in contact with the solid, any micrometric surface cavities with sizes in the range of 1 to 25 μm, become activated.

Although these cavity dimensions may promote the formation of large vapour bubbles, the formation of a vapour film capable of sustaining a liquid droplet requires additional steps. Once the bubbles nucleate, they have to grow and merge to form a film capable of levitating the droplet. If the cavity size distribution is even across a surface, and bubbles nucleate at a time (same speed), the formation of a stable vapour film can be promoted. Sparse defects of different sizes would have the opposite effect, as pointed out by Kim et al. [83].

7.3. Design of laser micromachined microstructures for the Leidenfrost effect

The laser micromachining process allows for a quantitative study of the effects of a changing geometry on the temperature that is required to reach the Leidenfrost point. This process can be employed to create ordered networks of cavities with sizes which are adequate for the heterogeneous nucleation of

Table 7.1.: Geometric dimensions and processing conditions of the metallic microstructures, micro–pillars (p) and micro–holes (h); maximum depth, μm; center to center spacing, μm; average energy per pulse (E_p), μJ and pulse to pulse spatial overlap, %.

Structure	Depth, μm	h_d, μm	Ep, μJ	Overlap, %
h1	3	17	0.35	0
h2	6	17	0.35	0
h3	9	17	0.35	0
p1	10	17	0.35	96
p2	18	17	0.35	96
p3	26	17	0.35	96

vapour bubbles. In order to study the temperature that is required to reach the Leidenfrost state, two different patterns were machined: a hatched pattern, see figure 7.3(left), and a blind hole array, see figure 7.3(right).

The laser beam was focused on the surface and scanned across different areas following two different machining strategies. First, the regular orthogonal hatched pattern previously introduced in chapters 1 and 3 was used for creating a pillar-like structure, see figure 7.3(left). The followed procedure was the same as discussed in previous chapters.

Next, a blind hole array was created by increasing the scanning speed while decreasing the laser repetition rate. This allowed for the spatial separation of the laser pulses. A unidirectional hatched pattern was employed in this case. The separation between the scanned lines, h_d, was selected to match the distance between the laser pulses along a track. As a result, a regular array of blind holes emerges from the material removal process, see figure 7.3(right). Both processes were repeated a number of cycles, to increase the depth of the resulting microstructures. The processing conditions and geometry of the resulting microstructures are summarized in table 7.1.

7.4. Experimental analysis

In order to investigate the effects of the created surface microstructures on the formation and stabilization of a vapour film, the temperature dependence of evaporation time and droplet shape was experimentally studied in paper C. The temperature increment, relative to the boiling point, required to reach the LFP was in addition investigated, for both the micro-pillar and the blind-hole arrays.

A hybrid hydrophobic state was identified, at much lower temperatures than the classical Leidenfrost temperature, in which the contact of the droplets with

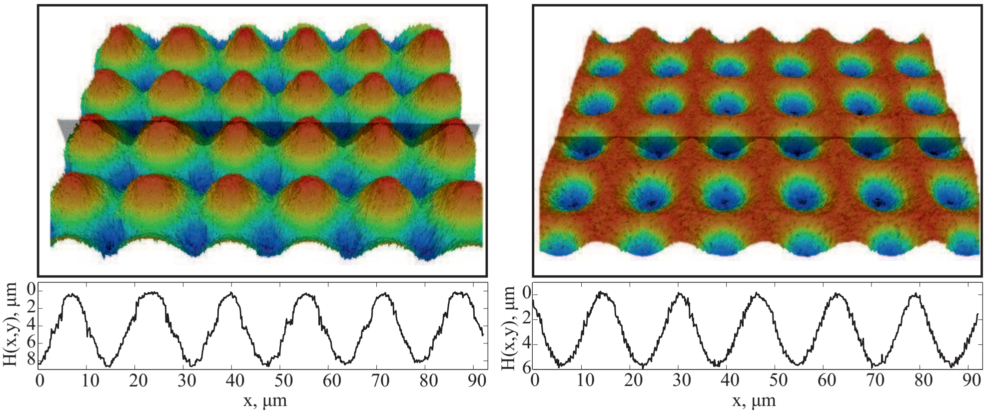

Figure 7.3.: CLSM images of a pillar-like structure (left top) and a hole array structure (right top) with their respective cross section profiles (bottom), corresponding to samples p2 and h2 listed in table 7.1.

the solid was substantially reduced. In such state, liquid drops vaporized at a fixed location, without drifting along the surface in frictionless motion. The reasons for the variation of the LFP on the microstructures are qualitatively and quantitatively discussed in paper C employing a simple semi-empirical model.

Paper C

Leidenfrost Point Reduction on Micropatterned Metallic Surfaces

D. Arnaldo del Cerro, Á. Gómez Marín, G.R.B.E. Römer, B. Pathiraj, D. Lohse and A.J. Huis in ‘t Veld

Langmuir 28(42): 15106-15110, 2012

URL: `http://dx.doi.org/10.1021/la302181f`

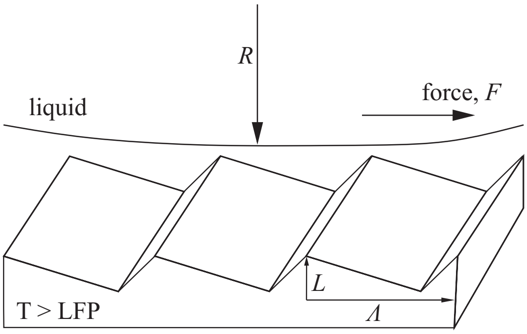

Figure 7.4.: A self–propelled Leidenfrost drop on a heated ratcheted surface with ratchet height L and periodicity Λ.

7.5. Self–propelled capillary drops on asymmetric surface microstructures

A liquid drop sitting on an asymmetric ratcheted structure at a temperature above the LFP moves in a preferential direction, which is given by the orientation of the ratchets, see figure 7.4. In literature, different mechanisms have been proposed for the thrust exerted on a Leidenfrost drop on a heated ratchet. These models predict different scaling laws for the force driving the motion, as a function of the size of the drop.

Surface microstructuring by picosecond laser pulses allows creating microstructures that can be employed for the study of this phenomenon, extending current analysis to include small capillary droplets. As such, laser microstructuring can help falsifying or confirming the proposed mechanism.

The vapour flow produced when a liquid drop approaches a surface at a temperature above the LFP has been proposed to follow a preferred direction, exerting drag on a Leidenfrost drop. As a result, the levitating drop flows following a predetermined direction, which is dictated by the geometry of the microstructure [87, 88]. Lagubeau et al. [87] proposed a simple mechanism based on vapor flow rectification and mass conservation, yielding a scaling law for the force F and the radius of the drop R_d: $F \sim R_d^{3/2}$. Shortly after, new observations brought a more sophisticated mechanism: the vapor flow is responsible for the thrust, but due to the viscous drag exerted over the surface of the drop, and not as a direct consequence of the momentum conservation [88]. As a result, in this case the force F scales with the volume of the drop, and therefore $F \sim R_d^3$.

Thermal creep has also been proposed as an alternative mechanism for the drop motion by Würger [121]. According to this model, the asymmetric surface produces a net horizontal component of the creep velocity [122]. That is, temperature gradients induce vapour movement along the solid–gas interface, which propels the Leidenfrost drop. Based on this approach, the force F scales as $F \sim R_d^{1.2}$ [121].

Laser microstructuring can be employed to create ratcheted microstructures with varying geometrical properties (height L and periodicity Λ), see figure 7.4, for the study of the mechanisms propelling a Leidenfrost drop. This approach is based on the development of a simple scaling law, extending the analysis performed by Dupeaux et al. [88] to include *capillary drops.* A capillary drop is characterized by a radius which is smaller than the *capillary length* c_l, given by $c_l = \sqrt{\gamma_L/\rho_l g}$, where γ_L and ρ_l are, respectively the surface tension and the density of the liquid. The radius of a water capillary drop is of about 1.5 mm. Capillary drops can be propelled by ratcheted substrates of micrometric size.

Viscous drag flow as potential mechanism

In paper D, the model developed by Dupeux et al. [88] is further elaborated to obtain scaling laws for the force exerted on drops of various diameters, including the size of capillary drops. The idea behind the *viscous mechanism* is the following: The vapor emanating from the bottom of the droplet flows preferentially into the deeper parts of a ratchet, giving the droplet a net shear according to a preferential direction, which is then given by the ratchet orientation. If the pressure below the drop results from the drop's weight, the force $F^{(s)}$ exerted on the drop is shown in paper D to be proportional to the squared radius of the drop as

$$F^{(s)} \sim \rho_l H_{drop} g R_d^2 \theta, \tag{7.6}$$

where H_{drop} is the height of the drop and $\theta = \arctan(L/\Lambda)$, with L and Λ being the height and periodicity of the ratchet, respectively (see figure 7.4). In the case of a capillary drop, the capillary pressure, which is proportional to $P \sim \gamma/R_d$, becomes stronger than the pressure exerted by the weight of the droplet [123]. In this case, the thrust $F^{(c)}$ that is exerted on a capillary drop is shown in paper D to scale as

$$F^{(c)} \sim \gamma \frac{c_l^2}{R_d} \theta \tag{7.7}$$

Hence, in contrast with the result obtained for a large drop, the thrust which is exerted on a capillary drop is shown to be inversely proportional

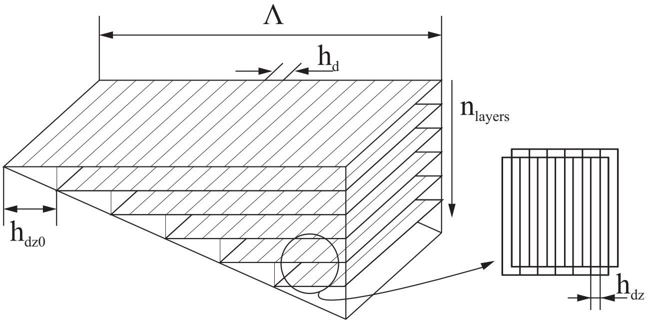

Figure 7.5.: A layer by layer machining strategy for the creation of a micro–ratchet with main geometrical parameters: ratchet periodicity, Λ, number of layers, n_{layers}, laser track separation within a layer, h_d, layer to layer offset, h_{dz0} and layer to layer relative vertical displacement, h_{dz}.

to its radius. The relation between the pressure and the aspect ratio θ is directly proportional in both cases.

The creation of microratchets which are capable of propelling both capillary and larger heavy drops allows for an experimental investigation of the mechanisms driving the propulsion of Leidenfrost drops.

7.6. Design of laser-generated micrometric ratchets

As can be concluded from the previous section, studying the motion of a capillary drop over a heated microstructured substrate requires creating surface features with an adequate geometry, in terms of the geometrical parameters Λ and L, with sizes in the order or smaller than several tens of micrometers. In order to propel capillary drops, the periodicity of the ratchets Λ has to be sufficiently smaller than the diameter of the drop, while their aspect ratio L/Λ should provide a measurable thrust, according to equation (7.7). The model developed in the first part of this thesis was employed to design and create a suitable machining strategy that allows achieving a microstructure with an adequate geometry for propelling (capillary) drops.

Ratchets can be achieved by a number of micromachining strategies. A relatively simple layer by layer strategy was selected. That is, each layer consisted of a unidirectional hatched pattern, containing several parallel laser tracks, which removed thin slices of material. The main geometrical parameters of this machining strategy are summarized in figure 7.5, and further discussed below.

The parameters defined in figure 7.5 have to be considered simultaneously, as the final geometry results of their combined effects. The

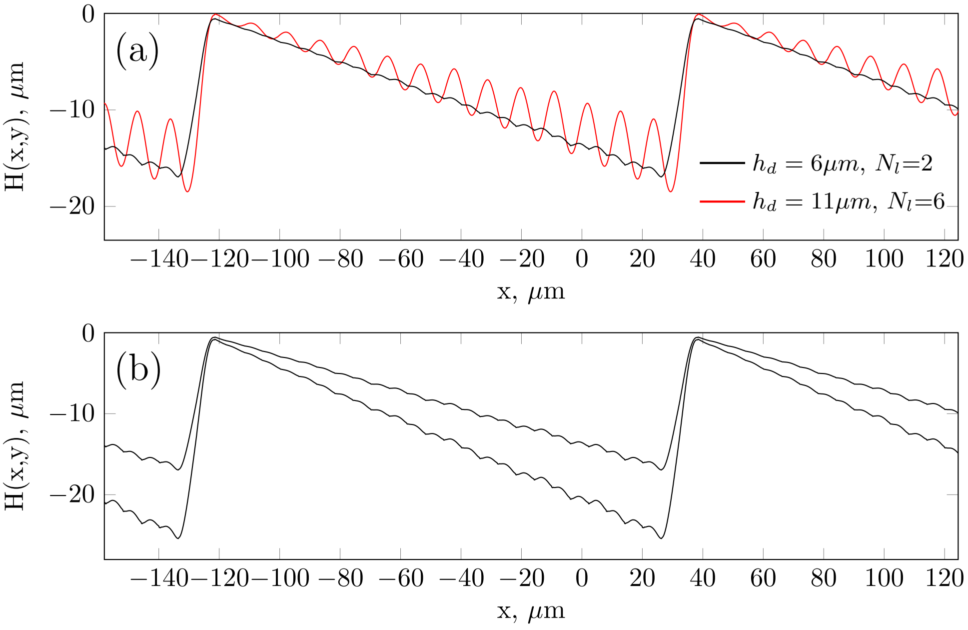

Figure 7.6.: Cross-sections of simulated surface profiles obtained after the following processing conditions: peak incident fluence 0.43 J/cm^2, laser pulses of <7 ps 515 nm, substrate is stainless steel (X5CrNi18-10). Pattern geometry (a) (red line): hatch distance 6 μm, 2 laser cycles, (black line) hatch distance of 11 μm, 6 laser cycles. Pattern geometry (b) hatch distance 6 μm, 2 and 3 laser cycles.

individual contribution of each parameter is discussed below, employing the model developed in the first part of this work to illustrate the resulting geometry. The final selection of processing parameters is addressed in the next section.

1. The track distance, h_d, determines the ablated thickness per layer and has an effect on the final roughness level of the ratchets. The parallel laser tracks within a layer should be close enough to obtained a reduced roughness. However, a too small value of h_d results into increased processing time and thicker slices of removed material per laser cycle, which in turn reduces the accuracy of the material removal process. Figure 7.6(a) shows simulation results illustrating the effects of changing the track separation on the geometry of the final microstructure. Here, the number of laser cycles have been accordingly adjusted to obtained structures with a comparable aspect ratio. It can be observed that the simulated microstructure with the smaller track separation has, in addition, a reduced surface

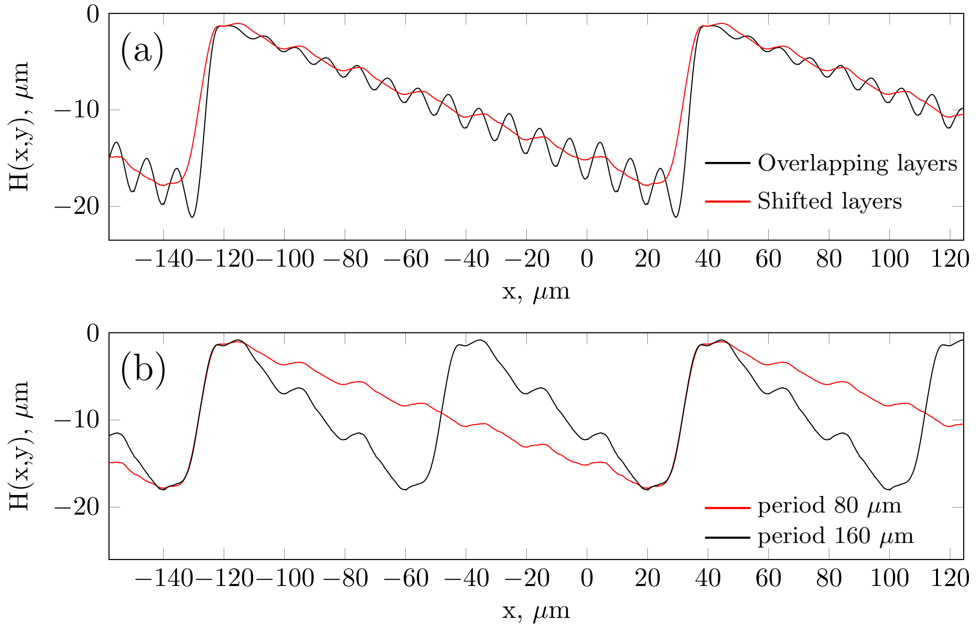

Figure 7.7.: Cross-sections of simulated surface profiles of ratchets machined with overlapping and shifted layers (a) and changing periodicity (b). Simulated processing conditions: peak incident fluence 0.43 J/cm^2, laser pulses of <7 ps 515 nm, substrate is stainless steel (X5CrNi18-10). Pattern geometry (a) (red line): hatched at hd 10 μm, layer to layer shifting hd_z 5 μm, number of laser cycles 6, (black line) hatched at 10 μm, layer to layer shifting hd_z 0 μm, number of laser cycles 6. Pattern geometry (b): hatched at hd 10 μm, layer to layer shifting hd_z 5 μm, number of laser cycles 6, surface profiles with changing periodicity Λ of 160 and 80 μm, red and black solid lines, respectively.

roughness.

2. Number of cycles. Increasing the number of times a selected strategy is repeated allows increasing the aspect ratio of the ratchets. The latter is known to affect the force exerted on the drops, see equations (7.6) and (7.7). Figure 7.6(b) shows the increased aspect ratio of two ratchets machined with 3 and 6 laser cycles, respectively.

3. Layer to layer relative displacement, h_{dz}. The relative position between layers determines the vertical overlap between tracks of consecutive layers. If the tracks from consecutive layers fall exactly on top of each other, the resulting surface roughness is the largest. Changing the relative orientation of the tracks between layers allows

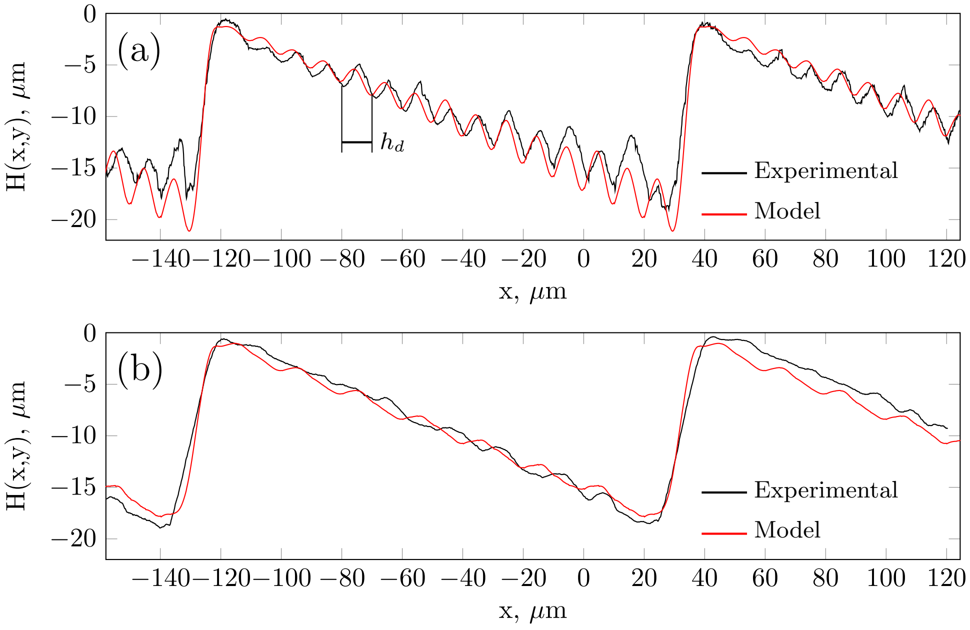

Figure 7.8.: Cross-sections of simulated as well as measured surface profiles of ratchets machined with overlapping (a) and shifted layers (b). Simulated processing conditions: peak incident fluence 0.43 J/cm^2, laser pulses of <7 ps 515 nm, substrate is stainless steel (X5CrNi18-10). Pattern geometry (a): hatched at hd 10 μm, layer to layer shifting hd_z 0 μm, number of laser cycles 6. Pattern geometry (b): hatched at hd 10 μm, layer to layer shifting hd_z 5 μm, number of laser cycles 6.

decreasing the roughness. Figure 7.7(a) shows a micro-ratchet machined with 100% vertical overlap between laser tracks, h_{dz}=0, from consecutive layers (solid black line), and the effects of displacing the laser tracks 50%, h_{dz}=$h_d/2$ (solid red line). It can be observed that the resulting roughness significantly decreases when displacing the laser tracks, while the number of layers and laser tracks per layer remains constant. Figures 7.8(a) and (b) show an additional comparison between simulated and measured surface profiles, for $h_{dz} = 0$ (a), and for $h_{dz} = h_d/2$, (b).

4. Periodicity, Λ. As discussed before, a sufficiently small periodicity allows propelling small capillary drops. A fixed periodicity of 150 μm was selected as it was experimentally found to provide a sufficient thrust for capillary droplets of diameter of about 1.5 mm, see paper D.

5. Number of layers per ratchet, N_L. This parameter is given by the

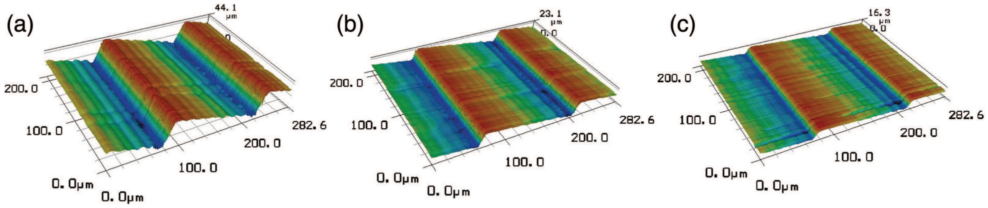

Figure 7.9.: CLSM micrographs of the laser micromachined ratchets on a stainless steel (X5CrNi18-10) substrate. Processing conditions: peak incident fluence 0.43 J/cm^2, laser pulses of <7 ps, 515 nm. Pattern geometry: hatched at 10 μm, layer to layer shifting hd_z 5 μm. Number of laser cycles: 9, 6 and 3, (a), (b) and (c), respectively.

periodicity and the track distance as $N_L = \Lambda/h_d$.

6. Layer to layer offset, h_{dz0}. This parameter is given by the periodicity and the number of layers as $h_{dz0} = \Lambda/N_L$.

Parameter selection

The selected machining strategy consisted of employing successive layers which were vertically displaced 50%, to prevent the vertical overlap of the laser tracks from successive layers, and reducing thus the resulting roughness, see figure 7.7. The hatched distance h_d was fixed at 10 μm. The periodicity of the ratchets was selected to be 150 μm, which is an order of magnitude below the typical size of a capillary drop. The number of laser cycles was selected to be 3, 6 and 9, which resulted in ratchets with increasing aspect ratios, see figure 7.9. This machining strategy allows obtaining micrometric ratchets, which were experimentally shown to propel capillary drops with increasing force F_R as the aspect ratio increases, see paper D.

Table 7.2.: Geometrical characteristics of the laser micromachined ratchets on a stainless steel (X5CrNi18-10) substrate. Processing conditions: peak incident fluence 0.43 J/cm^2, laser pulses of <7 ps, 515 nm. Pattern geometry: hatched at 10 μm, layer to layer shifting hd_z 5 μm. Number of laser cycles: 9, 6 and 3, respectively.

Pattern	Average height, L μm	Average period Λ, μm	Aspect ratio L/Λ
A	34	144	0.24
B	17	145	0.12
C	10	144	0.07

7.7. Experimental analysis

Ratchets with increasing aspect ratios were machined on a stainless steel X5CrNi18-10 substrate by the procedure described in the previous section. By properly adjusting the laser conditions, three samples with increasing aspect ratios with a fixed periodicity were obtained, see figure 7.9. The surface profile of the resulting microstructures was measured by CLSM, and the main geometrical characteristics are listed in table 7.2.

Paper D includes a study of the motion of droplets of different radii in terms of speed and acceleration. High speed camera recordings of the trajectory of the droplets along a ratchet were performed at increasing temperatures, at typical recording speeds of 1000 fps, on ratchets of at least 4 cm long. The recorded images were processed to obtain data on position of the drop and time, allowing for a direct calculation of velocity and acceleration. Next, the force exerted on the droplets was calculated.

The experimental data presented in paper D support the viscous mechanism as the main contributor to the droplet propulsion on the Leidenfrost ratchets. Laser micromachining with picosecond pulses has therefore been shown to be able to reproduce adequate geometries for the study of the Leidenfrost effect on capillary droplets.

Paper D

Capillary droplets on Leidenfrost micro-ratchets

Á. Gómez Marín, D. Arnaldo del Cerro, G.R.B.E. Römer, B. Pathiraj, A.J. Huis in ‘t Veld and D. Lohse

Physics of Fluids 24(12): 122001-122010, 2012

URL: `http://dx.doi.org/10.1063/1.4768813`

8 Conclusions & Future work

8.1. Conclusions

Laser micromachining of metals with picosecond laser pulses has been shown to be an adequate tool for the creation of microstructures with applications in microfluidics. The material removal process by short laser pulses allows adjusting key geometrical parameters of a microstructure, which permits the investigation of some of the mechanisms responsible for the fluidic functionalities.

Part I. Surface micro-structuring with short laser pulses

With respect to the first research question, ‘‘is it possible to predict, for given processing conditions, the resulting geometry of the surface of a substrate?’’, stated in chapter 1, the model developed in chapter 3 allows the calculation of the surface profile obtained after given laser processing conditions. The accuracy of the procedure suffices for the prediction of variations in the resulting microstructure, when changes in the machining strategy are introduced, see section 4.6.

The range of application of the model was experimentally determined, for a selected substrate (stainless steel X5CrNi18-10) and a picosecond laser source. First, it was shown that the average ablated depth per pulse remains constant at typical values around 20 nm/pulse, for a certain number of applied pulses, of about 500, at moderate fluence levels, below 0.8 J/cm^2. This linearity, together with the assumption of negligible effects caused by residual energy accumulation, allowed the simulation of a multi-pulsed process and, as a result, the calculation of surface profiles given the processing conditions.

Next, an extended experimental analysis revealed the applicability of the model for the simulation of microstructures, obtained after processing with partially overlapping laser pulses, which were arranged according to a predefined machining strategy. The model was shown to accurately reproduce surface microstructures with a maximum depth of about 20 μm, with a maximum relative error of 8%, when compared to experimental values. The experimental data also showed that the multi-pulsed material removal process is linear with the number of applied laser pulses even at a pulse repetition rate of 400 kHz.

As demonstrated in chapter 4, processing with moderate fluence levels leads to surface profiles with a *controllable* geometry. That is, because of the relatively thin layers that are removed by a laser pulse at these fluence levels, the surface profile can be controlled with a high accuracy. This has been achieved by properly adjusting the micromachining strategy, e.g., by changing parameters such as the number of applied laser cycles and the laser track separation.

Part II. Laser-generated functional microstructures

With respect to the second research question, “what knowledge can be gained regarding the interaction of a fluid with a microstructured surface obtained by laser processing?”, stated in chapter 1, several fluidic functionalities have been related to the geometry of the created microstructures. The geometry which is required to gain a functionality was first investigated. Then, the model developed in chapter 3 was employed to find a suitable laser machining strategy leading to the functional surface. Next, the mechanisms leading to these functionalities have been studied and clarified.

In chapter 6 and in papers A and B, it has been shown that a laser-generated superhydrophobic surface can be created by combining certain laser processing conditions and the application of a suitable hydrophobic coating. It was shown that a minimum of 50 laser cycles were required to achieve the superhydrophobic effect, when a hatched pattern with a track separation varying from 14 to 24 µm was employed. Further, a laser-generated superhydrophobic surface was shown to successfully act as a functional anti-ice substrate under certain conditions, providing that sufficient water repellent functionality was achieved.

In chapter 7, as well as in paper C, an ordered network of laser-generated microcavities, with radii varying between 1 and 25 μm, was shown to decrease the temperature required to achieve the Leidenfrost effect. Further, the viscous mechanism for the motion of a Leidenfrost drop on a heated microratchet was supported experimentally in chapter 7 and paper D, by employing laser-generated microratchets with periodicities of about 150 μm and aspect ratios varying from 0.07 to 0.24.

8.2. Future work

Part I. Surface micro-structuring with short laser pulses

The model introduced in this work relies on a calibration procedure for the calculation of an ablated profile. It would require further research into the mechanisms leading to material removal by laser ablation in order to calculate ablated profiles based on the laser pulse intensity profile and material properties. Current combined modelling approaches, based on e.g. the two-temperature model and molecular dynamic simulations, as introduced in chapter 2, give the best opportunity to describe the ablation process. However, the limitations of these models in terms of the size of the system that can be modelled in a reasonable time, due to the computational power that is required, greatly reduce their applicability for the simulation of surface profiles.

The moderate pulse energy that is required to ensure processing within the optical ablation regime, see section 2.2, implies that most of the available energy of a modern laser source is not used for material removal. In order to fully exploit the available energy, parallel processing is recommended. This for example consists of dividing the beam into multiple beams, (e.g. by diffractive optical elements) for beam splitting and parallel processing, or by adjusting the beam intensity profile with a spatial light modulator. This will increase the throughput, which is currently one of major limitations towards industrial implementation of laser micromachining with picosecond laser pulses.

Further, the experimental analysis of the ablation process introduced in chapter 4, suggests that laser spots showing a uniform fluence distribution, just below the transition into the thermal regime, should be optimal for the material removal process. The pulse intensity profile can be adjusted to obtain such a distribution. As discussed above, employing arrays of laser spots, or the use of cylindrical lenses for focusing a beam into a line, instead of a circular spot, allows to keep the peak incident fluence within adequate values, while employing a higher percentage of the available energy per pulse.

The temporal separation between consecutive laser pulses has been shown to have a negligible effect on the generated microstructures, for the material/laser processing conditions studied in this work. As a consequence, the repetition rate of the laser source could be increased to increase the throughput. Laser sources with pulse duration in the picosecond or femtosecond regime, providing moderate to low energy per pulse and (therefore) high repetition rates, are recommended for high precision laser micromachining. However, modern laser sources provide repetition rates in the MHz regime, where the effect of heat accumulation on the ablated depth per pulse might not be negligible. The effect of heat accumulation requires additional study. Operating at higher repetition rates, may result in a significant contribution of inter-pulse effects, mainly due to heat accumulation, which are expected to contribute to the material removal process. This contribution cannot be accounted for with the calibration procedure described in this work. Therefore, an alternative method, that takes in consideration the time between laser pulses, would be required to correctly describe the ablated depth. This may consist of, for example, measuring the depth profile of laser tracks scanned at a certain pulse repetition rate and spatial pulse to pulse overlap.

The model developed in chapter 3 allows an accurate calculation of the surface profile for relatively shallow microstructures, up to a depth of about 30 μm. As a microstructure becomes deeper, the accuracy is lost due to several physical phenomena, which were introduced in section 3.6. Advantage could be taken from a model capable of calculating deeper structures, e.g., for hole drilling. To this end, further research into the effects of multiple reflections within a microstructure, or the absorption of laser energy by the ejected material, is required.

As shown in section 3.2.1, the one-dimensionality of the ablation process suits well for an extended analysis of the material removal process employing ray-tracing techniques, which can reveal areas exposed to multiple reflections. The calibration procedure described in section 4.4 should then be updated, to relate values of local absorbed fluence to the corresponding ablated depth. This correction is not taken into account with the present approach, and can be employed as an extension for the simulation of deeper microstructures.

Additional mechanisms for material removal, which are related to the formation of a plasma in deep holes, could be included for an improved description of the material removal process. The effects of particle shielding and plasma formation can also be reduced by employing appropriate shielding gases, or by the flow of a thin liquid film on the surface, which will enhance the dilution of the particle cloud in the interaction volume, and the chances of plasma ignition. Alternative machining strategies can also reduce the interaction of the laser pulse with a particle cloud, by simply redistributing the laser pulses across the area to be processed, ensuring that there is sufficient time between pulses arriving at a given location on the surface.

Part II. Laser-generated functional microstructures

From the point of view of microfluidics, an extended analysis of processing conditions can be performed to obtain substrates with novel functionalities. For example, processing superhydrophobic surfaces with smooth and rough peaks, see section 6.4, allows creating patterns with contrasting (super)hydrophobic/hydrophilic patterns. These patterns can be exploited for accurate positioning of small droplets of aqueous solutions, for e.g. self-assembling of macromolecules or immobilization of functional materials, or for controlling the liquid flow on a patterned substrate.

Further, advantage can be taken from the variety of materials that can be processed with short laser pulses. Virtually any material (ceramic, polymeric and metallic) can be processed by a proper selection of pulse characteristics [9]. The applicability of the model can be investigated and extended by analyzing the morphology of a ceramic or polymeric substrate exposed to an increased number of laser pulses. This would allow the prediction of suitable geometries for the creation of superhydrophobic surfaces directly on hydrophobic substrates, avoiding the use of top hydrophobic coatings.

The material removal process by short laser pulses employed in this work leads to up-concave surface profiles, due to the normal incidence of the laser beam with respect to the substrate. Advance beam guiding techniques could be developed for positioning the laser beam at an arbitrary angle of incidence, allowing material removal from the “sides” of a generated microstructure. This could be exploited for the creation of surface profiles showing re-entrant curvatures, which have been shown to provide oleophobic properties. An alternative method for the creation of re-entrant curvatures would be developing 3D micromachining processes. These could consist of, e.g., a local modification generated by focusing the laser beam into a small volume in a semi-transparent material. This modification can be subsequently selectively etched by a chemical reagent [124].

The study of the Leidenfrost point reduction can be extended by creating networks of cavities with varying interconnectivity. The creation of sparse cavities may lead to a destabilization of the vapour film, promoting a higher Leidenfrost point, while an increased interconnectivity of the surface features should have the opposite effect. Further investigation of the Leidenfrost point of microstructures with varying spacings would therefore give additional information on the role of the shape and interconnectivity of the cavities on the reported decrease of the Leidenfrost point.

Smaller focal spots can be employed to investigate the role of microcavities as heterogeneous nucleation sites, to determine whether the microcavities contribute to the stabilization of the film, by enhancing bubble merging or by actually acting as nucleation sites. Near-field laser nanomachining by means of microspheres can be exploited to create nucleation sites with submicrometer size [125].

Extended research on microstructured surfaces can also be of interest for enhancing recently proposed drag reduction mechanisms [126] by taking advantage of the Leidenfrost state found at lower temperatures.

The self-propelling properties of a liquid on a micratcheted substrate are of special interest in microfluidics. Micrometric sized droplets can be directed to desired locations in microfluidic devices. From this point of view, it would be interesting to investigate more complex ratcheted patterns, in which the direction of the accelerated droplets is given by the design of the microstructure. The combination of asymmetric (ratcheted) and symmetric (arrays of pillars and blind holes) microstructures may provide a promising solution for the transport and controlled evaporation of colloidal or polymer droplets, to create solid micro/nanoparticles or complex particles (capsules, janus..., etc.) on selected locations on a surface.

Bibliography

[1] W. Barthlott and C. Neinhuis. Purity of the sacred lotus, or escape from contamination in biological surfaces. *Planta*, 202(1):1–8, 1997.

[2] M.R. Cardoso, V. Tribuzi, D.T. Balogh, L. Misoguti, and C.R. Mendonça. Laser microstructuring for fabricating superhydrophobic polymeric surfaces. *Applied Surface Science*, 257(8):3281–3284, 2011.

[3] V. Zorba, E. Stratakis, M. Barberoglou, E. Spanakis, P. Tzanetakis, and C. Fotakis. Tailoring the wetting response of silicon surfaces via fs laser structuring. *Applied Physics A: Materials Science & Processing*, 93(4):819–825, 2008.

[4] A. Nakajima, K. Hashimoto, and T. Watanabe. Recent studies on super-hydrophobic films. *Monatshefte für Chemie / Chemical Monthly*, 132(1):31–41, 2001.

[5] C. Lee and C. Kim. Maximizing the giant liquid slip on superhydrophobic microstructures by nanostructuring their sidewalls. *Langmuir*, 25(21):12812–12818, 2009.

[6] D. Quéré. Non-sticking drops. *Reports on Progress in Physics*, 68(11):2495–2532, 2005.

[7] B. Bhushan. Biomimetics: Lessons from nature - an overview. *Philosophical Transactions of the Royal Society A: Mathematical, Physical and Engineering Sciences*, 367(1893):1445–1486, 2009.

[8] A. Tuteja, W. Choi, M. Ma, J.M. Mabry, S.A. Mazzella, G.C. Rutledge, G.H. McKinley, and R.E. Cohen. Designing superoleophobic surfaces. *Science*, 318(5856):1618–1622, 2007.

[9] J. Meijer, K. Du, A. Gillner, D. Hoffmann, V.S. Kovalenko, T. Masuzawa, A. Ostendorf, R. Poprawe, and W. Schulz. Laser machining

by short and ultrashort pulses, state of the art and new opportunities in the age of the photons. *CIRP Annals - Manufacturing Technology*, 51(2):531–550, 2002.

[10] F. Dausinger, H. Hugel, and V.I. Konov. Micromachining with ultrashort laser pulses: from basic understanding to technical applications. In *Proceedings of the SPIE, International Conference on Advanced Laser Technologies*, volume 5147, pages 106–115, 2003.

[11] K.S. Abedin and F. Kubota. *A 40 GHz Polarization Maintaining Picosecond Modelocked Fiber Laser Employing Photonic Crystal Fiber*, volume 164 of *IFIP International Federation for Information Processing*, chapter 51, pages 403–408. Springer US, 2005.

[12] S.I. Anisimov and B.S. Luk'yanchuk. Selected problems of laser ablation theory. *Physics-Uspekhi*, 45(3):293–324, 2002.

[13] B. Rethfeld, K. Sokolowski-Tinten, D. Von Der Linde, and S.I. Anisimov. Timescales in the response of materials to femtosecond laser excitation. *Applied Physics A: Materials Science and Processing*, 79(4-6):767–769, 2004.

[14] D. Bäuerle. *Laser Processing and Chemistry.* Springer-Verlag, Berlin, fourth edition, 2000.

[15] C. Momma, S. Nolte, B.N. Chichkov, F. v. Alvensleben, and A. Tünnermann. Precise laser ablation with ultrashort pulses. *Applied Surface Science*, 109–110(0):15–19, 1997.

[16] S.S. Wellershoff, J. Hohlfeld, J. Güdde, and E. Matthias. The role of electron-phonon coupling in femtosecond laser damage of metals. *Applied Physics A: Materials Science and Processing*, 69(7):S99–S107, 1999.

[17] E.G. Gamaly. The physics of ultra-short laser interaction with solids at non-relativistic intensities. *Physics Reports*, 508(4-5):91–243, 2011.

[18] P. Lorazo, L.J. Lewis, and M. Meunier. Thermodynamic pathways to melting, ablation, and solidification in absorbing solids under pulsed laser irradiation. *Physical Review B*, 73(13):134108, 2006.

[19] S. Nolte, C. Momma, H. Jacobs, A. Tünnermann, B.N. Chichkov, B. Wellegehausen, and H. Welling. Ablation of metals by ultrashort

laser pulses. *Journal of the Optical Society of America B: Optical Physics*, 14(10):2716–2722, 1997.

[20] B.N. Chichkov, C. Momma, S. Nolte, F. von Alvensleben, and A. Tünnermann. Femtosecond, picosecond and nanosecond laser ablation of solids. *Applied Physics A: Materials Science & Processing*, 63(2):109–115, 1996.

[21] N. Bityurin, B.S. Luk'yanchuk, M.H. Hong, and T.C. Chong. Models for laser ablation of polymers. *Chemical Reviews*, 103(2):519–552, 2003.

[22] J.E.A. Pedder and A.S. Holmes. A study of angular dependence in the ablation rate of polymers by nanosecond pulses. In *Proceedings of SPIE - The International Society for Optical Engineering*, volume 6106. SPIE, 2006.

[23] Y.V. Afanasiev, V.A. Isakov, I.N. Zavestovskaya, B.N. Chichkov, F. von Alvensleben, and H. Welling. Hydrodynamic regimes of uv laser ablation of polymers. *Applied Physics A*, 64(6):561–572, 1997.

[24] S. Küper, J. Brannon, and K. Brannon. Threshold behavior in polyimide photoablation: Single-shot rate measurements and surface-temperature modeling. *Applied Physics A: Materials Science & Processing*, 56(1):43–50, 1993.

[25] B. Sinkovics, P. Gordon, and G. Harsányi. Computer modelling of the laser ablation of polymers. *Applied Thermal Engineering*, 30(16):2492–2498, 2010.

[26] S. R. Vatsya, E. V. Bordatchev, and S. K. Nikumb. Geometrical modeling of surface profile formation during laser ablation of materials. *Journal of Applied Physics*, 93(12):9753–9759, 2003.

[27] T. Schwarz-Selinger, D.G. Cahill, S.C. Chen, S.J. Moon, and C.P. Grigoropoulos. Micron-scale modifications of si surface morphology by pulsed-laser texturing. *Physical Review B - Condensed Matter and Materials Physics*, 64(15):1553231–1553237, 2001.

[28] J.E.A. Pedder, A.S. Holmes, and P.E. Dyer. Improved model for the angular dependence of excimer laser ablation rates in polymer materials. *Applied Physics Letters*, 95(17), 2009.

[29] M.C. Gower, E. Davies, and A.S. Holmes. Optical modeling of laser ablated microstructures. *Journal of Applied Physics*, 112(9):093112–9, 2012.

[30] M.I. Kaganov, I.M. Lifshitz, and L.V. Tanatarov. Relaxation between electrons and crystalline lattices. *Journal of Experimental and Theoretical Physics*, 4(2):173–178, 1957.

[31] S.I. Anisimov, Y.A. Imas, G.S. Romanov, and Y.V. Khodyko. *Effect of High-Power Radiation on Metals*. National Technical Information Service, Springfield, V.A., 1971.

[32] S.I. Anisimov, A.M. Bonch-Bruevich, and M.A. El'yashevich. Effect of powerful light fluxes on metals. *Soviet Physics - Technical Physics*, 11:945, 1967.

[33] S.I. Anisimov, B.L. Kapeliovich, and T.L. Perel'man. Electron emission from metal surfaces exposed to ultrashort laser pulses. *Journal of Experimental and Theoretical Physics Letters*, 66(2):776–781, 1974.

[34] S.I. Anisimov, V.V. Zhakhovski, N.A. Inogamov, K. Nishihara, Yu V. Petrov, and V.A. Khokhlov. Ablated matter expansion and crater formation under the action of ultrashort laser pulse. *Journal of Experimental and Theoretical Physics*, 103(2):183–197, 2006.

[35] R. Le Harzic, N. Huot, E. Audouard, C. Jonin, P. Laporte, S. Valette, A. Fraczkiewicz, and R. Fortunier. Comparison of heat-affected zones due to nanosecond and femtosecond laser pulses using transmission electronic microscopy. *Applied Physics Letters*, 80(21):3886–3888, 2002.

[36] L.V. Zhigilei, Z. Lin, and D.S. Ivanov. Atomistic modeling of short pulse laser ablation of metals: Connections between melting, spallation, and phase explosion. *The Journal of Physical Chemistry C*, 113(27):11892–11906, 2009.

[37] E. Leveugle, D.S. Ivanov, and L.V. Zhigilei. Photomechanical spallation of molecular and metal targets: Molecular dynamics study. *Applied Physics A: Materials Science and Processing*, 79(7):1643–1655, 2004.

[38] S.I. Anisimov, N.A. Inogamov, Y.V. Petrov, V.A. Khokhlov, V.V. Zhakhovskii, K. Nishihara, M.B. Agranat, S.I. Ashitkov, and P.S.

Komarov. Interaction of short laser pulses with metals at moderate intensities. *Applied Physics A: Materials Science and Processing*, 92(4):939–943, 2008.

[39] D. Perez and L.J. Lewis. Molecular-dynamics study of ablation of solids under femtosecond laser pulses. *Physical Review B*, 67(18):184102, 2003.

[40] B.S. Luk'yanchuk, S.I. Anisimov, and Y.F. Lu. Dynamics of subpicosecond laser ablation, examined by moments technique. In *Proceedings of the SPIE, International Conference on Advanced Laser Technologies*, volume 4423, pages 141–152, 2000.

[41] D.S. Ivanov and L.V. Zhigilei. Combined atomistic-continuum modeling of short-pulse laser melting and disintegration of metal films. *Physical Review B - Condensed Matter and Materials Physics*, 68(6):641141–6411422, 2003.

[42] J. Jandeleit, G. Urbasch, H.D. Hoffmann, H.G. Treusch, and E.W. Kreutz. Picosecond laser ablation of thin copper films. *Applied Physics A: Materials Science & Processing*, 63(2):117–121, 1996.

[43] S. Laville, F. Vidal, T. W. Johnston, O. Barthélemy, M. Chaker, B. Le Drogoff, J. Margot, and M. Sabsabi. Fluid modeling of the laser ablation depth as a function of the pulse duration for conductors. *Physical Review E - Statistical, Nonlinear, and Soft Matter Physics*, 66(6), 2002.

[44] W. Hu, Y. Shin, and G. King. Modeling of multi-burst mode picosecond laser ablation for improved material removal rate. *Applied Physics A: Materials Science & Processing*, 98(2):407–415, 2010.

[45] L. J. Lewis and D. Perez. Laser ablation with short and ultrashort laser pulses: Basic mechanisms from molecular-dynamics simulations. *Applied Surface Science*, 255(10):5101–5106, 2009.

[46] A. Spiro, M. Lowe, and G. Pasmanik. Drilling rate of five metals with picosecond laser pulses at 355, 532, and 1064 nm. *Applied Physics A: Materials Science & Processing*, 107(4):801–808, 2012.

[47] C.J. Hayden. A simple three-dimensional computer simulation tool for predicting femtosecond laser micromachined structures. *Journal of Micromechanics and Microengineering*, 20(2):025010, 2010.

[48] Y. Yashkir and Q. Liu. Experimental and theoretical study of the laser micro-machining of glass using a high-repetition-rate ultrafast laser. In *Proceedings of SPIE - Solid State Lasers and Amplifiers II; Strasbourg; France*, volume 6190, page 61900V, 2006.

[49] T. Baldacchini, J.E. Carey, M. Zhou, and E. Mazur. Superhydrophobic surfaces prepared by microstructuring of silicon using a femtosecond laser. *Langmuir*, 22(11):4917–4919, 2006.

[50] T.O. Yoon, H.J. Shin, S. C. Jeoung, and Y.I.I. Park. Formation of superhydrophobic poly(dimethysiloxane) by ultrafast laser-induced surface modification. *Optics Express*, 16(17):12715–12725, 2008.

[51] A.M. Kietzig, S.G. Hatzikiriakos, and P. Englezos. Patterned superhydrophobic metallic surfaces. *Langmuir*, 25(8):4821–4827, 2009.

[52] P. Bizi-Bandoki, S. Benayoun, S. Valette, B. Beaugiraud, and E. Audouard. Modifications of roughness and wettability properties of metals induced by femtosecond laser treatment. *Applied Surface Science*, 257(12):5213–5218, 2011.

[53] B. Wu, M. Zhou, J. Li, X. Ye, G. Li, and L. Cai. Superhydrophobic surfaces fabricated by microstructuring of stainless steel using a femtosecond laser. *Applied Surface Science*, 256(1):61–66, 2009.

[54] T. Jiang, J. Koch, C. Unger, E. Fadeeva, A. Koroleva, Q. Zhao, and B.N. Chichkov. Ultrashort picosecond laser processing of micromolds for fabricating plastic parts with superhydrophobic surfaces. *Applied Physics A: Materials Science and Processing*, 108(4):863–869, 2012.

[55] M. Groenendijk. Fabrication of super hydrophobic surfaces by fs laser pulses. *Laser Technik Journal*, 5(3):44–47, 2008.

[56] S. M. Eaton, C. De Marco, R. Martinez-Vazquez, R. Ramponi, S. Turri, G. Cerullo, and R. Osellame. Femtosecond laser microstructuring for polymeric lab-on-chips. *Journal of Biophotonics*, 5(8-9):687–702, 2012.

[57] D. L. N. Kallepalli, N. R. Desai, and V. R. Soma. Fabrication and optical characterization of microstructures in poly(methylmethacrylate) and poly(dimethylsiloxane) using femtosecond pulses for photonic and microfluidic applications. *Applied Optics*, 49(13):2475–2489, 2010.

[58] R. Osellame, H. J. W. M. Hoekstra, G. Cerullo, and M. Pollnau. Femtosecond laser microstructuring: An enabling tool for optofluidic lab-on-chips. *Laser and Photonics Reviews*, 5(3):442–463, 2011.

[59] R. Suriano, A. Kuznetsov, S. M. Eaton, R. Kiyan, G. Cerullo, R. Osellame, B. N. Chichkov, M. Levi, and S. Turri. Femtosecond laser ablation of polymeric substrates for the fabrication of microfluidic channels. *Applied Surface Science*, 257(14):6243–6250, 2011.

[60] R. Osellame, V. Maselli, R.M. Vazquez, R. Ramponi, and G. Cerullo. Integration of optical waveguides and microfluidic channels both fabricated by femtosecond laser irradiation. *Applied Physics Letters*, 90(23), 2007.

[61] F. Siegel, U. Klug, and R. Kling. Extensive micro-structuring of metals using picosecond pulses – ablation behavior and industrial relevance. *Journal of Laser Micro Nanoengineering*, 4:104–110, 2009.

[62] P.B. Corkum, F. Brunel, N.K. Sherman, and T. Srinivasan-Rao. Thermal response of metals to ultrashort-pulse laser excitation. *Physical Review Letters*, 61(25):2886–2889, 1988.

[63] J. Bonse, J.M. Wrobel, J. Krüger, and W. Kautek. Ultrashort-pulse laser ablation of indium phosphide in air. *Applied Physics A: Materials Science & Processing*, 72(1):89–94, 2001.

[64] B. Luther-Davies, A. V. Rode, N. R. Madsen, and E. G. Gamaly. Picosecond high-repetition-rate pulsed laser ablation of dielectrics: The effect of energy accumulation between pulses. *Optical Engineering*, 44(5):1–8, 2005.

[65] C.S. Nielsen and P. Balling. Deep drilling of metals with ultrashort laser pulses: A two-stage process. *Journal of Applied Physics*, 99(9), 2006.

[66] J. Byskov-Nielsen, J. Savolainen, M. Christensen, and P. Balling. Ultra-short pulse laser ablation of metals: threshold fluence, incubation coefficient and ablation rates. *Applied Physics A: Materials Science & Processing*, 101(1):97–101, 2010.

[67] Y. Yang, J. Yang, C. Liang, and H. Wang. Ultra-broadband enhanced absorption of metal surfaces structured by femtosecond laser pulses. *Optics Express*, 16(15):11259–11265, 2008.

[68] A.Y. Vorobyev and C. Guo. Enhanced absorptance of gold following multipulse femtosecond laser ablation. *Physical Review B - Condensed Matter and Materials Physics*, 72(19), 2005.

[69] J.M. Liu. Simple technique for measurements of pulsed gaussian-beam spot sizes. *Optics Letters*, 7(5):196–198, 1982.

[70] E. Carpene, E. Mancini, C. Dallera, M. Brenna, E. Puppin, and S. De Silvestri. Dynamics of electron-magnon interaction and ultrafast demagnetization in thin iron films. *Physical Review B - Condensed Matter and Materials Physics*, 78(17), 2008.

[71] J.E. Sipe, J.F. Young, J.S. Preston, and H.M. Van Driel. Laser-induced periodic surface structure. I. Theory. *Physical Review B*, 27(2):1141–1154, 1983.

[72] J.F. Young, J.S. Preston, H.M. Van Driel, and J.E. Sipe. Laser-induced periodic surface structure. II. Experiments on Ge, Si, Al, and brass. *Physical Review B*, 27(2):1155–1172, 1983.

[73] A. Ancona, S. Döring, C. Jauregui, F. Röser, J. Limpert, S. Noite, and A. Tünnermann. Femtosecond and picosecond laser drilling of metals at high repetition rates and average powers. *Optics Letters*, 34(21):3304–3306, 2009.

[74] D. Breitling, A. Ruf, and F. Dausinger. Fundamental aspects in machining of metals with short and ultrashort laser pulses. In *Proceedings of SPIE - The International Society for Optical Engineering*, volume 5339, pages 49–63, 2004.

[75] M.K. Dawood, H. Zheng, T.H. Liew, K.C. Leong, Y.L. Foo, R. Rajagopalan, S.A. Khan, and W.K. Choi. Mimicking both petal and lotus effects on a single silicon substrate by tuning the wettability of nanostructured surfaces. *Langmuir*, 27(7):4126–4133, 2011.

[76] Y.Y. Yan, N. Gao, and W. Barthlott. Mimicking natural superhydrophobic surfaces and grasping the wetting process: A review on recent progress in preparing superhydrophobic surfaces. *Advances in Colloid and Interface Science*, 169(2):80–105, 2011.

[77] N.A. Patankar. Mimicking the lotus effect: Influence of double roughness structures and slender pillars. *Langmuir*, 20(19):8209–8213, 2004.

[78] D. Quéré. Wetting and roughness. *Annual Review of Materials Research*, 38:71–99, 2008.

[79] J.G. Leidenfrost. On the fixation of water in diverse fire (Duisburg, 1756). *International Journal of Heat and Mass Transfer*, 9(11):1153 – 1166, 1966. Reprint.

[80] J.D. Bernardin and I. Mudawar. The Leidenfrost point: experimental study and assessment of existing models. *Transactions-American Society Of Mechanical Engineers Journal Of Heat Transfer*, 121:894–903, 1999.

[81] W.S. Bradfield. Liquid-solid contact in stable film boiling. *Industrial and Engineering Chemistry Fundamentals*, 5(2):200–204, 1966.

[82] C.T. Avedisian and J. Koplik. Leidenfrost boiling of methanol droplets on hot porous/ceramic surfaces. *International Journal of Heat and Mass Transfer*, 30(2):379–393, 1987.

[83] H. Kim, B. Truong, J. Buongiorno, and L.W. Hu. On the effect of surface roughness height, wettability, and nanoporosity on leidenfrost phenomena. *Applied Physics Letters*, 98:083121, 2011.

[84] S. Adera, R. Raj, R. Enright, and E.N. Wang. Non-wetting droplets on hot superhydrophilic surfaces. *Nature Communications*, 4(2518), 2013.

[85] H. Linke, B. Alemán, L. Melling, M. Taormina, M. Francis, C. Dow-Hygelund, V. Narayanan, R. Taylor, and A. Stout. Self-Propelled Leidenfrost Droplets. *Physical Review Letters*, 96(15), April 2006.

[86] G. Dupeux, M. Le Merrer, C. Clanet, and D. Quéré. Trapping Leidenfrost drops with crenelations. *Physical Review Letters*, 107(11):114503, 2011.

[87] G. Lagubeau, M. Le Merrer, C. Clanet, and D. Quéré. Leidenfrost on a ratchet. *Nature Physics*, 7(5):395–398, 2011.

[88] G. Dupeux, M. Le Merrer, G. Lagubeau, C. Clanet, S. Hardt, and D. Quéré. Viscous mechanism for Leidenfrost propulsion on a ratchet. *Europhysics Letters*, 96:1–7, 2011.

[89] P.G. de Gennes, F. Brochard-Wyart, and D. Quéré. *Capillarity and Wetting Phenomena: Drops, Bubbles, Pearls, Waves*. Springer, 2004.

[90] T. Young. An essay on the cohesion of fluids. *Philosophical Transactions of the Royal Society of London*, 95:65–87, 1805.

[91] A. Lafuma and D. Quéré. Superhydrophobic states. *Nature Materials*, 2(7):457–460, 2003.

[92] R.N. Wenzel. Resistance of solid surfaces to wetting by water. *Industrial and Engineering Chemistry*, 28(8):988–994, 1936.

[93] A.B.D. Cassie and S. Baxter. Wettability of porous surfaces. *Transactions of the Faraday Society*, 40:546–551, 1944.

[94] B. Bhushan and Y.C. Jung. Natural and biomimetic artificial surfaces for superhydrophobicity, self-cleaning, low adhesion, and drag reduction. *Progress in Materials Science*, 56(1):1–108, 2010.

[95] A. Marmur. From hygrophilic to superhygrophobic: Theoretical conditions for making high-contact-angle surfaces from low-contact-angle materials. *Langmuir*, 24(14):7573–7579, 2008.

[96] N.A. Patankar. On the modeling of hydrophobic contact angles on rough surfaces. *Langmuir*, 19(4):1249–1253, 2003.

[97] E. Bittoun and A. Marmur. Optimizing super-hydrophobic surfaces: Criteria for comparison of surface topographies. *Journal of Adhesion Science and Technology*, 23(3):401–411, 2009.

[98] A. Marmur. The lotus effect: Superhydrophobicity and metastability. *Langmuir*, 20(9):3517–3519, 2004.

[99] M. Nosonovsky and B. Bhushan. Roughness-induced superhydrophobicity: a way to design non-adhesive surfaces. *Journal of Physics: Condensed Matter*, 20(22):225009, 2008.

[100] D. Quéré, A. Lafuma, and J. Bico. Slippy and sticky microtextured solids. *Nanotechnology*, 14(10):1109–1112, 2003.

[101] P. Kim, T.S. Wong, J. Alvarenga, M.J. Kreder, W.E. Adorno-Martinez, and J. Aizenberg. Liquid-infused nanostructured surfaces with extreme anti-ice and anti-frost performance. *ACS Nano*, 6(8):6569–6577, 2012.

[102] J. Bico, C. Tordeux, and D. Quéré. Rough wetting. *Europhysics Letters*, 55(2):214–220, 2001.

[103] K. Koch, H.F. Bohn, and W. Barthlott. Hierarchically sculptured plant surfaces and superhydrophobicity. *Langmuir*, 25(24):14116–14120, 2009.

[104] B. Bhushan and Y.C. Jung. Natural and biomimetic artificial surfaces for superhydrophobicity, self-cleaning, low adhesion, and drag reduction. *Progress in Materials Science*, 56(1):1–108, 2011.

[105] C. Lee and C.J. Kim. Influence of surface hierarchy of superhydrophobic surfaces on liquid slip. *Langmuir*, 27(7):4243–4248, 2011.

[106] Y. Kwon, N. Patankar, J. Choi, and J. Lee. Design of surface hierarchy for extreme hydrophobicity. *Langmuir*, 25(11):6129–6136, 2009.

[107] J.F. Joanny and P.G. De Gennes. A model for contact angle hysteresis. *The Journal of Chemical Physics*, 81(1):552–562, 1984.

[108] H. Kusumaatmaja and J.M. Yeomans. Modeling contact angle hysteresis on chemically patterned and superhydrophobic surfaces. *Langmuir*, 23(11):6019–6032, 2007.

[109] Johnson R.E. and Dettre R.H. *Contact Angle Hysteresis*, volume 43 of *Advances in Chemistry*, chapter 7, pages 112–135. American Chemical Society, 1964.

[110] B.S. Gottfried and K.J. Bell. Film boiling of spheroidal droplets. Leidenfrost phenomenon. *Industrial & Engineering Chemistry Fundamentals*, 5(4):561–568, 1966.

[111] H. Linke, B.J. Alemán, L.D. Melling, M.J. Taormina, M.J. Francis, C.C. Dow-Hygelund, V. Narayanan, R.P. Taylor, and A. Stout. Self-propelled Leidenfrost droplets. *Physical Review Letters*, 96(15):154502, 2006.

[112] G. Dupeux, C. Clanet, S. Hardt, and D. Quéré. Viscous mechanism for leidenfrost propulsion on a ratchet. *Bulletin of the American Physical Society*, 56, 2011.

[113] G. Liu, L. Fu, A.V. Rode, and V.S.J. Craig. Water droplet motion control on superhydrophobic surfaces: Exploiting the Wenzel-to-Cassie transition. *Langmuir*, 27(6):2595–2600, 2011.

[114] I.U. Vakarelski, J.O. Marston, D.Y.C. Chan, and S.T. Thoroddsen. Drag reduction by leidenfrost vapor layers. *Physical Review Letters*, 106(21):214501, 2011.

[115] Y. Sugiyama, R.J. Larsen, J.W. Kim, and D.A. Weitz. Buckling and crumpling of drying droplets of colloid-polymer suspensions. *Langmuir*, 22(14):6024–6030, 2006.

[116] I.U. Vakarelski, N.A. Patankar, J.O. Marston, D.Y.C. Chan, and S.T. Thoroddsen. Stabilization of leidenfrost vapour layer by textured superhydrophobic surfaces. *Nature*, 489(7415):274–277, 2012.

[117] C. Kruse, T. Anderson, C. Wilson, C. Zuhlke, D. Alexander, G. Gogos, and S. Ndao. Extraordinary shifts of the leidenfrost temperature from multiscale micro/nanostructured surfaces. *Langmuir*, 29(31):9798–9806, 2013.

[118] J. D. Bernardin and I. Mudawar. A Cavity Activation and Bubble Growth Model of the Leidenfrost Point. *Journal of Heat Transfer*, 124(5):864–874, 2002.

[119] I.N. Levine. *Physical chemistry*. McGraw-Hill, 2002.

[120] E.R.G. Eckert and R.M. Jr. Drake. *Analysis of heat and mass transfer*. McGraw-Hill, New York, 1987.

[121] A. Würger. Leidenfrost gas ratchets driven by thermal creep. *Physical Review Letters*, 107(16):164502, 2011.

[122] J.C. Maxwell. On stresses in rarified gases arising from inequalities of temperature. *Philosophical Transactions of the Royal Society of London*, 170:231–256, 1879.

[123] Á. Gómez Marín, D. Arnaldo del Cerro, G.R.B.E. Römer, B. Pathiraj, A.J. Huis in 't Veld, and D. Lohse. Capillary droplets on leidenfrost micro-ratchets. *Physics of Fluids*, 24(12):122001–10, 2012.

[124] S. Kiyama, S. Matsuo, S. Hashimoto, and Y. Morihira. Examination of etching agent and etching mechanism on femotosecond laser microfabrication of channels inside vitreous silica substrates. *Journal of Physical Chemistry C*, 113(27):11560–11566, 2009.

[125] X. Sedao, T.J.-Y. Derrien, G.R.B.E. Römer, B. Pathiraj, and A.J. Huis in 't Veld. Large area laser surface micro/nanopatterning by contact microsphere lens arrays. *Applied Physics A: Materials Science and Processing*, 111(3):701–709, 2013.

[126] P. Tsai, A. M. Peters, C. Pirat, M. Wessling, R. G. H. Lammertink, and D. Lohse. Quantifying effective slip length over micropatterned hydrophobic surfaces. *Physics of Fluids*, 21(11):1–8, 2009.

[127] R. Le Harzic, D. Breitling, M. Weikert, S. Sommer, C. Föhl, S. Valette, C. Donnet, E. Audouard, and F. Dausinger. Pulse width and energy influence on laser micromachining of metals in a range of 100 fs to 5 ps. *Applied Surface Science*, 249(1-4):322–331, 2005.

Appendices

Appendix I

Mean ablated profile calculation

Experimental data on ablated profiles as presented in section 4.3 were acquired by means of CLSM. In order to reduce the measurement noise of the data, several ablated profiles, machined under identical conditions, were averaged. Each raw data set consisted of a matrix of 550 by 550 pixels, containing height information at each location h(x,y). The first moment of each image $(\bar{x}, \bar{y})$ was calculated and employed for centering the surface profiles, according to

$$\bar{x} = \frac{\int\int x\, h(x,y)\, \mathrm{d}x\mathrm{d}y}{\int\int h(x,y)\, \mathrm{d}x\mathrm{d}y} \qquad \bar{y} = \frac{\int\int y\, h(x,y)\, \mathrm{d}x\mathrm{d}y}{\int\int h(x,y)\, \mathrm{d}x\mathrm{d}y}. \tag{1}$$

An average surface profile was obtained by averaging the height of a given number of surface profiles, centered at $(x - \bar{x}, y - \bar{y})$. A minimum of 5 independent measurements were employed for each experimental set of laser processing conditions.

Surface profile smoothening by weighted robust local linear regression

In order to follow the evolution of an ablated profile, as the number of applied pulses increases, a smooth curve was fitted to the experimental data, see for example figure 4.3 on page 46. The data sets of ablated profiles were processed in a way that each experimental point was replaced by a calculated smooth value. The calculated smooth value was obtained by performing a weighted linear surface regression, using neighbour data points falling within a selected span. The weights w_i for each data point were calculated as

$$w_i = \left(1 - \left|\frac{x - x_i}{d(x)}\right|^3\right), \tag{2}$$

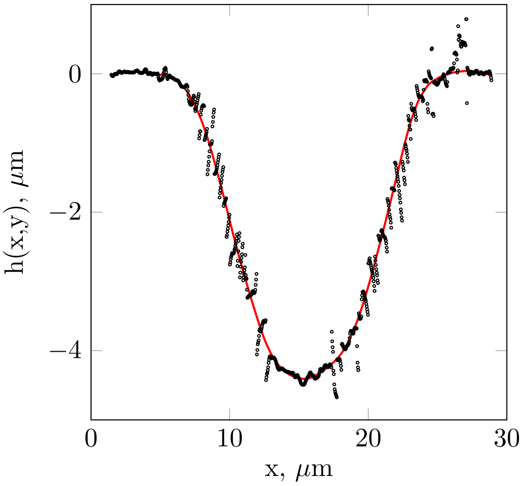

Figure 1.: Cross section of a calculated smooth profile (solid red line), compared to the raw (not averaged) data (circles), of a laser generated ablated profile. Processing conditions: 200 laser pulses at peak fluence of 0.52 J/cm^2, 515 nm and pulse duration < 10 ps.

where x is the value to be smoothed, x_i are the collection of points falling within the span, and $d(x)$ is the distance from x to the most distant data point within the interval determined by the span. In this way, data points that are close to the point to be smoothened have weights close to one, while distant points have less influence in the weighting.

Next, a weighted linear least-squares regression was performed, using a second degree polynomial. The smoothed values are obtained by evaluation of the weighted local regression at each location. By properly selecting the span, which was set to 10% of the total number of data points, the resulting fitting curve becomes smoother without deviating from the data point set. A cross section of the calculated smooth profile, compared to the raw (not averaged) data, is shown in figure 1.

Appendix II

Physical properties of selected materials

Table 1.: Thermal and physical properties of selected materials: ρ mass density; c_p specific heat; κ thermal conductivity; D thermal diffusivity; T_m melting temperature. Data obtained from [14].

Material	ρ, (kg/m^3)	c_p, (J/kg K)	κ, (W/m K)	$D \cdot 10^{-4}$, (m^2/s)	T_m, (K)
Al	2700	900	237	1.03	933
Ni	8900	440	89	0.24	1727
Mo	10200	260	137	0.52	2887
SS302	8030	500	15	0.04	1712

Table 2.: Electronic properties of selected materials: g electron phonon coupling strength; A_e electron specific heat constant; κ_{e0} electron heat conductivity; c_l lattice volumetric heat capacity. Data for Mo and Ni obtained from [16]. Data for Al obtained from [127].

Material	g, (W/m^3 K)	A_e, (J/m^3 K^2)	κ_{e0}, (W/m K)	$c_l \cdot 10^6$, (J/m^3 K)
Al	56.9	135	238	2.43
Ni	36	1065	91	4.1
Mo	13	350	135	2.8

Appendix III

Numerical calculation of surface areas

In order to obtain the parameters r, r_f and f in equations (6.2) and (6.3), see page 71, the surface area of a micro-structure has to be determined numerically. The method employed in this work to calculate this area is based on triangulation, which suits for smooth surfaces with uniformly spaced points (x, y, z). This is a fast and simple method that suits for the calculation of areas of multiple micro-structures, whose shape cannot be analytically described. The surface is divided into quadrilaterals, which are defined by 4 equally spaced consecutive points in the (x, y) plane, and then divided into 2 triangles. The area of each triangle is calculated from its defining vectors $\vec{u}$ and $\vec{w}$, see figure 2, and subsequently summed up. Calculating the surface area above a certain height level, consists of adding the areas of the quadrilaterals whose average height falls above the solid–liquid–vapour contact line (see section 6.5).

The area A of each triangle is given by half the magnitude of the cross

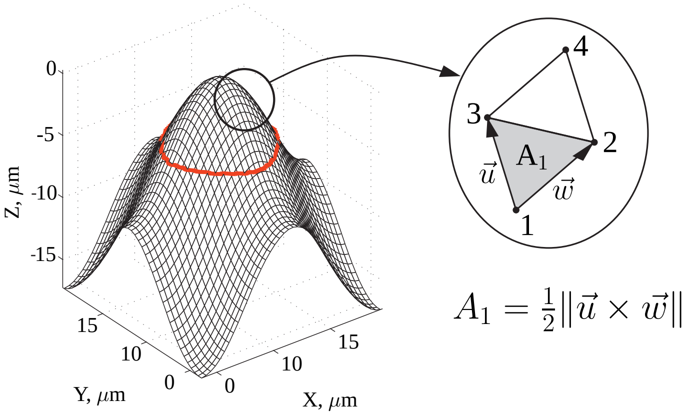

Figure 2.: Numerical calculation of surface areas.

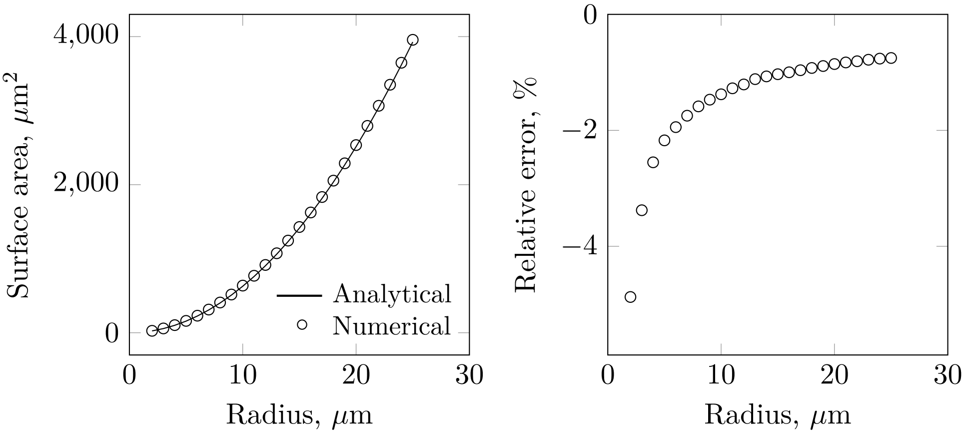

Figure 3.: Numerical and analytical calculation of surface areas. Left: analytical (solid line) and calculated (circles) surface areas of hemispheres with radii ranging from 2 to 25 μm. Right: relative error between analytical and numerical calculations.

product of its defining vectors, that is $A = \frac{1}{2}\|\vec{u} \times \vec{w}\|$. The (x, y, z) coordinates of each vertex of the triangle are known, so the total area of a quadrilateral, A_T, is simply given by $A_T = A_1 + A_2$, where A_1 and A_2 are calculated according to

$$A_1 = \frac{1}{2}\sqrt{(dxdy)^2 + (dx(z_3 - z_1))^2 + (dy(z_2 - z_1))^2} \tag{3}$$

$$A_2 = \frac{1}{2}\sqrt{(dxdy)^2 + (dx(z_4 - z_3))^2 + (dy(z_2 - z_4))^2}, \tag{4}$$

where dx and dy are the separation between equally spaced points in the (x, y) plane, and z_{1-4} are the z coordinates of each of the points defining a quadrangle.

The accuracy of the numerical calculation was evaluated by performing a direct comparison of numerically and analytically calculated surface areas of a perfect shape. Hemispheres of increasing radii, in the same range of sizes of the simulated peaks, were employed. The range of radii was selected from 2 to 25 μm, for a unit cell with a number of pixels (size) of 60×60, which corresponds to the narrowest simulated track separation (12μm), in section 6.5. Hence, the comparison was made for the unit cell for which the model was employed at its lower resolution.

Figure 3 shows the results of the comparison. As can be observed, the absolute values of numerical and analytical surface areas take similar values for the selected range of radii, figure 3(left), while the relative error remains below 5% for that range, figure 3(right).

An accurate estimate for the surface area can also be computed by fitting the surface to a cubic spline interpolant. The surface area of the interpolant can be evaluated with high accuracy employing numerical integration. The area A of the interpolant is calculated as

$$A = \int\int_W \sqrt{1 + \left(\frac{\partial H(x,y)}{\partial x}\right)^2 + \left(\frac{\partial H(x,y)}{\partial y}\right)^2}\, dxdy, \tag{5}$$

where $H(x, y)$ is the calculated surface profile, and W is the wet area, given by the location of the solid-liquid-vapour interface. The difference between the calculated wet areas, when employing the fast triangulation and the spline curve, is less than 1% (230 μm^2 for the triangulation vs. 232 μm^2 for the spline, when a surface area above a projected square of 75 by 75 pixels in the xy plane is measured). Therefore, the numerical approach, based on the fast triangulation algorithm, is considered to provide sufficient accuracy for the employed modelling conditions.

Acknowledgments

The process of becoming a doctor is unlikely to reach a good ending as a solitaire endeavor. Regardless personal efforts, it is only thanks to the support of many that one reaches his promotion date. I would like to express my gratitude to all the people that helped me during the years, and made this thesis possible.

First, I am indebted to my promoter Bert Huis in ‘t Veld, who gave the opportunity to become his first PhD student, and start this adventure of becoming a doctor. Also, I would not have reached this point without the continuous support of my daily supervisors Matthijn de Rooij and Gert-Willem Römer. Matthijn, thanks for the support and all the feedback. Gert-Willem, your advice, help and patience made this thesis possible. Thanks for keeping challenging me and making my work progress further. I am grateful and lucky to have an advisor who took care of me far beyond his responsibilities.

I would also like to thank the members of my graduation committee, Remko Akkerman, Stephan Barcikowski, Jaap den Toonder, Rob Lammertink and Detlef Lohse for taking the time for the critical review of this thesis.

Further, I would like to thank all the members of the Mechanical Automation group. Martina, I had a good feeling with you since the first emails we exchange prior my arrival to Enschede. You were always there to help, and your moral support was exactly what I needed so many times. Niya and Ralph, many thanks for your friendship and patient support. We had a lot of fun together. Pathiraj, many thanks for all the support and the common sense that you applied to my worries. Johan, Justus, Paul, Josef, Ali and Davide, thanks for all the discussions that made my work more complete and coherent. Bert, Ger, Gerald, Leo, Dannis, Johannes, Ronald, Jaap, Frank, Volkert, Steven and Wilco usually off-topic, but probably just as important as the strictly work related discussions, thank you. It has been a pleasure working with you all. Jonathan, many thanks for the last push and recommendations. Jitendra, Neelam and Bhairavi, many thanks for your friendship, help and accompany, particularly during the period after my injury.

During these years, I had the chance to collaborate with a number of fellow PhD candidates, whose shared experience and expertise saved me from many worries. Çan, many thanks for the advice and all the applied coatings. Burak, many thanks for sharing your expertise and original ideas. Alvaro, it has been a pleasure having the chance to work with you. Laura many thanks for your friendship and the help with the so much needed microscopy.

Michelle, Rene and Hans many thanks for your friendship and all the hours at the billiards. Also for taking care that I would not expend the whole of my time worrying about results. I am also thankful to all the people at Arriba, who showed me that playing basketball is only a little part of being a member of the club.

Finally, I would like to dedicate a few words to my family, whose unconditional support and understanding over the years allowed me to endure and enjoy one of the most challenging experiences of my life. Many thanks for everything!

Daniel Arnaldo del Cerro

Enschede, September 2014

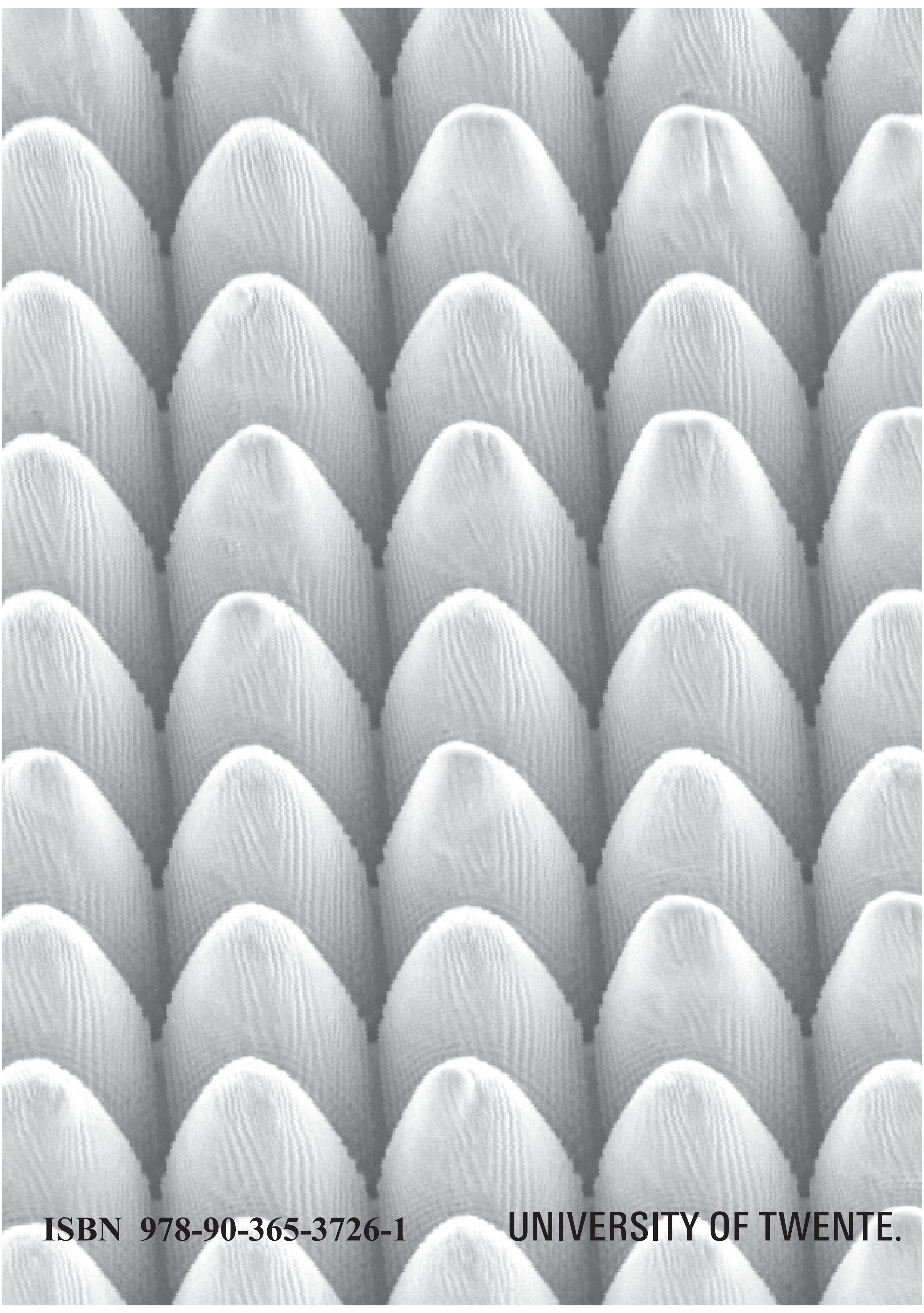

ISBN 978-90-365-3726-1

UNIVERSITY OF TWENTE.